Light-Matter Interactions in Optical Nanostructures Based on Organic Semiconductors

A DISSERTATION
SUBMITTED TO THE FACULTY OF THE GRADUATE SCHOOL
OF THE UNIVERSITY OF MINNESOTA
BY

Grant H. Lodden

IN PARTIAL FULFILLMENT OF THE REQUIREMENTS
FOR THE DEGREE OF
DOCTOR OF PHILOSOPHY

Russell J. Holmes, Advisor

December 2012

Acknowledgements

I would like to acknowledge some special people who have meant a lot to me through this process. First and foremost, I would like to thank my advisor Russell Holmes. His guidance and natural ability to educate has helped me broaden my knowledge and expertise, and assisted in making me the person and researcher that I am today. He has offered exceptional input throughout this process and motivated me to push myself allowing me to reach places I never thought were possible.

Secondly, I would like to thank all of the members of the Holmes and Frisbie groups that I have had the opportunity to collaborate with over my time at the University of Minnesota. Specifically, Wade, Kai, Nick, Richa, Matt, Yunlong, Bryan Boudouris, Derek Stevens and Dave Ellison. You all have made my time spent during this process enjoyable. I would also like to thank the administrative staff of Amundson Hall. Particularly, Julie Prince, Teresa Bredahl, Mary Nissen and Mary Haverkost for they have made the required departmental tasks seamless and were always willing to help if a problem arose. A tremendous amount of gratitude goes out to my two physics professors at Coe College, Dr. Steve Feller and Dr. Mario Affitigato. They are both outstanding professors and men. I am blessed to have experienced their exceptional teaching and the golden opportunities they provided for me.

Lastly, I would like to thank all of the people in my family. I would like to thank my parents, Ted and Judi, for serving as models for the importance of higher education. Their support and love has been a true catalyst for my work. They provided financial support in all of my endeavors and have encouraged me mentally and emotionally. I

would also like to thank my younger brother, Nolan, for having fun with me when I had time and for putting up with me when I did not. He gave me a reason to work hard to be someone he could be proud of and model after. I would like to thank the Gardiners as they have provided support and most importantly taken me into their wonderful family. Lastly, I would like to thank my wife, Allie, whose support and encouragement has kept me afloat throughout this entire process. Allie you have been nothing short of amazing in taking care of tasks when I did not have time to deal with them and being my foundation when I needed it most.

Dedication

This dissertation is dedicated to my wife Allie, my brother Nolan, and my parents Ted and Judi.

Abstract

The confinement of a semiconductor material to an optical microcavity leads to an inherent coupling between light and matter. Depending on the lifetime of the excited state of the semiconductor (the exciton) and the cavity photon, two distinct regimes of interaction are possible. The system is said to be weakly coupled if either the exciton or the cavity photon decay before the two species interact. Weak exciton-photon coupling results in a modification of the exciton lifetime, the spectral shape, and the angular dispersion of emission from the microcavity. Conversely, when the lifetimes of the exciton and cavity photon are long enough so that an interaction occurs prior to either state decaying, the regime of strong exciton-photon coupling is realized. The timescale for coupling is the Rabi period, which depends on exciton and cavity parameters including the exciton oscillator strength and transition linewidths. The eigenstates of the strongly coupled system are known as microcavity polaritons. Microcavity polaritons have unique properties arising from their mixed exciton-photon character, permitting the realization of novel optoelectronic devices. Organic semiconductors are attractive for application in strongly coupled systems due to their large exciton binding energy (~1 eV), which permits a robust coupled state that is stable at room temperature and under electrical excitation. In addition, organic semiconductors exhibit large exciton oscillator strengths (~10^{15} cm^{-2}) resulting in a strong interaction between the cavity photon and the exciton. We aim to better the understanding of polaritons in organic semiconductor microcavities to push the field towards novel optoelectronic devices.

Table of Contents

List of Tables

List of Figures

Chapter 1 A Review of Organic Semiconductors

1.1 Introduction

Semiconductors are broadly classified as materials with conductivities between that of metals and insulators.[1] The study of these materials has led to the discovery of many electronic devices which are instrumental to the way society functions. Examples include light-emitting devices (LEDs), photovoltaic cells (PVs), photo-detectors, optical and electrical amplifiers, lasers, transistors, etc.[1-4] To date, the vast majority of commercially available products incorporating electronic devices are comprised of inorganic semiconductors such as Si, Ge, GaAs, etc.[1,4] For example, direct band gap semiconductors, like GaN and GaAs, are commonly used materials in LEDs and lasers, while integrated circuits are typically fabricated from Si.[1,3,4] It was not until the fundamental demonstrations of an efficient organic photovoltaic cell (OPV) and light-emitting device (OLED) by Tang that organic semiconductors began to also receive consideration as active materials in optoelectronic devices.[5,6] This work signaled the beginning of an organic electronics revolution, which has allowed for the demonstration of high performance organic electronic and optoelectronic devices.[5-29]

Organic semiconductors are a broad class of materials exhibiting a variety of interesting properties.[30] For example, these materials are particularly well-suited for use as light-emitters given their broad luminescence spectra and potential for near continuous tunability across the visible spectrum.[30] The broad absorption spectra of organic semiconductors make them exceptional materials for employment in PVs as well.[30]

Beyond their excellent optoelectronic properties, organic semiconductors are Van der Waals solids, rendering them compatible with high-throughput processing techniques and compatible with a wide variety of substrates including glass, metal foil, plastic, etc.[31-34] This potential for low-cost processing has driven the substantial interest in these materials as a platform for next generation optoelectronics.[18,23-29,31-46]

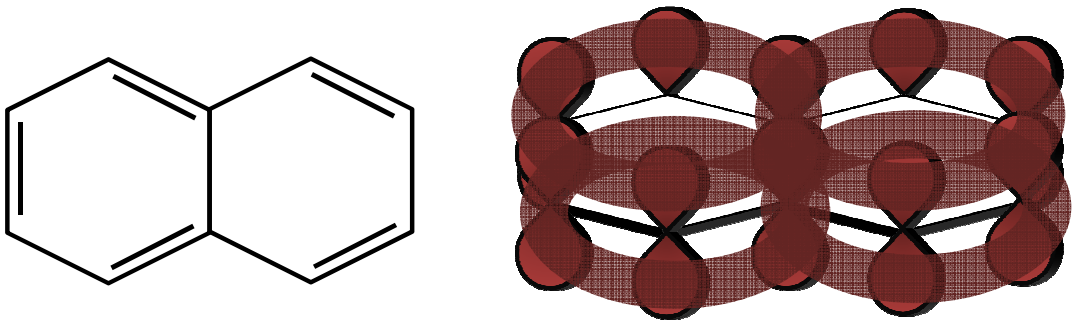

Figure 1.1 (a) The molecular structure of naphthalene, a conjugated molecule exhibiting, by definition, alternating single and double bonds. (b) Schematic showing the non-hybridized p orbitals, π-bonding and the resulting electron delocalization.

1.2 Organic Molecules as Semiconductors

Organic materials, defined as any compound containing carbon, are generally classified as insulators. Conjugated organic small molecules and polymers, however, are the exception (Fig. 1a).[30] In these materials, two of the three mutually orthogonal p orbitals of carbon mix with the 2s orbital to form three hybridized sp^2 orbitals. The residual p orbital remains unaltered and is oriented perpendicular to the plane of the sp^2 hybridization. The spacing between neighboring carbon atoms in a conjugated molecule results in overlap of the non-hybridized p_z orbitals. In this case, the p-orbitals create a π-

bond establishing a delocalized cloud of electrons (Fig. 1b).[30] It is the delocalized electrons which strongly determine the optical and electrical functionality of the material.

The delocalized electrons in these materials form the highest-energy occupied molecular orbital (HOMO) and lowest-energy unoccupied molecular orbital (LUMO) energy levels.[30] The HOMO and LUMO levels in a molecular system are qualitatively analogous to the valence and conduction bands of an inorganic semiconductor. Ultraviolet photoelectron spectroscopy (UPS) and inverse photoelectron spectroscopy (IPES) are used to determine the position of the HOMO and LUMO, respectively.[30] As such, the HOMO is the ionization potential while the LUMO is the electron affinity.[47,48] As in inorganic semiconductors, the gap in energy between the HOMO and LUMO is comprised of unavailable states and is termed the energy gap. The energy gap is realized from optical absorption measurements.

1.3 Molecular Excited States

When an electron is excited from the ground state (HOMO) to an excited state via absorption of electromagnetic radiation (light), a hole is left behind in the HOMO (Fig. 1.2). The low dielectric constant of organic semiconductors results in a strong coulomb attraction between the negatively charged electron and positively charged hole. The consequence is a tightly bound electron-hole pair referred to as a Frenkel exciton.[30] Optical or electrical excitation of organic semiconductors leads to the formation of Frenkel excitons. This is inherently different than the case of inorganic semiconductors

where optical excitation leads to free electrons and holes, or a loosely bound Wannier-Mott exciton.[30]

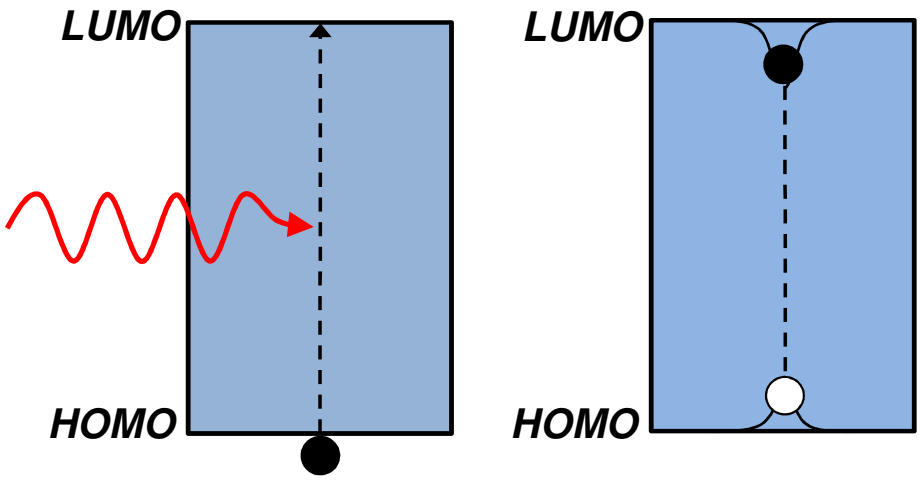

Figure 1.2 The highest-energy occupied molecular orbital (HOMO) and lowest-energy unoccupied molecular orbital (LUMO) energy levels in a molecular system. An electron is excited from the ground state (HOMO) to an excited state (LUMO) via absorption of electromagnetic radiation (light). This results in a strong coulomb attraction between the negatively charged electron and positively charged hole left behind in the HOMO. The consequence is a tightly bound electron-hole pair or Frenkel exciton.

The difference is manifested in the exciton binding energies of organic and inorganic semiconductors. Due to the large dielectric constant of inorganic semiconductors, the electron is electrostatically shielded from the hole resulting in a weakly bound Wannier-Mott exciton.[30,49] For example, the exciton binding energies of CdTe and GaAs are 4.8 meV and 10.0 meV, respectively.[49] At room temperature, the thermal energy ~25 meV is more than enough energy to dissociate the exciton into free charge carriers in the valence and conduction band. In contrast, the exciton binding energies of organic semiconductors can be >100 meV leading to robust excited states that are stable at room temperature and under high electrical and optical excitation densities.[30]

Careful consideration of the differing binding energies of organic and inorganic semiconductor excitons is imperative when studying exciton-photon coupling in optical microcavities (discussed in Chapter 2).

1.3.1 Singlet and Triplet Excitons

When an exciton is created via absorption of electromagnetic radiation, an unpaired electron (often referred to as a hole in the context of excitons) is left behind in the HOMO energy level. The unpaired electron in the HOMO and the electron excited from the HOMO to LUMO can assume two different spin orientations. Consequently, four different spin combinations are possible for the exciton.[50] The possible orientations can be well understood by considering a simple vector model for the electron spin states (Fig. 1.3). Each carrier is visualized as being a rotating vector (about the z-axis) generating orbital momentum.[50] Each vector can either be spin up or spin down, corresponding to the direction of orientation. The total spin of the exciton is calculated by adding the spin vectors of the constituents. A triplet exciton is formed when the two spins are precessing in-phase producing a total spin of S=1 shown in Fig. 1.3.[50] If the spin vectors are rotating out of phase, they are oriented anti-parallel and collinear resulting in exact cancellation and a net spin of S=0 (singlet).[50] Singlet and triplet states differ in both their energy level structure and in their transition lifetimes.

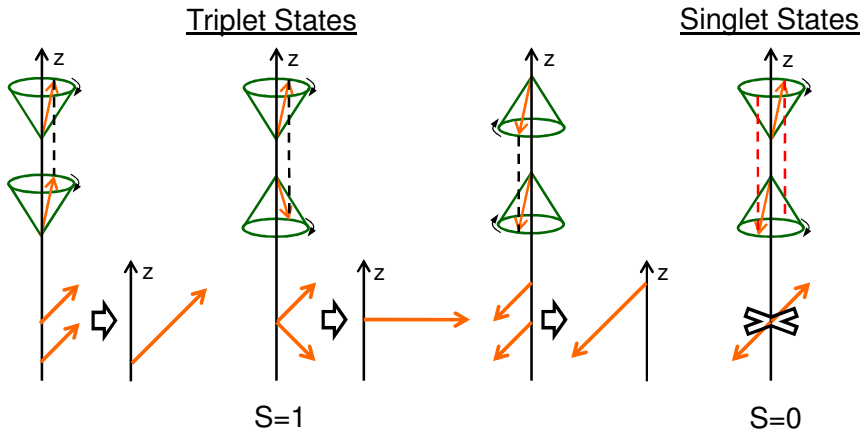

Figure 1.3 Vector schematic of triplet and singlet excitons. Triplet excitons have in-phase spins and thus a net spin S=1. Singlet excitons have anti-parallel spins resulting in a net spin S=0.

1.3.2 Electronic Transitions in Organic Semiconductors

The electronic transitions of organic semiconductors are usually depicted using a Jablonski diagram.[51,52] Figure 1.4 shows a generic energy level diagram for an organic semiconductor. S_0, S_1, and S_2 refer to the ground state singlet, 1st excited state singlet and 2nd excited state singlet, respectively.[30] Each excited state contains vibronic transitions denoted as 0, 1 and 2. When an organic semiconductor is excited optically through absorption, an excited state is created (S_1, S_2 or S_n). From the excited state, the exciton rapidly relaxes to the lowest vibronic level (0) of the lowest energy excited state (S_1). This process is referred to as internal conversion and is accompanied by a dissipation of energy in the form of heat (phonon emission). Following internal conversion, the S_1 excited state generally relaxes from the lowest vibronic level of the electronic manifold to any vibronic level in the ground state (known as Kasha's Rule).[30] In the simplest picture, the relaxation process can occur via two different mechanisms, radiative or non-radiative decay, each specifies the method of energy dissipation through emission of photons or

phonons, respectively. The former is referred to as luminescence. The rates of each decay process determine the emission efficiency or photoluminescence efficiency, Φ_{PL}:[50]

$$\Phi_{PL} = \frac{k_R}{k_R + k_{NR}} = \frac{k_R}{k_{TOT}} \tag{1.1}$$

In Equation 1.1, k_R and k_{NR} denote the rates of radiative and non-radiative decay, respectively. The non-radiative decay rate strongly impacts the photoluminescence (PL) efficiency. Additional sources of excited state decay could be separately accounted for by including additional terms in the denominator of Eqn. 1.1. These may include bimolecular quenching and intersystem crossing.[53,54]

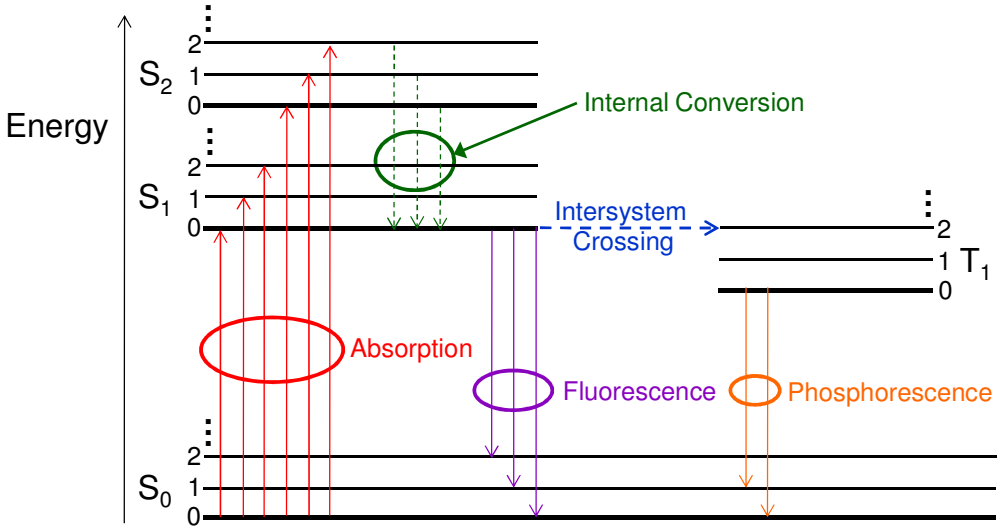

Figure 1.4 Energy level diagram for a generic organic semiconductor. S_0 is the ground state of the molecule. S_1 is the first excited state. The 0, 1, and 2 designate vibronic sublevels. In some cases, excited states may undergo intersystem crossing to triplet excited states which are represented as T_1.

Intersystem crossing is a process by which a singlet exciton is converted to a triplet. Such a transition is quantum mechanically unfavorable due to the required spin flip and thus is unlikely for most organic semiconductors.[50] Nevertheless, once an exciton is converted to a triplet (T_1), it may undergo further relaxation to the ground state

singlet through radiative or non-radiative decay. The former is referred to as phosphorescence. Typically, triplet states in organic semiconductors are non-emissive and thus undergo non-radiative decay to the ground state. This is attributed to the spin flip requirement for a triplet exciton to radiatively relax to the ground state singlet.

Phosphorescence, however, is enhanced in a number of organic semiconductors exhibiting large spin-orbit coupling.[50] Spin-orbit coupling is an interaction of the electrons motion with its spin. The specific mechanism responsible is the magnetic torque applied to the electron as it approaches the nucleus.[50] This effect increases as the atomic mass of the nucleus increases, hence, molecules comprised of heavy metal atoms, such as Ir, Pt, Pd Eu, etc., have a greater probability of exhibiting large spin-orbit coupling.[50] Large spin-orbit coupling generally provides enough torque to allow for exciton spin flips, effectively making the transition from singlet to triplet more probable. In these systems, the singlet and triplet states are effectively mixed allowing for efficient phosphorescence and intersystem crossing.[8-10,19,46,55-61]

The relaxation dynamics or timescales of the processes described above and shown in Fig. 1.4 ultimately dictate what transitions will occur following the excitation of an organic semiconductor. For example, vibronic transition rates (~10^{12} s^{-1}) are much faster than fluorescence rates and thus rapid relaxation occurs prior to fluorescence (~10^{9} s^{-1}).[52] In large spin-orbit coupling systems, intersystem crossing may occur before fluorescence and the phosphorescence rate is drastically enhanced (~10^{6} s^{-1}) resulting in efficient triplet luminescence.[8,30,50,55,56,58] The relative rates of the processes in Fig. 1.3 are summarized in Table 1.1.

Table 1.1 Summary of the transition rates of the processes in Fig. 1.3.[50]

Process	Rate [s^{-1}]
Absorption	10^{15}-10^{16}
Internal Conversion	10^{12}
Fluorescence	10^{9}
Intersystem Crossing	10^{4}-10^{12}
Phosphorescence	10^{-2}-10^{6}

1.3.3 Optical Transitions

The probability for a particular transition to occur goes beyond the simple Jablonski diagram exhibited in Fig. 1.4. Fermi's golden rule states that the transition probability (λ_{if}) depends on the strength of coupling between the initial and final state and the number of ways the transition can happen (i.e., the density of final states, ρ_f):[30]

$$\lambda_{if} = \frac{2\pi}{\hbar}\left|M_{if}\right|^2 \rho_f, \tag{1.2}$$

where ħ is the Dirac constant and M_{if} is the matrix element for interaction between the initial and final state. The matrix element can be written in the form of an integral where the interaction causing the transition is expressed as a potential V operating on the initial state wavefunction (Ψ_i):[30]

$$M_{if} = \int \Psi_f^* V \Psi_i \, \partial v, \tag{1.3}$$

where Ψ_f is the final state wavefunction. The integral is over all space (dv) and takes on the form of an expectation value which is the expected average value of a physical quantity in quantum mechanics. In this case, Eqn. 1.3 represents the expectation value of

the transition dipole moment. The transition probability is thus proportional to the square of the expectation value of the transition dipole moment and the density of final states.[30]

In a more simplified depiction, the transition probability is determined by the wavefunction overlap between the initial and final state.[30] Both the initial and final state for the molecular orbital can be represented as parabolic potential wells with discrete energy levels corresponding to vibronic transitions. The absorption intensities are thus determined by the wavefunction overlap between the 0^{th} vibronic level of the ground state S_0 and any of the vibronic levels in the excited state S_1.[30] Conversely, the fluorescence intensities are determined by the wavefunction overlap of the 0^{th} vibronic level of S_1 and any vibronic level of S_0.[30] As a result, the fluorescence of a particular organic molecule reveals the vibronic character of the ground state, while absorption reveals the vibronic character of excited states. Both of these processes are shown in Fig. 1.5 along with the resulting spectra based on the wavefunction overlap. The red-shift between the fluorescence and absorption is a result of the Frank-Condon principle.[30] Following absorption, the nuclei re-order within the molecule before emission occurs. This re-ordering causes a shift of the nuclear coordinate (R, Fig. 1.5) of the molecule as compared to the ground state.[50]

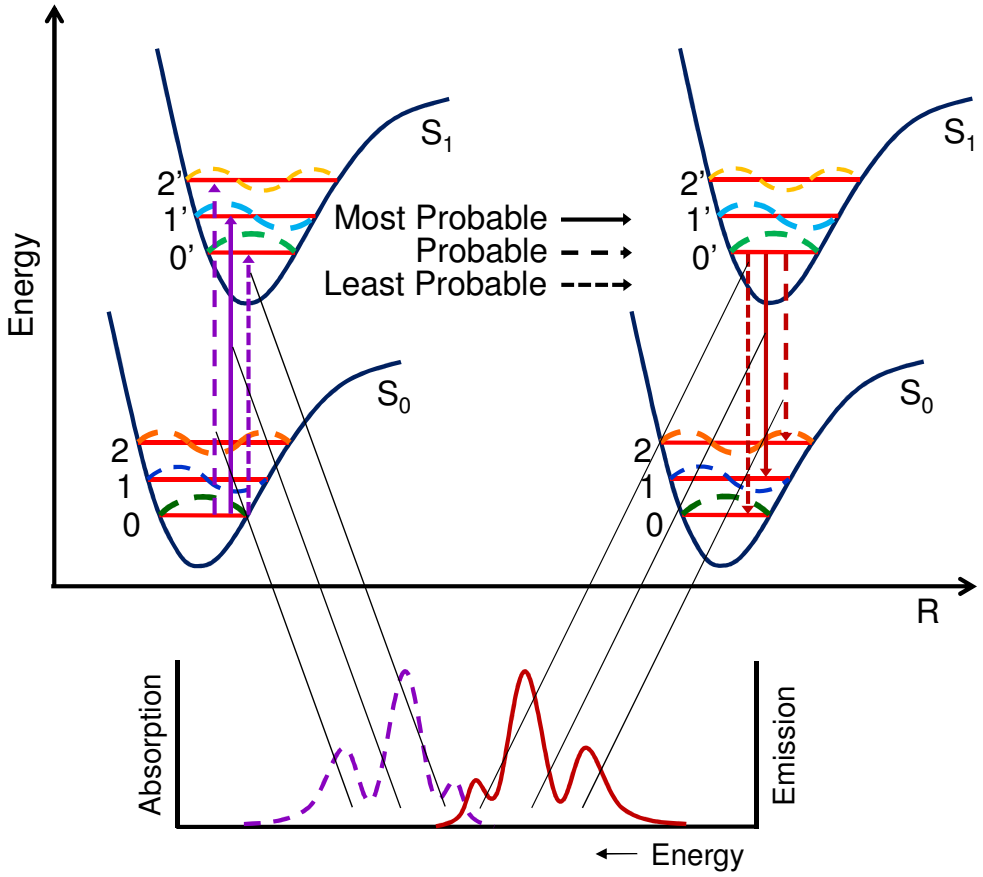

Figure 1.5 Illustration of Fermi's golden rule. Emission and absorption probabilities are determined by the overlap of the excited and ground state wavefunctions. The relative intensities of the absorption and emission features are determined by the magnitude of the overlap.

1.4 Excited State Energy Transfer

The transfer of energy between like or dissimilar molecules is extremely important when considering the design of high efficiency OLEDs and PVs, or the migration of excitons in a film.[8,9,46,57-60] For example, doping highly fluorescent guest molecules into a host film has shown to improve the efficiency of an OLED.[7] This method takes advantage of the large photoluminescence efficiency of the dilute guest

molecule, reducing the degree of exciton quenching often observed in neat solid films. There are three mechanisms responsible for exciton energy transfer.

1.4.1 Cascade Energy Transfer

Cascade energy transfer (or trivial energy transfer) is a process by which an exciton is transferred via emission of a photon from a donor molecule which is re-absorbed by an acceptor molecule.[50] The rate of such a process is reliant on the emission efficiency of the donor, the acceptor absorption cross-section coefficient and the spectral overlap between the emission spectrum of the donor and the absorption spectrum of the acceptor.[50] This process can be a long range process, typically more than 100 Å.[30]

1.4.2 Förster Energy Transfer

Förster transfer is another mechanism for excitonic energy transfer. It occurs between an excited molecule (donor) and non-excited molecule (acceptor). When there exists spectral overlap between the fluorescence of the donor and the absorption of the acceptor, an energetic resonance can be established between the two molecules. The oscillation of the electron in one molecule sets a ground state electron of the other into motion through a Coulombic dipole-dipole interaction.[51] This results in the ground state electron being excited into oscillation and the exciton being de-excited. In this process, the exciton is transferred whole between the two molecules. Figure 1.6 schematically shows the Förster transfer process. The rate of Förster transfer is expressed as:[50]

$$K_{D\to A} = \frac{1}{\tau_D}\frac{1}{R^6}\left(\frac{3}{32\pi^4}\int \frac{c^4}{\nu^4 n_0^4} F_D(\nu)\,\sigma_A(\nu)\partial\nu\right), \tag{1.4}$$

where τ_D ($\frac{1}{k_R+k_{NR}}$) is the natural lifetime of the donor molecule in the absence of quenchers, R is the radius between the two molecules (donor and acceptor). c is the speed of light, n_0 is the refractive index of the surrounding medium, F_D is the normalized fluorescence spectrum of the donor and σ_A is the acceptor absorption cross section in units of cm^2. The rate can be rewritten in terms of a critical transfer radius (R_0) or Förster radius, which represents the distance where all other decay mechanisms are as equally probable as Förster energy transfer.[50]

$$K_{D\to A} = \frac{1}{\tau_D}\left(\frac{R_0}{R}\right)^6 \tag{1.5}$$

The value of the critical transfer radius (or Förster radius) is characteristically ~10's Å for organic systems.[30]

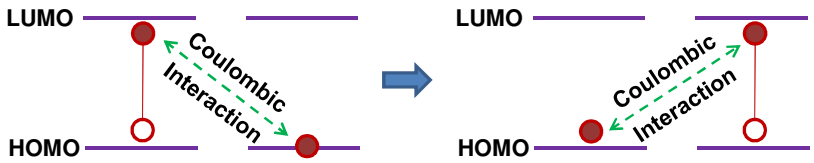

Figure 1.6 Schematic of the Förster energy transfer process.

1.4.3 Dexter Energy Transfer

The final exciton energy transfer mechanism is known as Dexter transfer. This process requires a physical overlap of the electron clouds of the donor and acceptor molecules. An exchange of an electron from the HOMO of the acceptor to the HOMO of the donor simultaneously with an electron exchange from the LUMO of the donor to the LUMO of the acceptor completes the transfer process (see Fig. 1.7 for a schematic). Expectedly, this is a much shorter range process than either Förster or cascade energy transfer.

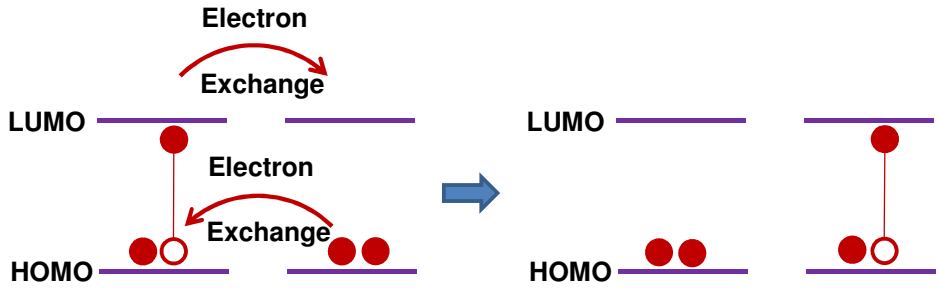

Figure 1.7 Schematic of the Dexter energy transfer process.

The Dexter transfer rate is quantified by the following equation:[50]

$$K_{D\to A} = K\exp(-2R/L)\int F_D(\nu)A_A(\nu)\,\partial\nu \qquad (1.6)$$

$F_D(\nu)$ is the normalized fluorescence spectrum of the donor, $A_A(\nu)$ is the normalized absorption spectrum of the acceptor, R is the molecular separation, L is the Van der Waals radius and K is related to the specific orbital interactions. The specific orbital interaction term contains information regarding the wavefunction overlap between donor and acceptor molecules. Contrary to Förster energy transfer, the Dexter process is not dependent on the absorption strength of the acceptor. Energy transfer between triplet excitons is typically best described as a Dexter transfer process. The exponential term leads to a short range interaction, relevant for length scales of 5-10 Å.[50]

1.5 Charge Transport in Organic Semiconductors

Organic semiconductor thin films are weakly bound by Van der Waals forces and can therefore assume various degrees of crystallinity based on the growth conditions. Typically, two extremes of crystalline order are considered in the context of charge transport, ordered and disordered, which indicate crystalline and amorphous, respectively.[30,62] Crystalline materials are typically modeled with a band transport

model, while a hopping transport model is employed for amorphous materials.[30] In each case, the mechanism for charge transport is characterized by the magnitude and temperature dependence of the charge carrier mobility.[30] The mobility characterizes how quickly a charge carrier can move through a solid when subjected to an electric field and can vary significantly in magnitude depending on the transport mechanism. Typically, the transport properties of a given organic semiconductor fall somewhere in between the extreme cases of hopping and band transport. The hopping model emphasizes the molecular character of conduction states while the band model emphasizes the collective character of conduction states.[30]

1.5.1 Band Transport

Band theory, initially developed by Bloch, is sufficient to elucidate charge transport in crystalline inorganic and organic semiconductors.[4] The theory assumes that a single valence electron moves in a periodic potential established by the ion cores of the crystalline solid. The solution to the Schrödinger equation, in this case, is represented by a periodic wavefunction dependent on the wavevector (position in the crystal) and potential. For discrete values of the wavevector and potential, there are a number of allowed energies (solutions) for a Bloch electron wavefunction.[4] The ranges of allowed energies are called energy bands and the excluded energies are termed band gaps. In the case of semiconductors, the band gap between empty (conduction band, LUMO) and filled (valence band, HOMO) energy bands is small, resulting in a significant population of electrons in the empty band at room temperature. Electrons in the partially empty

band are free to move and conduct. The band transport mechanism is characterized by the following temperature (T) dependence on mobility (μ):[30]

$$\mu \propto T^{-n}, n > 1 \quad (1.7)$$

The constant n is determined experimentally and is material dependent. This model breaks down when adjacent molecules have weak wavefunction overlap and the assumed periodicity of the crystal is disrupted.[62]

1.5.2 Hopping Transport

In disordered films, the charge carrier is highly localized and moves by hopping transport.[30] Hopping transport can be visualized as a thermally activated, random walk (Fig 1.8a) of a carrier about a random array of sites within the semiconductor.[43] Figure 1.8b illustrates a very simple interpretation of hopping conduction in a disordered solid. Electrons or holes are localized on individual molecules in potential wells. Due to the random orientation of the molecules in the solid, each potential well has a different distribution of energy levels associated with it.[30] Carriers must overcome a potential barrier to hop from one well to another. As a result, hopping is an activated process. The energy to promote a hop from one molecular site to the next is obtained from the thermal energy (phonons) of the system. An expression governing the hopping mobility (μ) is given as:[30]

$$\mu \propto exp(-E_A/k_BT) \quad (1.8)$$

where E_A is the activation energy, T is the temperature, and k_B is the Boltzmann constant. The exponential term represents the probability of a carrier acquiring the activation energy necessary to escape the potential well and hop to the next lattice site.

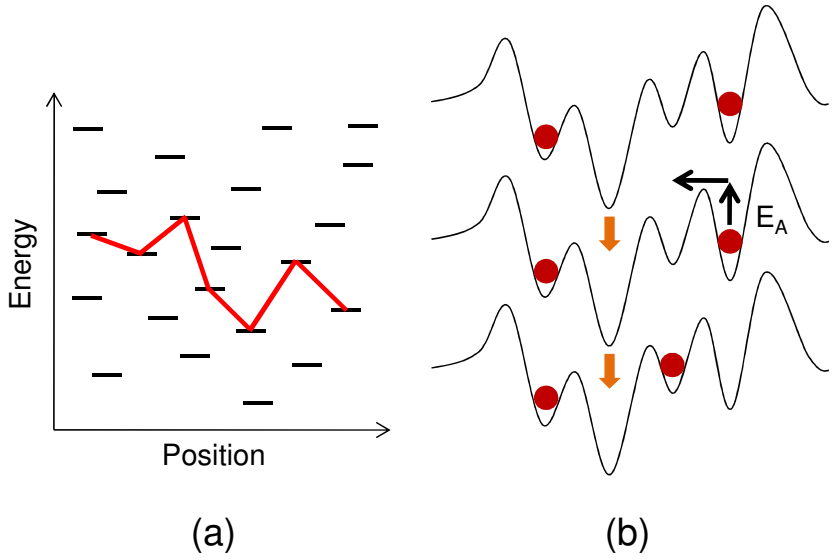

Figure 1.8 (a) Energy versus position schematic of hopping conduction. The red line demonstrates a potential charge carrier path. (b) Carrier moves from one potential well to another by overcoming the activation energy (E_A).

1.6 Organic Optoelectronic Devices

In the previous sections the electrical and optical properties of organic semiconductors were discussed. Due to these properties, organic semiconductors are excellent candidates for inclusion into a variety of optoelectronic devices. This section reviews a variety of these devices and their operating principles. Prior to this discussion it important to distinguish two subsections of organic semiconductors.

Organic semiconductors are grouped into two categories based on their molecular weights. Small molecules have molecular weights less than 1000 g/mol, while polymers are repeating chained structures that have molecular weights exceeding 1000 g/mol.[30] One key difference between the two materials are the processing techniques that are often

used for device construction. Polymers are dissolved in a suitable solvent and deposited by solution-based techniques such as spin-coating or ink-jet printing, whereas small molecules are most frequently deposited by thermal evaporation.[25,30-34,39,63] All of the work in this thesis is based on small molecule materials, and the following discussion is tailored to this subsection of organic semiconductors.

1.6.1 Organic Light-Emitting Devices (OLEDs)

High efficiency organic light-emitting devices (OLEDs) typically consist of three or more thin layers of organic semiconductors sandwiched between two electrodes.[11,20,64] In the simplest device architecture (Fig. 1.9), one layer is specifically designed to transport holes (the hole transport layer or HTL), another to transport electrons (the electron transport layer or ETL) and a third to serve as the location for exciton recombination (known as the emissive layer or EML). Electrons and holes are injected into the ETL and HTL from the cathode and anode, respectively. Injected electrons and holes migrate toward the oppositely charged electrodes through their respective transport layers until they reach the EML.[20,64] In the EML, the electron and hole form an exciton which may radiatively decay. This process is indicated schematically in Fig. 1.9 in terms of the HOMO and LUMO energy levels of each material in the device.

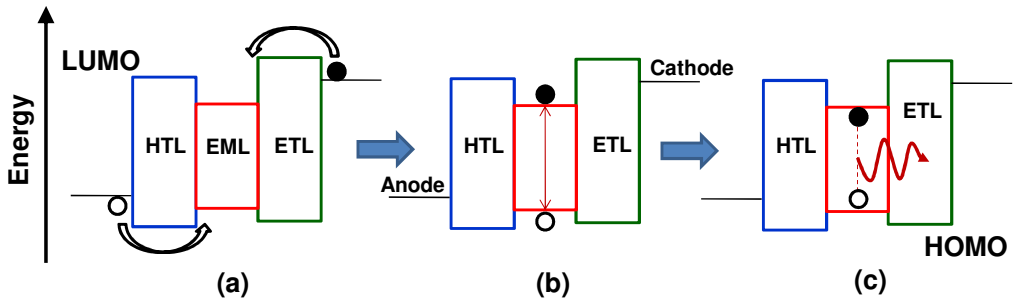

Figure 1.9 Schematic representation of operating principles behind an OLED. (a) Electrons (black dots) and holes (white dots) are injected onto the electron and hole transporting layers (ETL and HTL, respectively) via their respective electrodes. (b) Exciton formation occurs in the emissive layer (EML) followed by radiative recombination (c).

The energy alignment for the HTL, ETL and EML are as shown in Fig. 1.9. The LUMO of the HTL is higher than the LUMO of the EML so that electrons are confined on the EML.[10] Equivalently, the HOMO of the ETL is lower in energy than the HOMO of the EML to "trap" holes. This energy arrangement enhances the probability of exciton formation in the EML.[10] Also, the EML serves as a confinement layer for excitons, which eliminates exciton quenching at organic semiconductor-metal interfaces.

There are four inherent processes essential to OLED operation and thus efficiency. The product of the four equals the external quantum efficiency (η_{EQE}) of the device or the fraction of emitted photons to injected charge carriers:

$$\eta_{EQE} = \gamma\chi\phi_{PL}\eta_{OC} \tag{1.9}$$

The first process is charge balance (γ). Charge balance is defined as the ratio of injected electrons to holes in the emissive layer. Charges injected into the EML that do not form excitons result in loss. In well designed OLEDs based on the concepts discussed above, balanced injection of electrons and holes is achieved and hence $\gamma \sim 1$.[10] Next, is the spin fraction (χ). As a consequence of the number of possible spin orientations discussed in

Sec. 1.3.1 and shown in Fig. 1.3, 25% of the excitons created under electrical excitation are singlets while the remainder are triplets.[8,9,46,57-60,65] As discussed in Sec. 1.3.1, triplets typically do not emit and the spin fraction is therefore 0.25.[10] However, for phosphorescent OLEDs, where the emissive layer is comprised of a material exhibiting large spin-orbit coupling (phosphorescent material) or a host doped with a phosphorescent material, emission is permitted from triplet states raising the spin fraction to unity.[8,9,46,57-60,65] The PL efficiency (Φ_{PL}, Sec. 1.3.2) of the material exciton is the source of the third component. This can approach unity for EMLs designed to reduce non-radiative decay processes such as a host/guest system.[58] Finally, outcoupling efficiency (η_{OC}), or the amount of light that is forward emitted from the device, is the last product of the external quantum efficiency. A large amount of generated light is lost to waveguided modes in the glass substrate, and ITO/organic layers due to refractive index differences between adjacent layers (Fig. 1.10). In general, this is the major loss mechanism of OLEDs and is typically <0.2.[10] Multiplying all of these efficiencies together would give an OLED efficiency of ~20 percent.

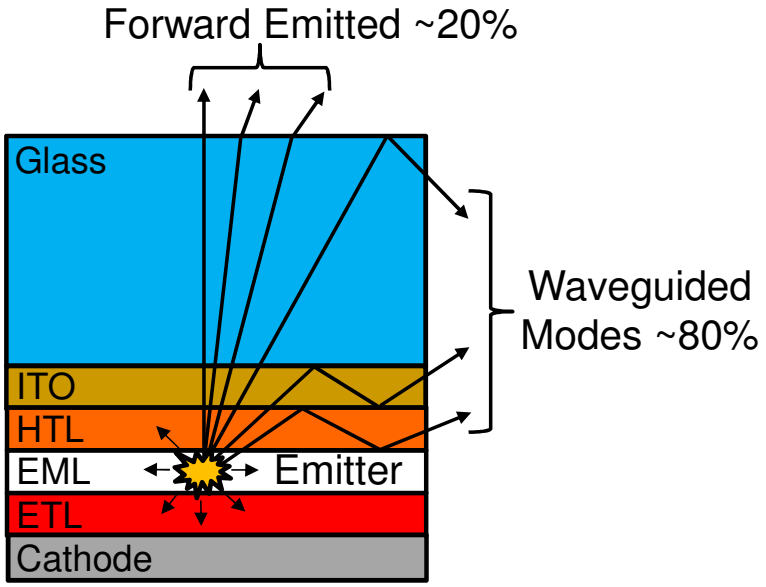

Figure 1.10 Due to refractive index differences between adjacent layers in an OLED, a large fraction of the light created is lost to waveguided modes in the glass substrate and ITO/organic layers. The amount of light that is forward emitted is referred to as the outcoupling efficiency (η_{OC}).

1.6.2 Organic Photovoltaic Cells (OPVs)

Organic photovoltaic cells convert optical power to electrical power. Contrary to inorganic solar cells which typically consist of a single material, usually a pn homojunction, organic OPVs require an exciton dissociating interface. Thus, the simplest conceivable architecture is a bilayer device consisting of an electron donor and acceptor as shown in Fig. 1.11.[21-29,45] When the device is subjected to an incident optical field absorption occurs in the donor and acceptor layer with an absorption efficiency (η_A) (Process 1, Fig 1.11). Once a photon is absorbed, an exciton is created which diffuses toward the donor-acceptor interface characterized by an exciton diffusion efficiency (η_{ED}) (Process 2, Fig. 1.11).[23] If the LUMO energy offset between the donor and acceptor is

greater than the binding energy of the exciton, the exciton is dissociated into a free electron and free hole on the acceptor and donor, respectively (Process 3, Fig. 1.11).[21,22,27] An analogous process occurs for an exciton created on the acceptor if the HOMO energy offsets are greater than the exciton binding energy. The exciton dissociation process is quantified by an efficiency termed the charge transfer efficiency (η_{CT}). Finally, the carriers are swept out of the device toward their respective electrodes with a charge collection efficiency (η_{CT}) (Process 4, Fig. 1.11).[23] The device external quantum efficiency (η_{EQE}) or the number of collected carriers to incident photons is given as the product of the efficiencies of the four processes discussed above.[23]

$$\eta_{EQE} = \eta_A \eta_{ED} \eta_{CT} \eta_{CC} \tag{1.10}$$

Efficient device operation requires that the four processes summarized in Fig. 1.11 be maximized.

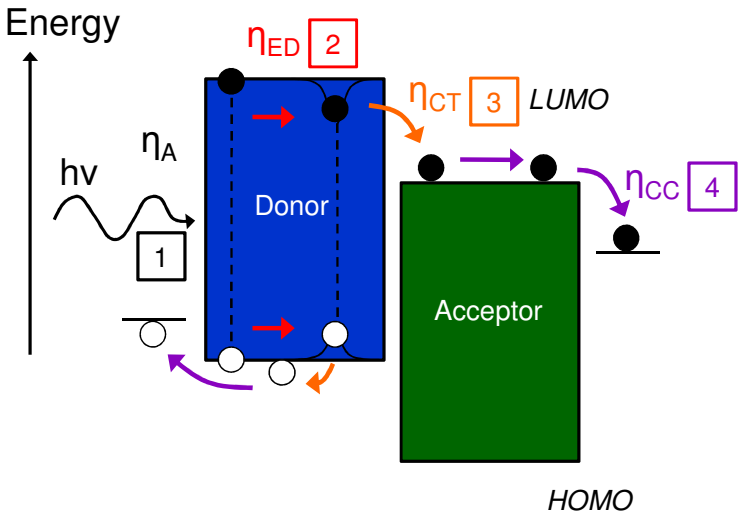

Figure 1.11 The operation of an organic photovoltaic cell. Light absorption leads to the formation of excitons (Process 1) which diffuse toward the donor acceptor interface (Process 2). At the donor acceptor interface, the exciton is dissociated (Process 3) into a free electron (black dot) and a free hole (white dot). The carriers are then swept out of the device and collected at the electrodes (Process 4).

1.6.3 Organic Lasers

There are three possible interactions between a system of organic semiconductor molecules and light.[66] One possible interaction is as simple as absorption accompanied by the creation of an excited state, discussed in Sec. 1.3.2. Another possible interaction is the emission of a photon following absorption. This process is referred to as spontaneous emission and occurs stochastically with no phase relationship between photons emitted from a group of excited molecules.[66] The final possible interaction is termed stimulated emission. Stimulated emission is when a photon with energy equal to the energy gap between the excited state and ground state induces an excited molecule to emit.[66] This process results in two photons of equal energy and phase.

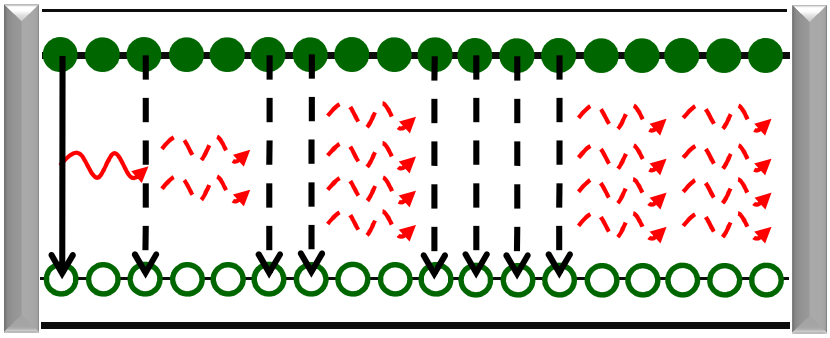

Figure 1.12 A simple schematic of a laser. An active medium is placed in an optical resonator comprised of two mirrors. The structure is pumped to create a population inversion. Initially, an excited state decays and stimulates emission from another excited state producing two coherent photons. The process continues throughout the active layer building up a large number of coherent photons. A laser is established when this coherent build up of photons overcomes the inherent losses in the system.

The operation of a laser under optical excitation relies on all three of the light-matter interactions described above. Initially, molecules are excited from the ground state to the excited state by a process called pumping.[66] The structure is pumped to create more excited states than ground states referred to as a population inversion. The excited

molecules decay via spontaneous emission resulting in the subsequent release of incoherent (no phase relationship) photons. The incoherent photons are fed back into the laser medium by an optical resonator (optical resonators will be discussed in more detail in Chapter 2). A fraction of the incoherent photons are re-absorbed by the molecules in the ground state, while a portion of photons cause stimulated emission of excited-state molecules, releasing a photon.[66] Multiple stimulated emission processes result in a large build-up of coherent photons within the resonator as shown in Fig. 1.12. If the number of coherent photons being created per pass (gain) in the optical resonator is greater than the inherent loss in the system, the net result is a laser.[66] Typically, pump power is increased until such losses are overcome. Lasing, by way of optical pumping, has been shown in a wide variety of small-molecule and polymer organics in various resonator geometries.[14-16,18,38,44,67-75]

1.7 Light-Matter Interactions in Organic Optoelectronic Devices

The central assertion in the optoelectronic devices discussed above is that excitons and light simultaneously exist in these structures. This allows for additional interactions between the light in the structure and the semiconductor exciton which can drastically alter the performance and behavior of the device. The nature of the interaction is determined by the relative magnitude of the lifetimes of the trapped light and exciton and a characteristic interaction time for the system known as the Rabi period.[76] For instance, if the exciton decays or the trapped light escapes before a complete Rabi period,

weak exciton-photon coupling occurs. In the weak coupling regime, the exciton and cavity photon behave independent of each other. Weak coupling modifies the emission characteristics of the exciton, both in terms of the spectral shape and excited state lifetime. The most obvious applications of weak coupling are photon mode lasers, optical amplifiers, microcavity light-emitting devices and photodetectors.[15,18,38,40,66,77-96] However, if the exciton and trapped light persist over a timescale longer than the Rabi period, the regime of strong coupling is reached.[76] In this case, a new quasiparticle is created, termed a polariton. Polaritons are a mixture of both light and exciton. Their allowed energy levels are split around the exciton energy where one polariton energy state is above the exciton energy (termed the upper branch) and one is below (termed the lower branch) as shown in Fig. 1.13. These interactions are not yet well understood in organic semiconductors. A thorough understanding of light-matter interactions is therefore paramount to realizing novel optoelectronic devices based on organic semiconductors.

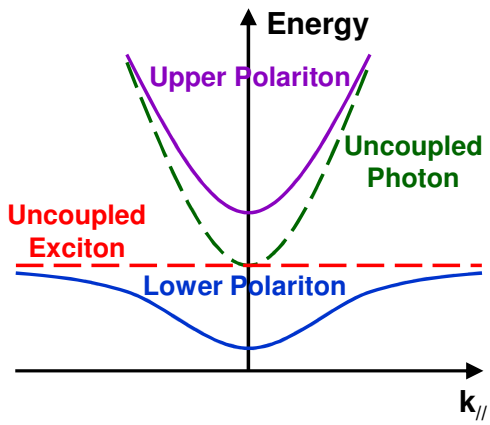

Figure 1.13 Allowed energies of polariton states versus in-plane wavevector or energy-wavevector dispersion (angle of incidence, discussed further in Chapter 2). The allowed energies of the polariton states (solid lines) are split around the exciton energy, one above (upper polariton branch) and one below (lower polariton branch).

Chapter 2 A Review of Microcavity Polaritons

2.1 Introduction

In Sec. 1.7 it was discussed that the interaction between an exciton and photon can alter the performance of organic optoelectronic devices and that the interactions are not yet well understood in these systems. The best way to study these interactions is in an optical microcavity, a structure utilized to more efficiently confine light to the semiconductor active layers.[96-98] This chapter provides a background of exciton-photon coupling in optical microcavities and the creation of microcavity polaritons. The first part of the chapter is dedicated to optical resonators and their properties. Next, the potential weak and strong coupling interactions between the light confined in the resonator and the organic semiconductor excitons are explained more thoroughly. Microcavity device physics will be examined with the intent of providing insight into potential applications. Finally, the properties of the organic semiconductors previously utilized in microcavities will be evaluated.

2.2 Properties of Optical Resonators

An optical resonator is a structure used to create large electromagnetic (E-M) field intensities without the need for large power inputs.[66] These cavities also strongly modify the photon density of states and may be as simple as two or more mirrors that "trap" an E-M wave by successive reflections.[96,97] The trapped standing wave has a wavelength

related to the dimensions of the structure and is termed a "mode" of the resonator. Often, resonators that have only a single mode are desired. In practice this can be done by reducing the size of the resonator to half a wavelength. This would ensure that only a single mode could exist inside the structure. From a fabrication standpoint this is a difficult task but not impossible if the intended wavelength range is the visible spectrum.[66] A Fabry-Perot (FP) cavity with wavelength dimensions is an example of such a resonator.[99]

2.2.1 Operating Principle of a Fabry-Perot Cavity

In its simplest incarnation, a FP cavity consists of two flat reflectors separated by a distance L. Figure 2.1a shows the schematics of a FP cavity and will serve as a visual for the following model which will be used to extract the resonant modes of the structure. Define r, t, r' and t' as the reflection (r) and transmission (t) coefficients of the reflectors for incident waves outside and inside (designated with a prime) of the cavity, respectively. If A_i is the electric field amplitude of the wave incident on the cavity, the amplitudes of the total reflected external wave (A_r) and total transmitted external wave (A_t) are:

$$A_r = A_i\left[r + tt'r'e^{i\delta}\left(1 + r'^2e^{i\delta} + r'^4e^{2i\delta} + \cdots\right)\right] \tag{2.1}$$

and

$$A_t = A_i tt'\left[1 + r'^2e^{i\delta} + r'^4e^{2i\delta} + \cdots\right]. \tag{2.2}$$

The exponential term $e^{i\delta}$ is the phase difference of the wave in one round trip of the cavity, which is explicitly calculated later in this section. Each amplitude term contains a geometric series permitting A_r (Eqn. 2.1) and A_t (Eqn. 2.2) to be written as:

$$A_r = \frac{(1-e^{i\delta})\sqrt{R}}{1-Re^{i\delta}} A_i \tag{2.3}$$

and

$$A_t = \frac{T}{1-Re^{i\delta}} A_i \tag{2.4}$$

also

$$\frac{I_r}{I_i} = \frac{A_r A_r^*}{A_i A_i^*} = \frac{4R\sin^2(\delta/2)}{(1-R)^2+4R\sin^2(\delta/2)}$$

$$\frac{I_t}{I_i} = \frac{A_t A_t^*}{A_i A_i^*} = \frac{1-R^2}{(1-R)^2+4R\sin^2(\delta/2)}, \tag{2.5}$$

where $R=r^2=(r')^2=rr'$, $T=tt'$ and $R+T=1$. It is assumed that the FP cavity mirrors are symmetric. To extract the resonant modes, an explicit expression for δ as a function of L is needed.

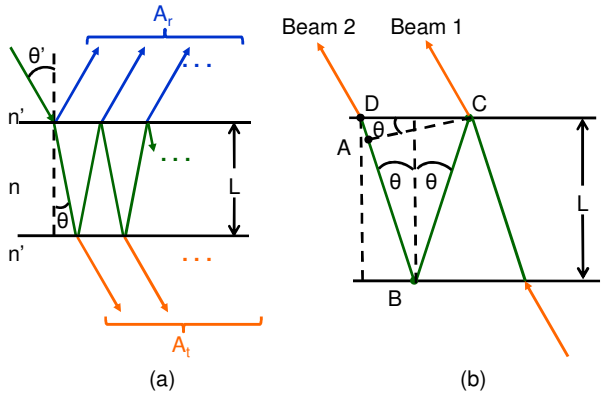

Figure 2.1 Schematic of an FP cavity. (a) Labels assigned for modeling in text. (b) Path difference "x" in one round trip of the cavity.

Figure 2.1b shows the path length difference encountered in one round trip of a FP cavity. This extended path length results in a phase difference of the wave between point C and D. If it is assumed that the waves in the FP resonator are plane waves, then

at point C in Fig. 2.1b, beam 2 is in-phase with beam 1. Then the path length difference is given by:

$$\delta L = AB + BC = \frac{L\cos(2\theta)}{\cos(\theta)} + \frac{L}{\cos(\theta)} = \frac{L}{\cos(\theta)}(\cos(2\theta) + 1) = 2L\cos(\theta) \quad (2.6)$$

Considering the equations of an electromagnetic wave and assuming no absorption, the round trip phase change(s) can be expressed in terms of δL as:

$$e^{i\delta} = e^{-ik\delta L}, \text{ since } k = \frac{2\pi n}{\lambda} \text{ implies } \delta = \frac{-4\pi nL\cos(\theta)}{\lambda} \quad (2.7)$$

Using Eqns. 2.5 and 2.7, the condition for maximum transmission (or analogously reflection) of the cavity can be calculated. For $\frac{I_t}{I_i} = 1$, the following must be true:

$$4R\sin^2(\delta/2) = 0, \text{ which implies } \nu_m = \frac{mc}{2nL\cos(\theta)} \quad (2.8)$$

Equation 2.8 defines the resonant modes of a FP resonator. The spacing between the modes, known as the free spectral range (FSR), is defined as:

$$FSR = \Delta\nu = \nu_{m+1} - \nu_m = \frac{c}{2nL\cos(\theta)} \quad (2.9)$$

A calculation of the spectral width of the resonance, again uses Eqn. 2.5 with $\frac{I_t}{I_i} = \frac{1}{2}$:

$$\frac{(1-R)^2}{4R} = \sin^2\left(\delta_{1/2}/2\right) \quad (2.10)$$

Applying a phase shift trigonometric identity,

$$\frac{(1-R)^2}{4R} = \sin^2\left(\frac{\delta_{1/2} - 2m\pi}{2}\right) \text{ assuming } \frac{\delta_{1/2} - 2m\pi}{2} \ll \pi \text{ gives } \delta_{1/2} = \frac{(1-R)}{\sqrt{R}} + 2m\pi \quad (2.11)$$

Neglecting the 2mπ phase shift and using Eqn. 2.7, the full-width-half-maximum ($\Delta\nu_{1/2}$) is:

$$\Delta\nu_{1/2} = \frac{c}{2\pi nL\cos(\theta)}\frac{(1-R)}{\sqrt{R}} \quad (2.12)$$

Finally, the number of resolvable frequencies can be calculated by taking the ratio of the FSR to the width of a mode since one mode is contained in each FSR (see Fig. 2.2). This quantity is called the Finesse (F) of the cavity. Calculated explicitly by dividing Eqn. 2.9 by Eqn. 2.12:

$$F = \frac{\pi\sqrt{R}}{1-R} \tag{2.13}$$

Figure 2.2 is a plot of transmission of a FP resonator as a function of frequency, providing an illustration of mode behavior. The transmission at a resonant frequency follows a shape like Fig. 2.2 for imperfect mirrors. For perfect reflectors (R=1), a delta function response would be expected. Accordingly, FP cavities with high finesse (high mirror reflectivities) show sharper transmission peaks (narrower linewidth) with lower minimum transmission coefficients (Fig. 2.2). Another figure of merit for a FP cavity is termed the cavity quality factor (Q) and is a measure of how efficiently light is confined within the structure. Mathematically, Q is expressed in terms of the mode full width at half maximum value ($\nu_{1/2}$) and the frequency of the mode (ν):

$$Q = \frac{\nu}{\Delta\nu_{1/2}} = \omega\tau_c \tag{2.14}$$

The quality factor can also be used to calculate the lifetime of a photon in the structure (τ_c) for a mode with angular frequency (ω) as exhibited by Eqn. 2.14. An important feature of a FP cavity is the ability to tune the resonant mode position by changing the separation between the reflectors (L) or the refracted angle inside the cavity (θ) (Eqn. 2.8).

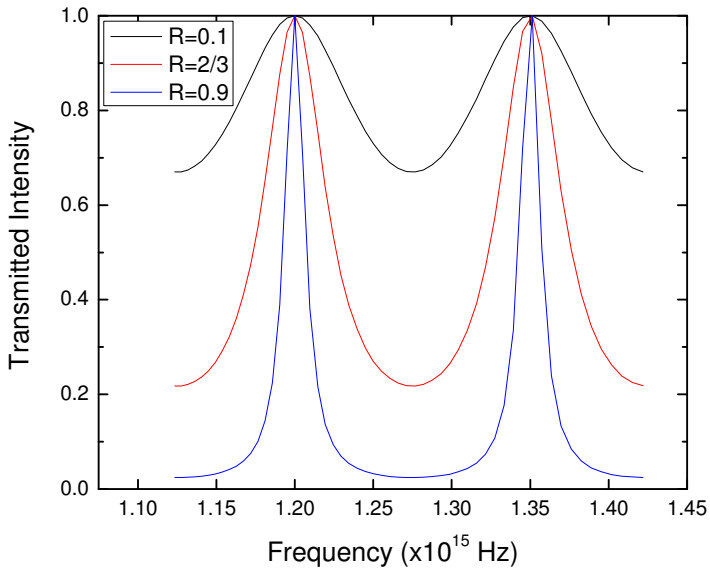

Figure 2.2 The modes of a Fabry-Perot resonator for different values of reflectivity. As reflectivity increases, the spectral width of the modes and minimum transmission deceases.

2.2.2 Angular Dispersion of the Cavity Mode

Previously, it was stated that a FP resonator with wavelength dimensions will exhibit single mode behavior. An example of such a resonator is a planar microcavity where large area (compared to wavelength dimensions) reflectors are separated by an integer multiple of half the wavelength.[99] In such a structure, off-normal modes become important due to the large difference in dimensions between the reflector spacing and area.[66] From Eqn. 2.8, it can be seen that the spectral position of the resonant modes in the cavity have both a mirror spacing dependence and a dependence on the angle of incidence. This implies that a mode can be scanned over a frequency range by changing the angle of light incident on the microcavity.

An important distinction to recognize is that the expression for the modes in a FP cavity (Eqn. 2.8) contains the refracted angle (θ in Fig. 2.1) inside the cavity rather than the angle of incidence (θ' in Fig. 2.1). Taking this minor issue into account, the angular dependence of a microcavity (cavity) mode can be derived by using Snell's law of refraction along with Eqn. 2.8:

$$\nu_m^2 = \frac{m^2c^2}{4n^2L^2\cos^2(\theta)} = \frac{m^2c^2}{4n^2L^2(1-\sin^2(\theta))} = \frac{m^2c^2}{4n^2L^2}\left(1-\frac{\sin^2(\theta')}{n^2}\right)^{-1}, \quad (2.15)$$

where n'=1 (index of air). It follows directly that the FP cavity mode energy (E_{ph}) is:

$$E_{ph} = E_0\left(1-\frac{\sin^2(\theta')}{n^2}\right)^{-1/2}, \quad (2.16)$$

where $E_0 = \frac{m}{2}\frac{hc}{nL}$. (2.17)

Since the perpendicular component ($k_\perp$) of the wavevector (k) in a microcavity is quantized in units of π/L (Fig. 2.3) as $k_\perp = \frac{m\pi}{L}$, Eqn. 2.16 can be modified by substituting Eqn. 2.17 and the definition of E_{ph} in terms of wavevector ($E_{ph} = \hbar ck$) and rearranging,[99]

$$E_{ph} = \frac{\hbar c}{n}\left[\left(\frac{m\pi}{L}\right)^2 + (k\sin(\theta'))^2\right]^{1/2} \quad (2.18)$$

Clearly, the term in the square brackets of Eqn. 2.1.8 is the total wavevector k. The first and second terms in the brackets are $k_\perp$ and the parallel wavevector ($k_\parallel$) respectively. Using Eqn. 2.18, the energy of the cavity mode can be mapped as a function of angle, which is termed the cavity mode dispersion. Figure 2.3 illustrates the concept of quantized $k_\perp$ and possible modes (standing waves) according to the following:

$$k_\perp = \frac{m\pi}{L} \text{ or } L = \frac{m\lambda}{2} \quad (2.19)$$

The concepts discussed in detail above are essential when analyzing the physics of cavity photons and their interaction with matter.

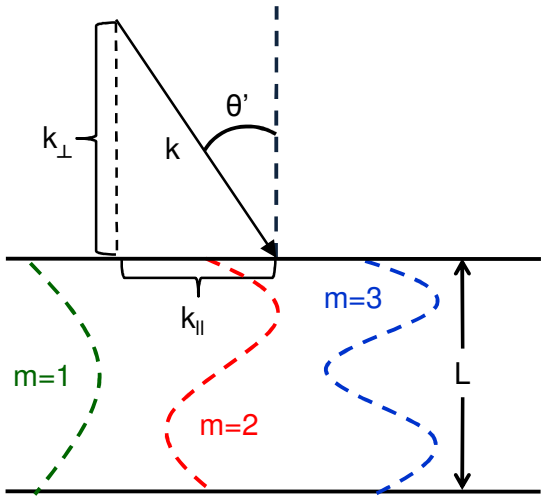

Figure 2.3 Schematic of the quantized perpendicular wavevector ($k_\perp$) and potential resonant modes of a FP cavity.

2.2.3 Absorbing Media in Microcavities

In the previous section an idealized case of an optical microcavity was analyzed where the material sandwiched between the mirrors was optically transparent. If this material is absorbing, the physics become markedly more interesting. Assuming that the cavity photon mode (or cavity mode) is resonant with the electronic excitation (exciton) of the cavity material, a competition arises between the strength of the exciton-photon interaction and their respective lifetimes.[76] The lifetime of the cavity photon mode is dictated by either the possibility of the photon being transmitted through or being absorbed by a reflector. Alternatively, the exciton lifetime is determined by the recombination lifetime.[98] The exciton dephasing time is important for realizing coherent polaritons.[100] An unperturbed exciton moves through a solid with a coherent, wave-like

motion.[101] This motion is disrupted when lattice vibrations or molecular vibrations scatter the exciton, resulting in a randomization of the exciton phase and thus making its motion incoherent.[101] Although exciton dephasing does not actually annihilate the exciton, it may be a challenge to coherent light emitters based on polaritons.[99]

The interaction between the exciton of a semiconductor and the photon mode of a cavity can be thought of as a periodic energy exchange between two oscillators. A mechanical analog to this condition is two pendula connected by a spring where the spring serves as a means of energy exchange as in Fig. 2.4. It becomes quite apparent that the operation of such a system is highly dependent upon the spring. Due to this fact, there are two different regimes that are possible. One in which the interaction is strong compared to the damping mechanisms of the two pendula and another where the interaction is weak compared to the damping mechanisms.[76,98,102]

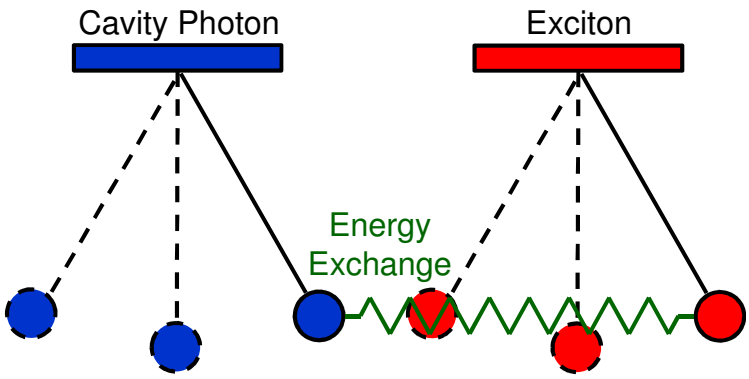

Figure 2.4 Two coupled pendula periodically exchanging energy through a connecting spring.

2.3 Microcavity Polaritons

This section describes the theories used to elucidate the physics exhibited by microcavity polaritons. These mathematical derivations provide a concrete

understanding of the physics of polaritons and also help to further explain their existence. The two theories discussed also form the foundation for more complex models which have been developed to explain microcavity polariton relaxation and excitation dynamics, luminescence, etc. A thorough understanding of the models discussed is essential to grasp the subject of microcavity polaritons.

2.3.1 Strong vs. Weak Exciton-Photon Coupling

Building off of the pendulum analogy discussed in Sec. 2.2.3, weak exciton-photon coupling occurs when the rate of damping of the exciton (dephasing time) and photon (lifetime in the cavity) are more rapid than the time for interaction between the two species.[76] In contrast, the strong exciton-photon regime is observed when the interaction is more rapid than the damping processes.[76] The different regimes result in distinct perturbations of the optical properties of the microcavity.

In the case of the weak exciton-photon regime, the spontaneous emission rate of the exciton is modified. According to Fermi's Golden Rule, the probability of a transition from an initial to a final state is proportional to the density of final states.[98] The density of photon states in a microcavity is highly altered (only certain modes exist) from the case of free space (Eqn. 2.16). As a consequence, the radiative lifetime of the exciton in a microcavity is determined by the spatial overlap of the exciton and the perturbed photon density of states.[98] This effect is quantified by the following expression for the rate of spontaneous emission in the cavity (Γ_{cav}) and in vacuum (Γ_0):[98]

$$\Gamma_{cav} \cong \Gamma_0 \frac{Q\lambda^3}{V} \tag{2.20}$$

The cavity quality factor (Eqn. 2.14), volume of the cavity, and wavelength of interest are denoted by, Q, V, and λ, respectively. Accordingly, the spontaneous emission rates as well as the angular properties of emission of a material are modified when embedded in a weakly coupled microcavity.[79-84,91,96,97,102-109]

The strongly coupled regime results in a condition where energy is periodically exchanged between the exciton and photon. This causes a splitting of the resonant modes of the system. The separation between these two frequencies at closest approach is a quantity known as the Rabi frequency and is a measure of the interaction strength between the exciton and the photon. The strong exciton-photon coupling regime is modeled in the following section.

2.3.2 Theory of Microcavity Polaritons

2.3.2.1 Classical Linear Dispersion Model

First, a classical linear dispersion model will be reviewed. The advantage of this model is that it can be derived from first principles. Starting with the dispersion for the cavity mode given in Eqn. 2.16, a substitution is made for the index of refraction. Working under the assumption that the relative permeability of most materials is close to one at optical frequencies, the index of refraction can be set equal to the square root of a background dielectric constant ε_b.[110] Subsequently, the cavity photon dispersion becomes:

$$E_{ph} = \frac{\hbar c}{\sqrt{\varepsilon_b}} \sqrt{k_\perp^2 + k_\parallel^2} \tag{2.21}$$

Assuming that the cavity medium has a single exciton resonance which is dispersionless and applying Maxwell's equations for a transverse wave yields:[110]

$$\frac{\hbar^2 c^2 \sqrt{k_\perp^2 + k_\parallel^2}}{E^2} = \varepsilon_b + \frac{A}{E_{ex}^2 - E^2 - 2iE\gamma_{ex}} \tag{2.22}$$

The far right term is equivalent to a Lorentzian lineshape function with the constant A containing information about the oscillator strength (equivalent to the strength of absorption) of the exciton.[110] Similar to above, γ_{ex} is the total broadening (linewidth) of the exciton resonance. If the cavity mode is tuned close to resonance with the exciton, it implies that $E \approx E_{ph} \approx E_{ex}$. Substituting Eqn. 2.21 into Eqn. 2.22 and rearranging gives:

$$\frac{A}{E_{ex}^2 - E^2 - 2iE\gamma_{ex}} = \frac{\varepsilon_b E_{ph}^2}{E^2} - \varepsilon_b = \frac{\varepsilon_b\left(E_{ph}^2 - E^2\right)}{E^2} \tag{2.23}$$

but

$$E_{ph}^2 - E^2 = \left(E_{ph} + E\right)\left(E_{ph} - E\right) \approx 2E\left(E_{ph} - E\right) \tag{2.24}$$

and

$$E_{ph}^2 - E^2 = 2E(E_{ex} - E) \tag{2.25}$$

Substituting Eqns. 2.24 and 2.25 into Eqn. 2.23 gives:

$$\left(E - E_{ph}\right)(E - E_{ex} + i\gamma_{ex}) = \frac{A}{4\varepsilon_b} \tag{2.26}$$

Setting $V^2 = \frac{A}{4\varepsilon_b}$, where V is the interaction term and substituting a linewidth (γ_{ph}) for the cavity photon into Eqn. 2.26 results in the following equation:

$$\left(E - E_{ph} + i\gamma_{ph}\right)(E - E_{ex} + i\gamma_{ex}) = V^2 \tag{2.27}$$

Solving for the energy eigenvalues (E) of the system gives:

$$E = \frac{E_{ph} + E_{ex} - i\left(\gamma_{ph} + \gamma_{ex}\right)}{2} \pm \frac{1}{2}\sqrt{\left(E_{ph} - E_{ex} - i\left(\gamma_{ph} - \gamma_{ex}\right)\right)^2 + 4V^2} \tag{2.28}$$

Equation 2.28 exhibits the frequency splitting (in this case energy) discussed in the context of the strong exciton-photon regime. Fig. 2.5 is a plot of Eqn. 2.28 using Eqn. 2.16 as the cavity photon energy. The result is referred to as the polariton dispersion and is the classic signature of strong exciton-photon coupling.[76] For the lower polariton branch (thick black curve in Fig. 2.5), the polariton is photon-like at small angle and exciton-like at large angles of incidence. The upper polariton branch is exciton-like at small angle and photon-like at large angles of incidence. The polariton linewidths are weighted averages of the exciton and photon linewidths based on the polariton character (α^2 and β^2).[110] Figure 2.5 depicts an ideal case of constant linewidths over each branch.

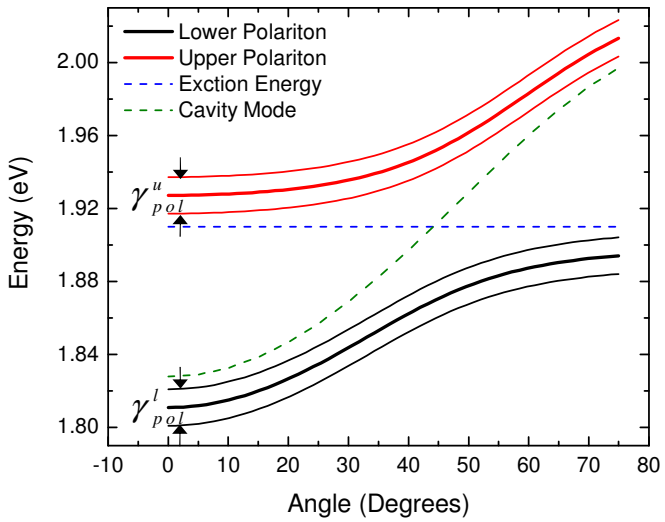

Figure 2.5 Equation 2.28 plotted with polariton linewidths. Uncoupled dispersions of the cavity photon and exciton are displayed as broken lines where the photon dispersion is given by Eqn. 2.16 and the exciton dispersion is flat (dispersionless). Polariton linewidths for the lower (γ_{pol}^{l}) and upper branch (γ_{pol}^{u}) are shown as fine lines above and below the two polariton branches.

2.3.2.2 *Quantum Mechanical Model*

The quantum mechanical model is the most powerful mathematical construct to explain microcavity polariton physics. Beyond the simplest form of the model presented here, additional terms can be included to account for polariton dynamics.[102,111-116] To start, the systems Hamiltonian (*H*) can be written in terms of the creation (designated by a superscript "+") and annihilation (designated by a superscript "-") operators (both bosonic operators) for the cavity photon (a_k^+, a_k^-) and exciton (b_k^+, b_k^-):[98,117]

$$H = \sum_k \hbar\omega_{ph}(k) a_k^+ a_k^- + \hbar\omega_{ex}(k) b_k^+ b_k^- - \sum_k \hbar\Gamma_{12}(a_k^+ b_k^- + b_k^+ a_k^-) \quad (2.29)$$

The interaction between the cavity photon and exciton is denoted by Γ_{12}. The Hamiltonian is the summation of the energies of creating a photon (1st term), exciton (2nd term) and polariton (3rd term) over all of the relevant wavevectors (*k*). New boson operators, ξ_p^- and ξ_p^+ are introduced to diagonalize the Hamiltonian such that:[118]

$$a_k^- = \sum_p \alpha_p(k) \xi_p^-(k) \quad (2.30)$$

$$b_k^- = \sum_p \beta_p(k) \xi_p^-(k) \quad (2.31)$$

Equations 2.30 and 2.31 can also be written in terms of the creation operators for the photon (a_k^+) and exciton (b_k^+) by adding the superscript "+" to ξ_p. The relative photon and exciton components of the polariton are denoted by α_p and β_p, respectively. Substitution of Eqns. 2.30 and 2.31 into 2.29 along with proper treatment of the boson operators yields the following expressions from the Hamiltonian eigenvalue problem:[118]

$$\alpha\left(\hbar\omega_{ph} - \hbar\omega\right) + \beta\hbar\Gamma_{12} = 0 \quad (2.32)$$

$$\alpha\hbar\Gamma_{12} + \beta(\hbar\omega_{ex} - \hbar\omega) = 0 \quad (2.33)$$

Upon evaluation of Eqns. 2.32 and 2.33, it is clear that the system of equations resembles an eigenvector and eigenvalue formulism. In fact, substituting the energies for the cavity photon (E_{ph}), exciton (E_{ex}), interaction term (V) and eigenvalue (E) for $\hbar\omega_{ph}$, $\hbar\omega_{ex}$, $\hbar\Gamma_{12}$ and $\hbar\omega$ yields:

$$\begin{bmatrix} E_{ph} & V \\ V & E_{ex} \end{bmatrix} \begin{bmatrix} \alpha \\ \beta \end{bmatrix} = E \begin{bmatrix} \alpha \\ \beta \end{bmatrix} \tag{2.34}$$

where $\begin{bmatrix} \alpha \\ \beta \end{bmatrix}$ is the eigenvector, E are the energy eigenvalues of the system. Equation 2.34 is often referred to as the coupled oscillator model.[99] The cavity photon and exciton are represented as harmonic oscillators with energies E_{ph} (Eqn. 2.16) and E_{ex}, respectively.[98,99] The off diagonal matrix element V denotes the coupling interaction between the exciton and cavity photon. Since a polariton is a quasiparticle of both exciton and photon character, $|\alpha|^2$ and $|\beta|^2$ represent the relative contributions of photon and exciton to the polariton, respectively.

The energetic broadenings (linewidths) of the cavity photon (γ_{ph}) and uncoupled exciton transition (γ_{ex}) can be included in Eqn. 2.34 as follows:

$$\begin{bmatrix} E_{ph} - i\gamma_{ph} & V \\ V & E_{ex} - i\gamma_{ex} \end{bmatrix} \begin{bmatrix} \alpha \\ \beta \end{bmatrix} = E \begin{bmatrix} \alpha \\ \beta \end{bmatrix} \tag{2.35}$$

Equation 2.35 leads to the exact same result obtained above in Eqn. 2.28. As is the case with many quantum mechanical problems, including additional terms in Eqn. 2.29 to account for supplemental physics increases the complexity of the solution, often requiring numerical methods to solve.[119] Nevertheless, the quantum mechanical model is a powerful construct to deal with most of the potential physics exhibited by strongly coupled systems.

2.3.3 Interpretation of Theory

The linewidths (broadening terms) play an important role in determining whether a system is strongly coupled. Concentrating on the case when the exciton and cavity photon are at resonance ($E_{ph} = E_{ex}$), Eqn. 2.28 simplifies to:

$$E = \frac{2E_{ex} - i(\gamma_{ex} + \gamma_{ph})}{2} \pm \frac{1}{2}\sqrt{4V^2 - (\gamma_{ex} - \gamma_{ph})^2} \tag{2.36}$$

Noticeably, there are two regimes based on the contribution from the square root.[102] In the case where $2V < |\gamma_{ex} - \gamma_{ph}|$, the value from the square root is solely imaginary, meaning that the exciton transition linewidth is modified. This leads to a modified angular emission pattern and decay rate, which is characteristic of the weakly coupled regime. In contrast, the value under the square root is real when $2V > |\gamma_{ex} - \gamma_{ph}|$, leading to the strongly coupled regime and the appearance of two **new** energy features separated by a value known as the vacuum Rabi splitting (ħΩ), given by the following:[102]

$$\hbar\Omega = \hbar\sqrt{4V^2 - (\gamma_{ex} - \gamma_{ph})^2} \tag{2.37}$$

The concepts above are enormously important. The crossover between the weak and strong exciton-photon regime is entirely based on the broadening of the exciton resonance.[102] This is a material dependent property which can be determined by evaluating the linewidth of the feature of interest in an absorption spectrum. The cavity photon typically has a narrow linewidth (given by Eqn. 2.12), which implies that the width of the excitonic transition must be relatively narrow to realize strong exciton-photon. Unfortunately, this constricts the set of materials that are suitable for strong

exciton-photon coupling. The exciton broadening however is not the only material dependent property that is significant.

Using a semiclassical transfer matrix (TM) approach outlined in Ref [102,120], the interaction matrix term (V) can be derived. Deferring the TM treatment to Appendix B, Ref [102] presents the following result:

$$V = \sqrt{\frac{1+\sqrt{R}}{\sqrt{R}} \frac{c\Gamma_{ex}}{nL}} \tag{2.38}$$

where R is the reflectivity of the mirrors, n is the index of refraction of the cavity material, L is the mirror spacing, c is the speed of light and Γ_{ex} is the decay rate of the exciton. Qualitatively, it makes sense that the splitting is inversely proportional to an expression similar to the finesse of the cavity (damping process for cavity photons) and directly proportional to the decay rate (exciton damping process) of the exciton. The decay rate of an exciton in a cavity can be calculated using Fermi's Golden Rule.[121] In Ref. 121 it is found to be proportional to the oscillator strength of the exciton. The exciton oscillator strength is a parameter which expresses the strength of an excitonic transition.[98] As such, the experimental analog to the oscillator strength (*f*) is the absorption coefficient (α):[98]

$$f \propto \int \alpha(\omega)\, \partial\omega \tag{2.39}$$

Thus, the magnitude of absorption coefficient of a particular excitonic transition is a critical material characteristic to realize the strong exciton-photon regime.

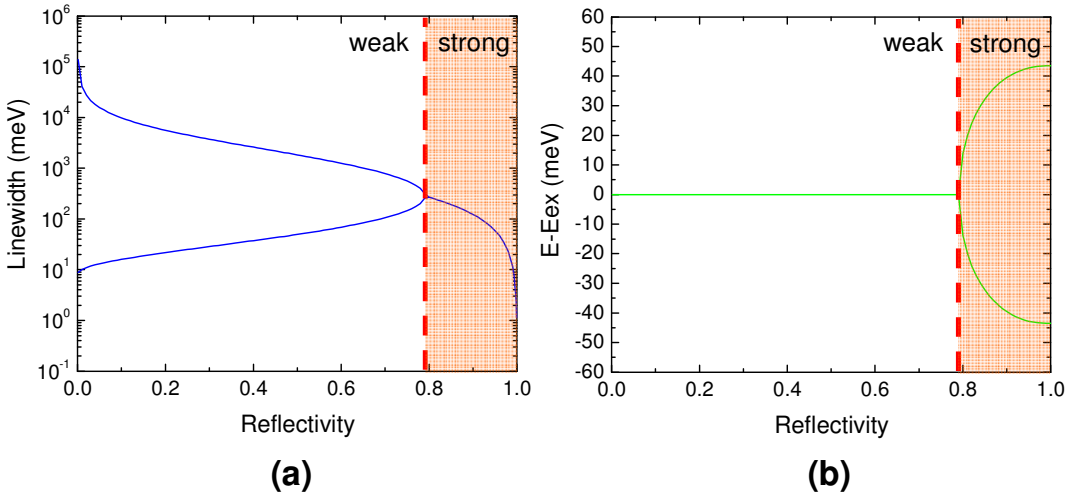

Figure 2.6 Plots of linewidth (a) and energy (b) versus reflectivity (see Eqn. 2.36). Linewidth splitting is characteristic of the weak coupling regime (not-highlighted) whereas the energy splitting is characteristic of the strong coupling regime (highlighted). Equations 2.36 and 2.38 were used to generate the plots and calculated with values typical of an organic microcavity.

In conclusion, two material properties are important when attempting to access the regime of strong exciton-photon. These properties are the exciton oscillator strength and the linewidth of the exciton. If both properties are sufficient to realize the strong exciton-photon regime, the only remaining quantity of significance is the cavity finesse, which is mainly dependent upon the choice of the cavity reflectors. Equation 2.38 substituted in Eqn. 2.36 demonstrates the dependence of the coupling regime upon reflectivity. When the mirror reflectivity is small such that the linewidth mismatch term (γ_{ex}-γ_{ph}) is larger than Eqn. 2.36, the splitting is purely imaginary and hence only observed in the linewidth (Fig. 2.6a).[102] This is the signature of the weak exciton-photon coupling regime and is manifested experimentally as a modification of the exciton decay rate. Eventually, a crossover exists between strong and weak exciton-photon coupling where the reflectivity becomes large enough that the interaction term V is larger than the

linewidth mismatch term ($\gamma_{ex} - \gamma_{ph}$).[102] In this case, two distinct energy features are present signifying strong exciton-photon coupling (Fig. 2.6b). Figure 2.6 exemplifies the two regimes with the following assumptions: the exciton has a constant linewidth with respect to reflectivity and the linewidth of the photon varies with reflectivity as in Eqn. 2.12 (with no angular dependence). Knowing the characteristic experimental signatures of the strong and weak exciton-photon coupling regimes is essential when interpreting data.

2.3.4 Probing Microcavity Polaritons Experimentally

The theoretical treatment discussed in Sec. 2.3.3 gives insight into what to expect experimentally in a strongly or weakly coupled system. The energy splitting observed in the regime of strong exciton-photon coupling is the formation of two new energetic states termed the upper and lower branch polariton. One of the two states is higher (upper polariton) in energy than the exciton while the other is lower (lower polariton) in energy. Figure 2.7a shows the modified excitonic energy level diagram (Jablonski diagram as discussed in Sec. 1.3.2) at strongest coupling if the cavity photon is coupling with the lowest energy exciton (S_1).[122] If the strong exciton-photon regime is realized, polaritons are allowed energy states that can be populated by a variety of techniques and hence detected by various approaches.

Evidence for the existence of polaritons can be observed in the following experiments: reflectivity, transmission, absorption, photoluminescence (PL) and electroluminescence (EL).[123-127] Before proceeding, the experimental techniques listed above can be divided into two basic categories which have noticeably different physics. Reflectivity, absorption and transmission are all techniques that involve directly populating energetic levels of the system to detect changes in the absorptive behavior of the system without regard for relaxation dynamics (Fig. 2.7a).

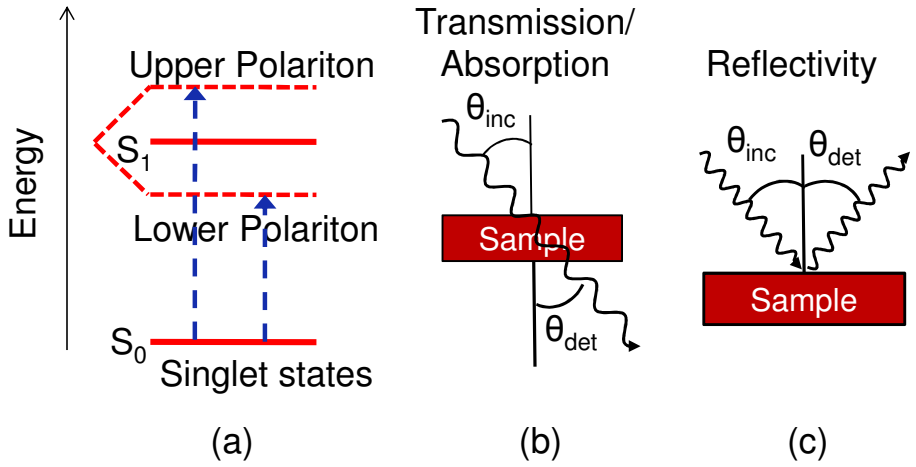

Figure 2.7 (a) Modified excitonic energy level diagram as a result of strong exciton-photon. Transmission/absorption (b) and reflectivity measurements (c) result in direct excitation of polariton states. The angle of incidence and angle of detection are denoted by θ_{inc} and θ_{det}, respectively.

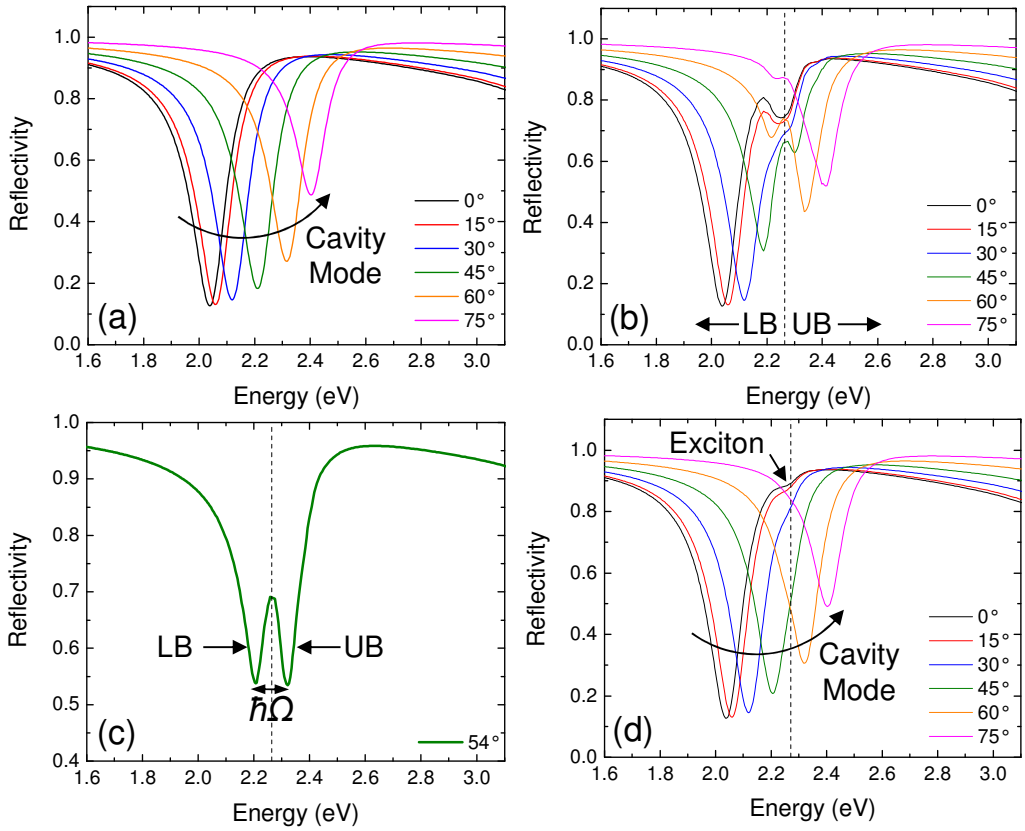

Figure 2.8 Transfer matrix simulation (Appendix B) of an organic microcavity consisting of a 130 nm organic semiconductor (n=1.8, k=0) slab sandwiched between two 27.5 nm thick metal reflectors. (a) Reflectivity spectra of the cavity mode which "walks" to higher energy as angle of incidence is increased. (b) Reflectivity spectra of a microcavity containing an organic semiconductor with a single absorbing feature (k≠0) at ~2.25 eV. Two spectral features designated by LB (lower branch polariton) and UB (upper branch polariton) increase in energy with increasing angle of incidence which is characteristic of the strong exciton-photon regime. (c) Strong exciton-photon at resonance. Two equal intensity dips corresponding to the lower branch polariton (LB) and the upper branch polariton (UB) are observed and are energetically separated by the Rabi splitting ($\hbar\Omega$). (d) Reflectivity spectra portraying the weak coupling regime. The exciton feature is "absorbed" into the cavity mode. In (b)-(d) the dotted line denotes the excitonic transition (~2.25 eV) of interest.

For these experiments, the cavity mode is typically tuned angularly toward resonance with the exciton energy (can also tuned by changing cavity thickness, see Eqn. 2.8), by adjusting the angle of incidence.[123] As the angle is increased, the cavity mode energy increases (Eqn. 2.16). Incident light is stored in the resonator as the cavity mode and hence appears as a peak in transmission/absorption (Fig. 2.7b) and a dip in

reflectivity (Fig. 2.7c).[66] A simulation of the cavity mode of an optical microcavity under white light reflectivity is shown in Fig. 2.9a.

Building off of the example in Fig. 2.8a, an absorbing (active) cavity material would result in exciton formation. This would again appear as a dip in reflectivity because optical energy is absorbed for exciton creation. The exciton has no angular dispersion (dispersionless) and hence does not change energy as the angle of incidence is increased.[102] However, the high energy peak (designated by a UB) will show marked dispersion and increase in energy if the strong exciton-photon regime is realized.[123] In this case, the new eigenstates of the system are lower (LB in Fig. 2.8b) and upper branch (UB in Fig. 2.8b) polaritons which exhibit dispersion with angle of incidence since they contain cavity photon character. Looking closely at the reflectivity spectra, two important trends are demonstrated. First, the lower polariton feature is very similar in appearance and dispersion to a cavity mode at low angle but asymptotes towards the exciton absorption energy at high angle (Fig. 2.8b). Alternatively, the upper polariton feature begins slowly increasing in energy from the exciton absorption energy at low angles but approaches the cavity photon at high angle (Fig. 2.8b). Tracking the two features by recording the energy of the centers of the dips at each angle of incidence yields a polariton dispersion shown in Fig. 2.9.[76] Characteristically, the lower (upper) branch asymptotes to the cavity mode at low angle (high angle) and exciton at high angle (low angle).

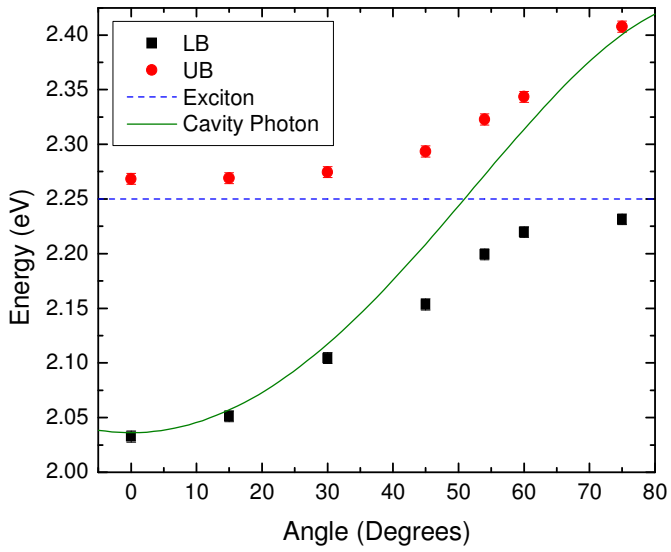

Figure 2.9 Dispersion relation of the lower (LB) and upper branch (UB) of the simulated angle-resolved reflectivity spectra of Fig. 2.8b. The cavity mode (solid line) was extracted from the reflectivity spectra of Fig. 2.8a. The excitonic transition of interest denoted by a broken line.

A special case exists when the cavity photon energy is tuned to that of the exciton. This condition is referred to as the point of strongest coupling or point of anti-crossing and is also the angle of incidence at which the upper polariton and lower polariton are separated in energy by the Rabi energy.[76] Anti-crossing is manifested in reflectivity, transmission, and absorption as two equal intensity (depth of the dips in reflectivity) features as shown in Fig. 2.8c.[128] The relative depth of each polariton feature in the reflectivity spectra is related to the character (weight photon and exciton) of the branch. At angles below resonance, lower branch states are mostly photon-like, and thus have deeper reflectivity responses. At angles above resonance, the lower branch is more exciton-like and hence exhibits a shallower reflectivity response. The opposite is true for

the upper branch as the reflectivity response increases with angle of incidence. At resonance, the relative character of both branches is 50% photon and 50% exciton. The character of the lower and upper branch polaritons (calculated using Eqn. 2.34 and the dispersion of Fig. 2.9) of Fig. 2.8b are shown in Fig. 2.10.

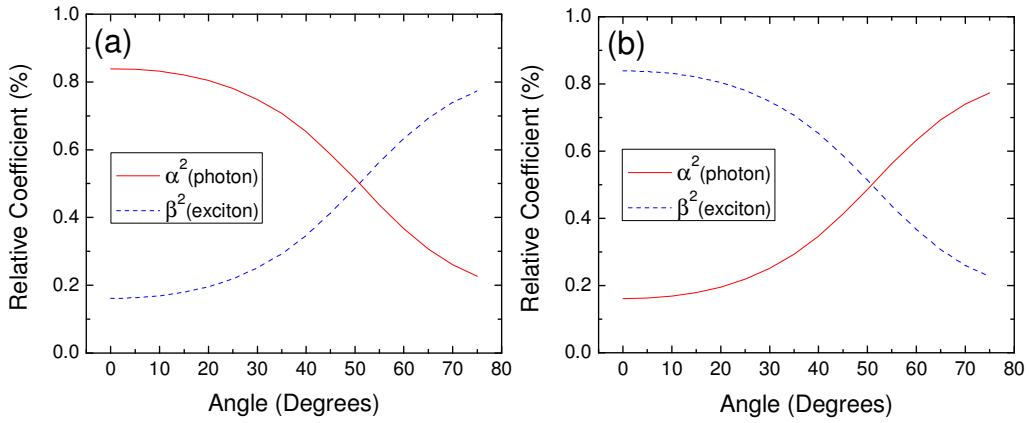

Figure 2.10 Character versus angle of incidence for the lower (a) and upper (b) polariton branches of Fig. 2.8b calculated from the dispersion of Fig. 2.9. The resonance condition is observed around 54°, where the polariton is half exciton and cavity photon for both branches.

If the exciton oscillator strength is reduced, a crossover exists from strong to weak exciton-photon coupling.[102] Weak exciton-photon coupling manifests itself in reflectivity, transmission and absorption as a modification in the cavity mode linewidth and intensity but not as an energetic splitting. The excitonic feature in Fig. 2.8d is "absorbed" by the cavity mode as the cavity mode increases in energy with angle of incidence, but has no dispersion of its own. Also, in Fig. 2.8d it is observed that the cavity mode is the only feature present near resonance (magenta spectrum) and that it differs in linewidth and intensity from the "empty" cavity mode (Fig. 2.8a). This is the so-called weak exciton-photon coupling regime.

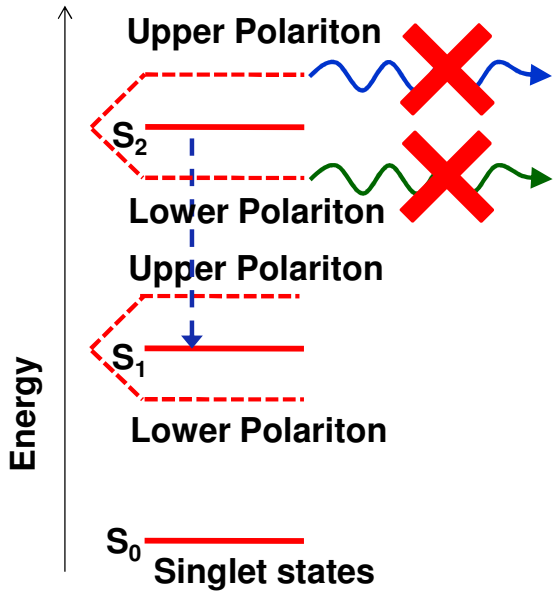

Figure 2.11 In measurements of PL and EL, excited state dynamics must be taken into consideration when analyzing the results of an experiment. In this system, strong coupling occurs between the cavity photon and the S_2 excitonic transition. However, no polariton emission is observed due to rapid relaxation of the S_2 excitonic state to S_1.

Photoluminescence and EL are methods that entail populating energetic states and measuring the emission from those states. In doing so, the excited state dynamics of the material are introduced and non-radiative recombination, intersystem crossing, or polariton relaxation, and hence their respective lifetimes must be considered.[124] For example, consider a system where the cavity photon is strongly coupled to an S_2 excitonic transition (Fig. 2.11). Rapid vibronic relaxation of S_2 to S_1 excitonic energy states makes observing polariton PL and EL difficult since these states are emptied non-radiatively prior to polariton emission.[122,129,130] Therefore, the excited state dynamics of the active coupling material and polariton states must be taken into consideration when analyzing the results of such an experiment (Fig. 2.12a). For these reasons, PL and EL are often more interesting and fruitful experiments, given the window in polariton dynamics.

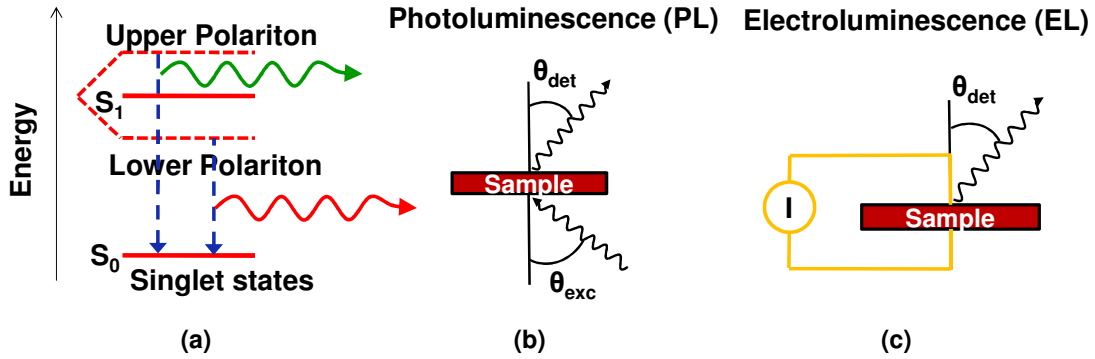

Figure 2.12 (a) Excitonic energy diagram of polariton PL and EL. Emission is observed from polariton states thus excited state dynamics must be considered. (b) Schematics of PL (b) and EL (c) experiments.

In PL, excitation is accomplished with a light source incident on the sample with the detection angle adjusted to tune the cavity mode (2.12b).[131] The largest absorption peak of the active coupling material is typically excited, allowing for maximum absorption. Often the transition of interest for coupling is much lower in energy than the largest absorption peak and internal conversion to the lowest energy exciton occurs prior to the formation of polariton states.[132] EL differs from PL in that the excitation is performed electrically by passing a current through the device and therefore only the detection angle needs to be considered (Fig. 2.12c).[127]

In both microcavity PL and EL experiments, emission from the active material in a weakly coupled system is "funneled" through the cavity photon mode due to the modified density of photon states of the microcavity.[79] In the strong exciton-photon regime, tuning the cavity photon towards the exciton energy yields a splitting in the emission pattern.[127,130,132,133] This should appear as two separate peaks in emission both exhibiting dispersion with angle as in Fig. 2.13, thus a polariton dispersion similar to Fig. 2.9 can in principle be extracted from the PL or EL spectra. As in reflectivity, absorption

and transmission, the upper and lower polariton features asymptote to the exciton and cavity photon energies analogously. In addition, the intensities of lower and upper branch emission should reflect the photon character of the branch of interest. Photon-like polariton states have a shorter radiative lifetime (the cavity photon typically has a much shorter lifetime (~10^{-12}-10^{-15} s) than the exciton) giving rise to efficient emission. As such, lower (upper) branch polariton luminescence is more (less) intense at low angles than high angles and should emit consistent with the photon character.[132]

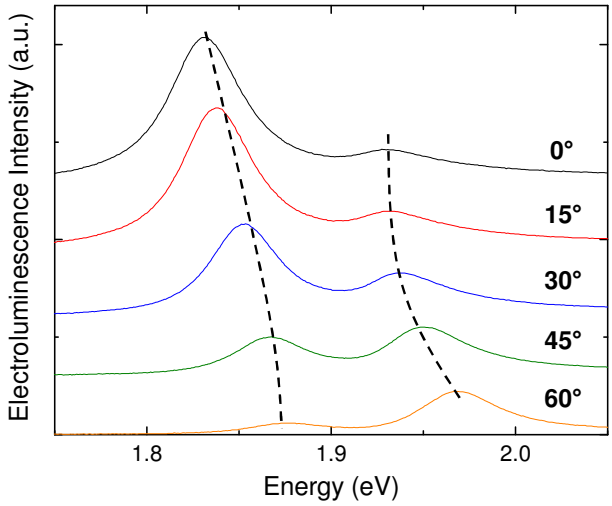

Figure 2.13 Angle-resolved polariton EL versus angle for a tetraphenylporphyrin microcavity (Chapter 3). Dotted lines are guides to the eye for the dispersions of the lower and upper branch.

As already noted, emission is a time dependent process permitting competing relaxation processes. As such, strongly coupled organic microcavities typically exhibit weak upper branch polariton emission because of efficient relaxation of upper branch polaritons via a variety of mechanisms.[111,112,124,127,130,132,134] This makes analyzing EL and PL results more challenging than reflectivity, transmission and absorption. Plotting a

dispersion (as shown in Fig. 2.9) and confirming the asymptotes is the only way to be certain that the observed emission is from a polariton state and not a weakly coupled exciton.[124]

Weak exciton-photon coupling in PL and EL modifies the emission pattern of the cavity material.[79-82,96-98,107,109,135] As discussed in Sec. 2.3.3, the linewidth of the emission in the weakly coupled regime is also modified (Fig. 2.14a). Non-cavity emission in a conventional OLED is typically Lambertian and consequently reduces in intensity as the detection angle is increased.[136] Conversely, microcavity emission follows the dispersion of the cavity mode as the angle is changed (see Fig. 2.14b). All of the experiments mentioned above are efficient probes in determining the coupling regime of a particular sample and are thus important experiments in the context of polaritons.

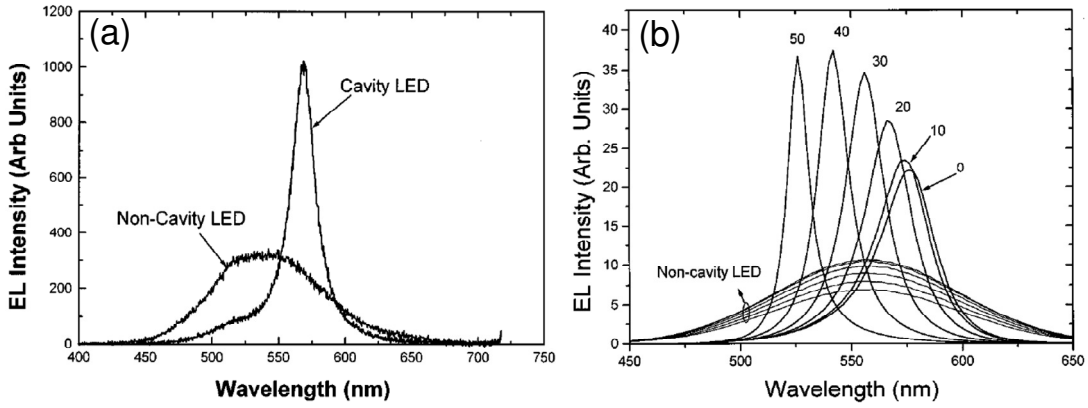

Figure 2.14 (a) Electroluminescence (EL) from a weakly coupled microcavity LED versus a non-cavity LED. (b) A comparison between the angle resolved EL from a non-cavity LED versus a weakly coupled microcavity LED.[79]

2.4 Scattering of Microcavity Polaritons

Scattering is a process by which polaritons relax in energy and in-plane momentum (angle of incidence). The possible energies and momentum of polariton

states are specified by the dispersion relation, thus, all polariton relaxation processes must occur along the dispersion relation. A mechanical analog can be made to a ball in a bowl. For the ball to relax to the bottom of the bowl it must roll along surface. Polariton scattering occurs through interactions with other particles or quanta of energy and momentum such as phonons, other polaritons, charge carriers, etc.[98,115,116,137,138] The scattering process is essential to the realization of optoelectronic devices based on polaritons such as optical amplifiers and lasers.[115,137-159] Historically, these demonstrations have been restricted to inorganic semiconductor systems.[98,137] Recently, however, lasing was demonstrated in a single crystal organic microcavity.[71] This section will explain the physics behind polariton optical amplifiers and lasers.

2.4.1 Polariton Lasing

A polariton laser is actually a coherent (meaning in-phase) emitter.[156] This distinction is made because no population inversion is required to realize a polariton laser. Coherent emission, rather, occurs due to a large build-up of polaritons in a single state referred to as a macroscopic population.[137] A macroscopic population of polariton states is obtained through a process called stimulated scattering which relies on various unique properties of polaritons.[98]

Using Eqn. 2.18, angle of incidence can be converted into in-plane wavevector ($k_{\parallel}$), yielding a dispersion where the possible energies and momenta of polaritons are clearly defined (see Fig. 2.15). By adjusting the cavity detuning ($\Delta = E_{ph} - E_{ex}$), defined as the energy separation between the exciton and cavity photon at $k_{\parallel}=0$ (see Fig. 2.15), the energetic minimum and shape of the polariton branch can be manipulated. The lower

branch has a shape analogous to a potential well suggesting that polaritons could potentially relax to the energetic minimum of the well (Fig. 2.15). Additionally, polaritons are bosons, as they are an admixture of two bosonic particles.[137] This means that polaritons do not obey the Pauli Exclusion Principle and thus a macroscopic population of polaritons can exist in a single state. Combining the aforementioned properties of polaritons, it could be possible to condense all of the polaritons on the lower branch and build up a macroscopic population at the energy minimum ($k_{\parallel}=0$).[137]

If the polariton population exceeds unity at $k_{\parallel}=0$, then stimulated scattering occurs, where transitions can be stimulated by population of the final state.[156] Reverting back to the mechanical analogy (this is an analogy and does not represent the actual physics), assume that there are now three magnetic balls in the bowl, where one ball is already at the bottom of the bowl (the $k_{\parallel}=0$ state). The ball in the bottom of the bowl will pull the other two balls to the final state. Stimulated scattering of polaritons is an analogous process however it is a bosonic interaction rather than a magnetic interaction. In the case of stimulated scattering, the rate of transition to the final state is proportional to $(1 + N_{final})$, where N_{final} is the final state population. Thus, the larger the population is at $k_{\parallel}=0$, the stronger the interaction is. The combination of the above properties has led to the concept of a polariton laser, where a macroscopic population of polaritons is accumulated at $k_{\parallel}=0$ (could be energy tuned by adjusting detuning) by means of stimulated scattering.[137] In general, two methods have been employed to realize stimulated scattering: resonant and non-resonant pumping.

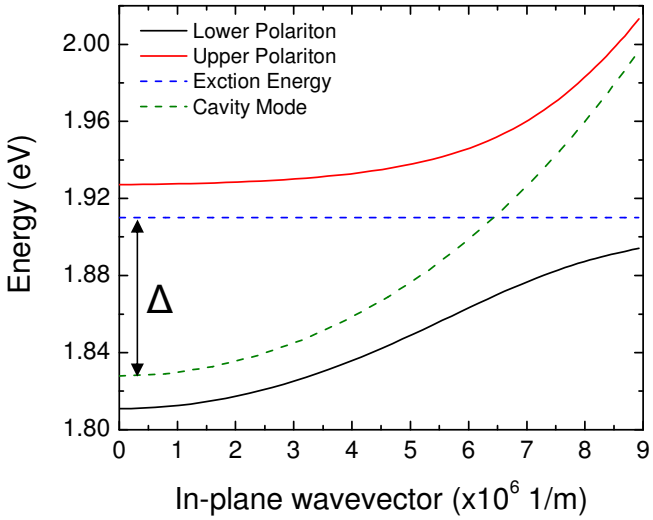

Figure 2.15 Polariton dispersion relation of energy vs. wavevector for a microcavity polariton where Δ denotes the detuning and is given by $\Delta = E_{ph} - E_{ex}$.

2.4.2 Resonant Pumping

Resonant pumping (resonant to the dispersion) refers to a technique by which polaritons are created at a distinct energy and in-plane wavevector (angle of incidence) on the lower branch.[137] In this case, all created polaritons have the same phase due to the coherent pump source. The resonant pumping technique results in polariton-polariton scattering (parametric scattering) in which momentum and energy are conserved.[156] The momentum and energy conservation can be written as:

$$2k_R = k_0 + k_L$$

$$2E_R = E_0 + E_L$$

The subscripts R, 0 and L denote the pump, zero wavevector polariton and large wavevector polariton, respectively. The position at which the conservation laws are satisfied is often referred to as the magic angle or matching angle (θ_{match}).[156] Figure 2.16 demonstrates resonant pumping and the resulting polariton-polariton scattering. The population of $k_{\|}$=0 can be probed via transmission or reflection to gauge the change in population.

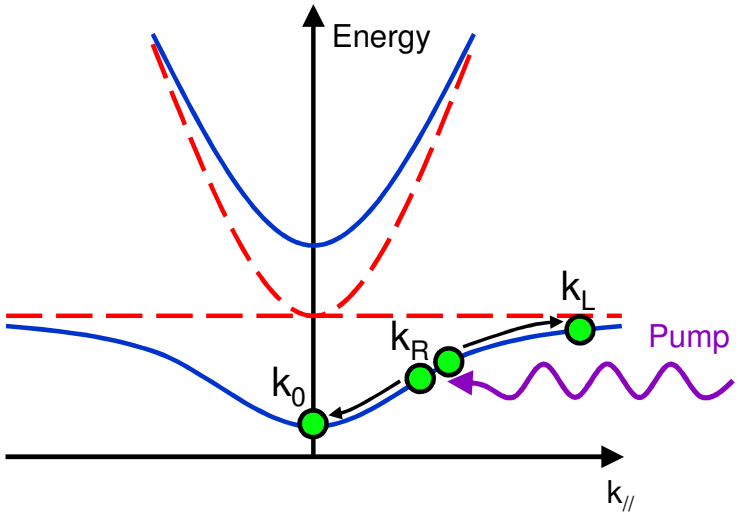

Figure 2.16 Resonant pumping and parametric scattering. Polaritons are created directly in the lower polariton branch. Pair-wise scattering results in polariton occupation of $k_{\|}$=0 and a higher energy and momentum polariton.

Stevenson et al. showed that parametric scattering is possible in an inorganic ($In_{0.06}Ga_{0.94}As$) microcavity under resonant excitation (Fig. 2.17).[153] At sufficient pump powers ($P=1.15\times10^3$ Wcm^{-2}) stimulated scattering is manifested in an inherent increase in the emission intensity at $k_{\|}$=0 (0°) (Fig. 2.17a). A macroscopic polariton population is then established at larger pump powers ($P=1.9\times10^3$ Wcm^{-2} and $P=2.3\times10^3$ Wcm^{-2}) and narrow, amplified emission is observed from $k_{\|}$=0 (0°) (Fig. 2.15a).[156] At the largest

pump power (P=2.3x10^3 Wcm^{-2}), significant emission is seen from the $k_{\|}$=0 polariton state but little emission is seen from the momentum and energy conserving polariton state. This is attributed to the polariton at high angle being predominantly exciton-like resulting in a longer lifetime than the photon-like polariton at $k_{\|}$=0. Parametric scattering has been shown in a variety of inorganic microcavities.[147,160]

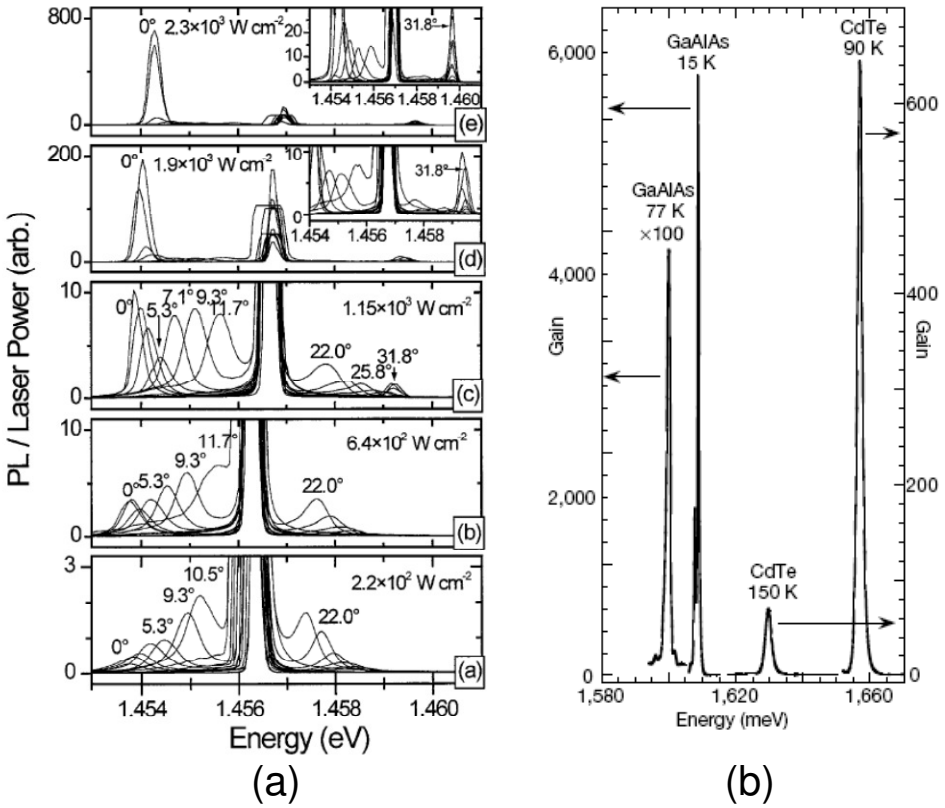

Figure 2.17 (a) Resonant excitation of a strongly coupled $In_{0.06}Ga_{0.94}As$ microcavity. The angle-resolved PL is monitored as a function of angle of incidence and pump power. As the pump power is increased, a large re-distribution of emission is observed as a result of parametric scattering. At the largest pump power (P=2.3x10^3 Wcm^{-2}), intense emission at 0° signifying a macroscopic population.[156] (b) Ultrafast pump-probe spectroscopy results for a variety of inorganic microcavities. The probe creates a population of polaritons at $k_{\|}$=0. If the pump is tuned to the magic angle, large amplification (gain) of the probe pulse is observed as a result of parametric scattering.[153]

Stimulated scattering has also been shown in ultrafast pump-probe experiments (Fig. 2.17b).[153,155] In these experiments, a low power probe laser is used to create a population at $k_{\parallel}=0$ to encourage stimulated scattering.[153,155] Without the probe pulse, no scattering is observed because the ultrafast pump does not allow for a sufficiently large build-up of polariton states at $k_{\parallel}=0$ to initiate stimulated scattering.[153] The probe pulse is amplified and thus exhibits gain when present, but only when the pump beam is at the magic angle.[153] Increasing temperature results in an marked decrease in gain and increase in width of the probe pulse due to the dephasing of the exciton by increased phonon-exciton collisions. Increasing the temperature causes a red shift in the semiconductor bandgap resulting in a shift of the probe gain toward higher energy (see Fig. 2.17b).[153]

2.4.3 Non-resonant Pumping

The distinction of non-resonant pumping from resonant pumping is that excitons are created with the intention that they energetically relax into lower branch polariton states through phonon emission (Fig. 2.18).[137] High energy excitons are created, which relax via longitudinal optical phonon emission to form a reservoir of large k excitons.[157] Additional relaxation from the exciton reservoir by emission of one to multiple acoustic phonons creates polariton states in the lower branch.[137] The emission intensity at various angles detection gives information about the magnitude of scattering to each polariton state on the lower branch.

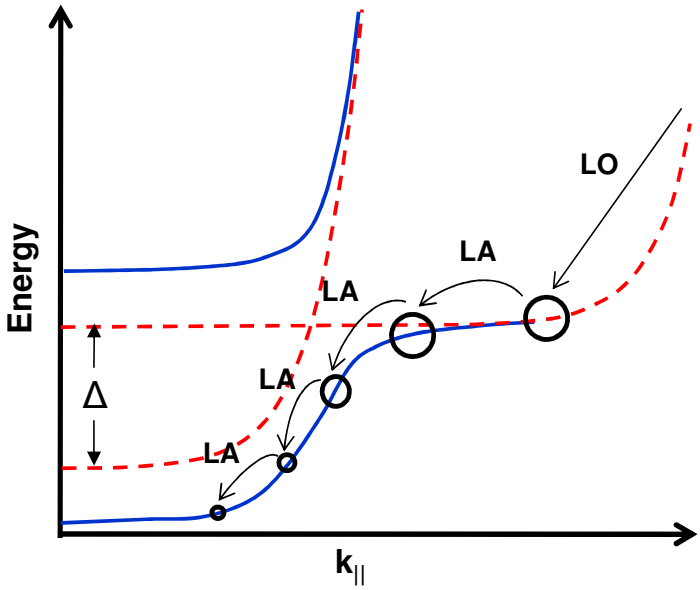

Figure 2.18 Schematic of non-resonant excitation and resulting phonon-assisted scattering mechanisms for inorganic systems. In organic systems, the exciton is dispersionless (flat) and the function of longitudinal acoustic (LA) phonons is replaced by intermolecular phonons.

As polaritons relax (coherently) down the lower branch, they become increasingly photon-like (see Fig. 2.10a) and their lifetime decreases (radiative rate increases).[157] This results in a competition between the relaxation by polariton-phonon scattering and polariton radiative decay, a phenomenon known as the relaxation bottleneck.[157] A consequence of the relaxation bottleneck is a depletion of low k polariton states relative to high k polariton states, represented in Fig. 2.18 by decreasing circle diameters.[157] The depletion occurs relative to the anti-crossing on the lower polariton branch.

As discussed above resonance is the point on the dispersion where the polariton in either branch is 50% photon and 50% exciton. States lower (higher) in energy than the anti-crossing are more photon-like (exciton-like) (Fig. 2.10a). Therefore, the relaxation bottleneck depends strongly on the detuning of the microcavity since the detuning

controls the anti-crossing position of the dispersion. In fact, Tartakovskii et al. see no bottleneck behavior for cavities with positive or zero detunings and a more dramatic bottleneck effect for larger negative detunings.[157] At positive and zero detunings, the entire lower branch is mostly exciton-like and the bottleneck is thus suppressed. While at negative detunings, a larger amount of polariton states are mostly photon-like and hence the bottleneck effect is more severe (Fig. 2.19, top panel).[157]

The relaxation bottleneck can also be suppressed with increased pump power (P=400 Wcm^{-2} and P=1200 Wcm^{-2}, Fig. 2.19).[157] At large enough pump powers, enough polaritons exist in the system that polariton-polariton scattering becomes significant and the bottleneck is suppressed.[137] This appears in the data, as enhanced emission from $k_{||}=0$ is observed as the pump power is increased (P=400 Wcm^{-2} and P=1200 Wcm^{-2} as opposed to the top panel, Fig. 2.19).[140] Although polariton-polariton scattering is achieved, parametric scattering (boson interaction) never occurs as the pump power is increased because of the large exciton density present in the semiconductor. The large exciton densities result in screening effects and hence broadening of the excitonic transition.[140] Eventually, the exciton broadening (linewidth or γ_{ex}) becomes larger than the interaction term (V) in Eqn. 2.37 and strong-coupling is lost (Fig. 2.6).[137] At even larger pump powers, exciton screening results in dissociation of the exciton and traditional lasing is observed at the band gap energy of the semiconductor (P= 3200 Wcm^{-2} Fig. 2.19).

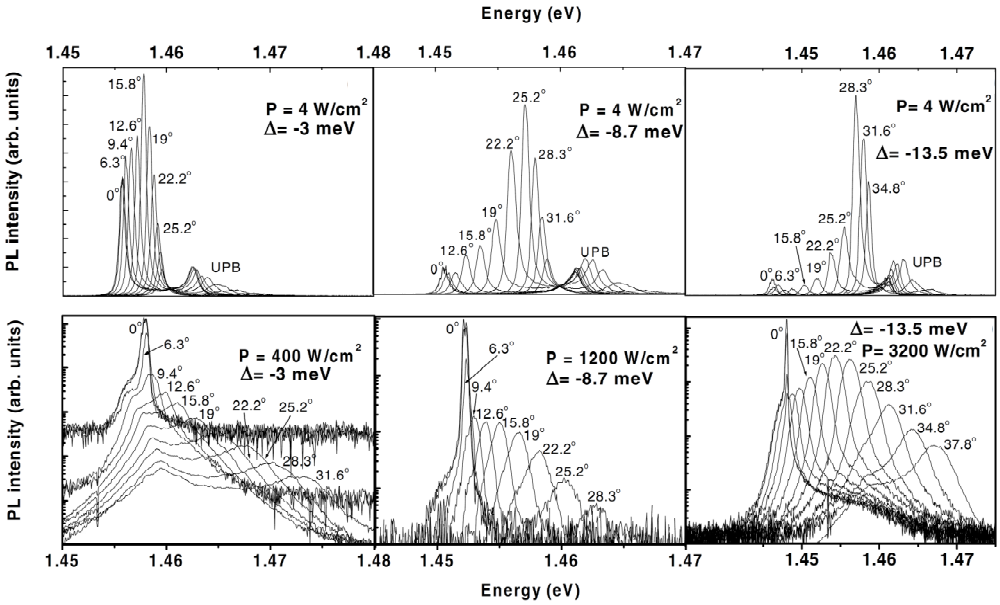

Figure 2.19 Angle resolved polariton emission at various pump powers (P) and detunings (Δ). The top panel demonstrates the effect of the detuning on the polariton bottleneck. The bottom panel illustrates the physics of non-resonantly pumped microcavities subjected to increasing pump power.[140]

2.4.3.1 Organic Polariton Lasing

In the previous sections, the concept of polariton lasing was introduced. Recently, the first demonstration of organic polariton lasing under optical excitation was published by Kéna-Cohen et al.[71] In this case, the mechanism responsible for the macroscopic polariton population at $k_{\parallel}=0$ is contrary to inorganic polariton lasers where polariton relaxation to the ground state occurs through stimulated scattering or a multistep relaxation along the lower branch. In the anthracene single crystal microcavity studied, fast relaxation of photogenerated excitons to the $k_{\parallel}=0$ state was achieved through direct radiative scattering. Direct radiative scattering occurs through the vibrationally assisted radiative decay of incoherent excitons which are populated by non-resonant

pumping.[71] The effectiveness of the radiative scattering process of reservoir excitons to the $k_{\parallel}=0$ state is manifested in the demonstration of a clear lasing threshold, spectral narrowing, and subsequent collapse of the emission lifetime as exhibited in Fig. 2.20. Although the mechanism responsible for polariton redistribution is different in this case, the demonstration of organic polariton lasing is an important first step to the realization of novel devices based on strongly coupled organic microcavities.

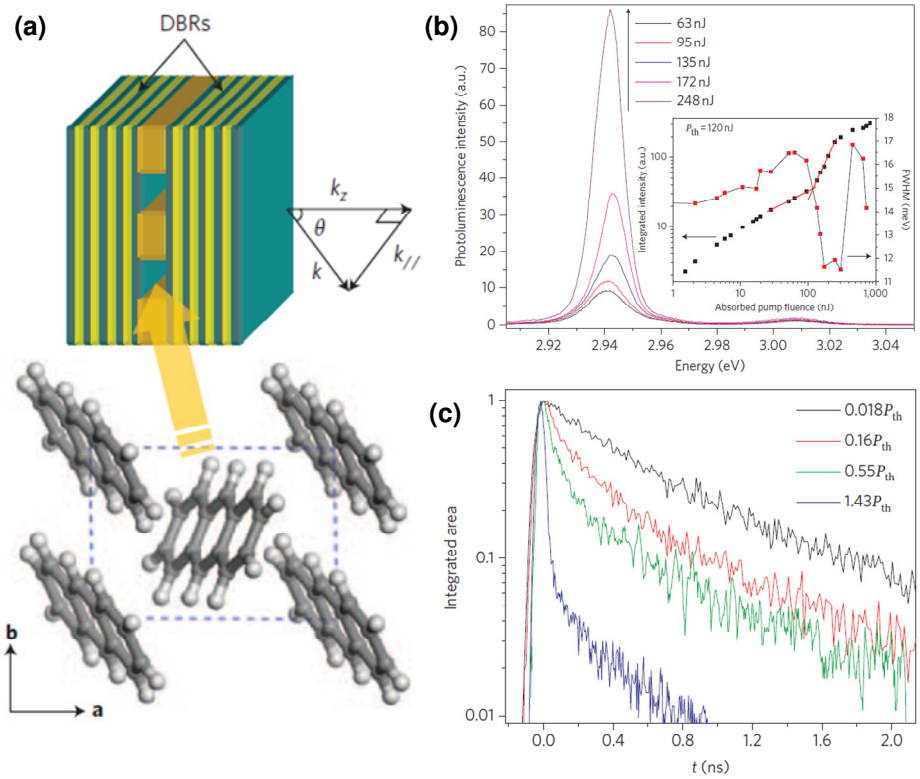

Figure 2.20 (a) The single crystal anthracene organic semiconductor microcavity architecture. (b) The photoluminescence intensity increases super linearly with pump power signaling the existence of lasing. Inset: The PL linewidth decreases with pump power and the intensity shows a clear change in slope. (c) The emission lifetime collapses with pump power, again, suggesting the lasing.[71]

2.4.4 Organic vs. Inorganic Semiconductor Microcavities

Organic microcavities have numerous attractive attributes for strongly coupled devices. As discussed in Sec. 1.3, inorganic semiconductor excitons are Wannier-Mott type and are thus weakly bound. The exciton is only stable at low temperature in these materials, making difficult the excitation of the polariton state at room temperature and under electrical excitation. Indeed, all of the scattering experiments discussed above were performed at temperatures much below room temperature.[137,140,156,157] There are a couple of exceptions such as GaN and GaAs microcavities which have shown the excitation of the polariton state (GaAs and GaN) and polariton lasing (GaN)[159] at room temperature.[141,142,159,161]

In contrast, organic semiconductor excited states are characterized as Frenkel or tightly bound excitons and are thus stable to thermalization at room temperature (Sec. 1.3). The ability to generate stable excitons has also permitted the realization of a stable strongly coupled state in these materials under large optical and electrical excitation densities, making organic semiconductors potentially more practical for device applications.[162] In addition to their large exciton binding energy, organic semiconductors also exhibit large exciton oscillator strengths, which ultimately increase the intensity of the interaction between the semiconductor and the cavity photon.[123] A strong light-matter interaction (Rabi splitting) allows for a larger tolerance of exciton broadening (linewidths) and more easily resolvable polariton features.[162]

2.5 Strong Exciton-Photon Coupling in Organic Microcavities

2.5.1 Common Materials

The number of organic semiconductors that exhibit strong exciton-photon coupling is limited by the two material criteria outlined in Sec. 2.3.3: exciton linewidth and oscillator strength. The material choices are therefore limited to organic semiconductors which demonstrate strong absorption with narrow linewidths. Unfortunately, this drastically condenses the list of suitable materials. Indeed, to date, only the following materials have been shown experimentally to exhibit strong exciton-photon: tetraphenylporphyrin (TPP), platinum(II) octaethylporphyrin (PtOEP), tetraphenylporphyrin zinc (ZnTPP), tetra-(2,6-t-butyl)phenylporphyrin zinc (4TBPPZn), various molecular J-aggregates, poly[*bis*(*p*-butylphenyl)silane] (PBPS), 3,4,7,8 napthalenetetracarboxylic dianhydride (NTCDA), anthracene, and tetracene.[124,127,130,133,163-167]

With the exception of TPP and PtOEP, the porphyrins listed above are solution processed in a polymer host. This can be a disadvantage for device fabrication as care must be taken to select materials and solvents that do not promote mixing of layers. In addition, these materials are typically doped in optically inactive, insulating polymer hosts making electrical excitation challenging.[123,163] An additional challenge is the ability to control film thickness when spin coating, which is needed to control the spectral position of the cavity mode. The porphyrins, TPP, ZnTPP, 4TBPPZn and PtOEP, (ZnTPP and 4TBPPZn can be thermally evaporated although they were solution

processed for the studies referenced above) and are instead materials that can be thermally evaporated, permitting fine thickness control and straightforward construction of multilayer devices.[63] Another potential challenge of all porphyrins is that they have many absorptive transitions, the strongest (largest oscillator strength) of which is non-radiative (see Fig. 2.21).[162] Coupling to this feature in emission is therefore difficult. However, the lowest energy absorption feature of TPP is radiative and has sufficient oscillator strength for strong exciton-photon.[130] Finally, PtOEP demonstrates intersystem crossing. Intersystem crossing is a disadvantage due to the competition with polariton states for excitons.[130]

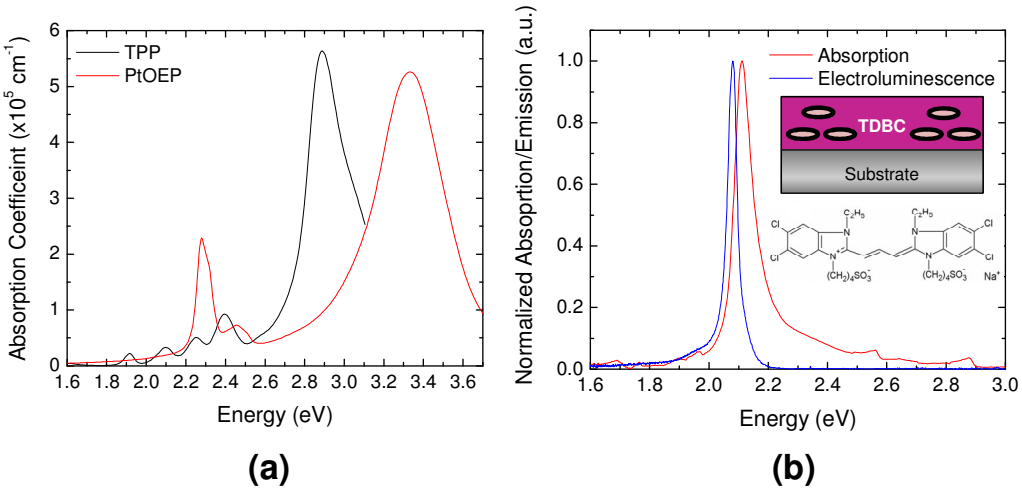

Figure 2.21 (a) Absorption coefficients of TPP and PtOEP. (b) Normalized emission and absorption for (5,6-dichloro-2-[3-[5,6-dichloro-1-ethyl-3-(3-sulfopropyl)-2(3H)-benzimidazolium hydroxide (TDBC), a molecular J-aggregate. Inset: An ordered alignment of dye molecules referred to as a J-aggregate and the molecular structure of TDBC.

Molecular J-aggregates are an attractive material class due to their giant exciton oscillator strengths, and single and narrow absorption and emission features under appropriate preparation conditions.[124,125,168-170] A single, narrow absorption feature is

achieved by forming an ordered alignment (referred to as a J-aggregate) of dye molecules (see Fig. 2.21). Molecular J-aggregates must be solution processed and often suspended in a polymer host matrix to achieve alignment.[124] Using a layer-by-layer deposition technique, Bradley et al. were able to overcome the need for a polymer host matrix while maintaining the most advantageous properties.[171] This development lead to the observation of polariton electroluminescence for the first time.[127]

NTCDA is also deposited by thermal evaporation much like TPP and PtOEP.[165] Slow growth rates have enabled the deposition of polycrystalline films of NTCDA with a relatively high exciton oscillator strength compared to the other materials.[165] Although such properties make NTCDA an encouraging active material, a major disadvantage is that NTCDA, due to its large bandgap, is difficult to excite electrically.[165] PBPS is the only pure polymer shown to exhibit strong exciton-photon in a microcavity. PBPS demonstrates giant splittings in high finesse cavities and clear polariton photoluminescence.[133] A disadvantage of PBPS is its broad exciton linewidth which would normally make it difficult to resolve strong exciton-photon but the giant Rabi splitting is able to overcome this problem.[133]

Crystalline organic semiconductors have also recently received significant attention as potential active materials in microcavities. The crystalline samples are fabricated by either slow rate thermal evaporation (tetracene) or a melt process (anthracene).[166,167] The high crystalline order of these materials enables high exciton oscillator strength and narrow absorption features. Figure 2.22 shows a selection of the active materials discussed above that have been used to observe strong exciton-photon coupling in organic semiconductors. Also shown are the relevant physical properties that make these materials interesting for the study of these phenomena.

	Peak Lambda (nm)	Alpha (cm^{-1})	Splitting (meV)	Cavity Structure
4TBPPZn	431	2.2×10^5	160	DBR/Metal
Tetracene	504	4.6×10^4	120	Metal/Metal
TDBC	595	1.0×10^6	265	Metal/Metal
PBPS	395	1.3×10^5	420	DBR/Metal
NTCDA	389	3.5×10^5	156	DBR/Metal

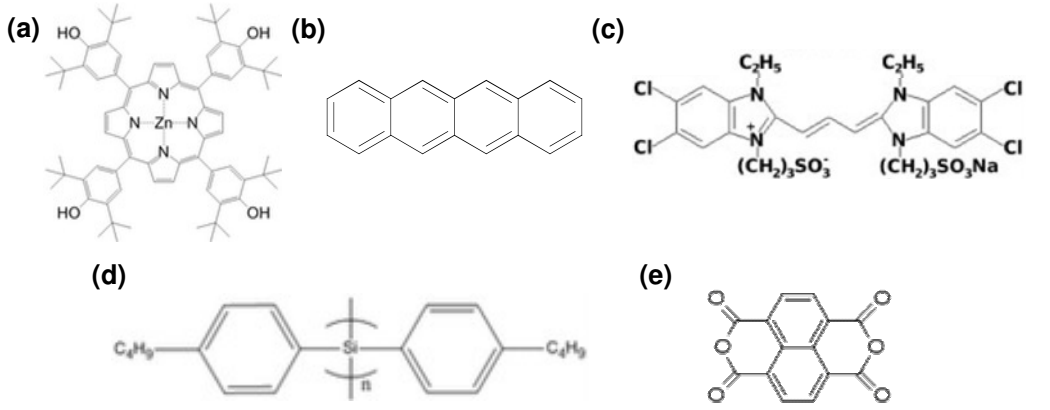

Figure 2.22 The above table gives an overview of the material specific properties for strong coupling materials. (a) Tetra-(2,6-t-butyl)phenylporphyrin zinc (4TBPPZn) (b) tetracene (c) (5,6-dichloro-2-[3-[5,6-dichloro-1-ethyl-3-(3-sulfopropyl)-2(3H)-benzimidazolidene]-1-propenyl]-1-ethyl-3-(3-sulfopropyl) benzimidazolium hydroxide (a J-Aggregate dye) (d) poly[bis(p-butylphenyl)silane] (PBPS) (e) 3,4,7,8 napthalenetetracarboxylic dianhydride (NTCDA)

2.5.2 Cavity Design

As noted in Sec. 2.3.3, the regime of strong exciton-photon coupling is realized when both the confined cavity photon and exciton decay rates are slower than the Rabi frequency. The decay rate of the cavity photon, or photon lifetime, can be engineered based on the design of the optical microcavity. The higher the Q of the optical cavity, the more efficient the confinement of light and thus the slower the decay rate of the cavity photon (Eqn. 2.14). For the study of strong exciton-photon coupling, this has often led to the development of extremely high Q cavities to maximize the photon lifetime.[163]

In organic semiconductors, microcavity polaritons have been observed in a variety of one-dimensional (1D) microcavity structures (FP cavities).[123,124,163,172] The mirrors of the microcavity may consist of metallic films or dielectric stacks tailored to form a distributed Bragg reflector (DBR), and are separated by a distance that yields a cavity resonance near degeneracy with the semiconductor excited state. Materials such as TeO_2, SiN_x, HfO_2 and TiO_2, and SiO_2 and LiF have been used as the high and low index components of the DBR, respectively.[163] The system of TeO_2/LiF is of particular interest as it is compatible with thermal evaporation.[163] The reflectivities of DBRs can approach unity for large numbers of pairs. In contrast, while metallic mirrors are convenient for the study of microcavity polaritons under electrical excitation, they have much lower reflectivities limited by the optical losses of the metal. While metal-metal microcavities typically have Q~10, structures containing DBR-metal or DBR-DBR reflectors can have Q>100.[163,172] Due to the large exciton oscillator strength of organic

semiconductors, the regime of strong exciton-photon coupling has been observed in organic semiconductor microcavities with Q as low as 10.[172]

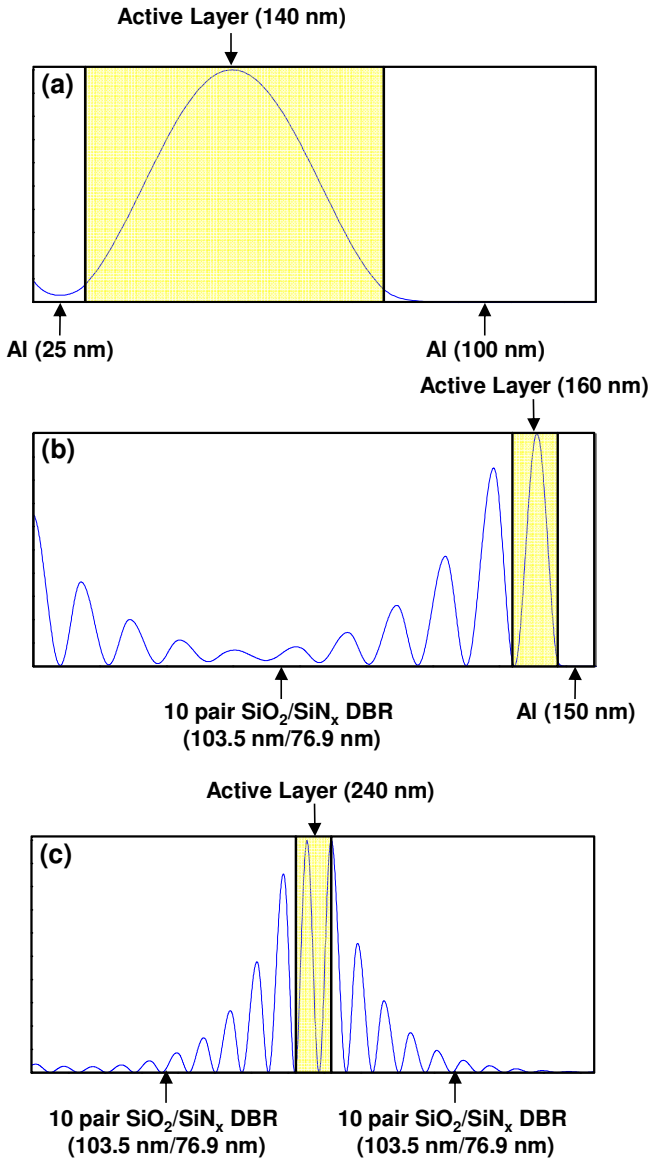

Figure 2.23 Simulated optical field intensity profiles for metal-metal, (a) DBR-metal, (b) , and DBR-DBR (c) microcavities with a n=1.8, k=0 active layer.

The overlap of the optical field with the active layer is also a factor in determining the Rabi splitting (Fig. 2.23). Metal mirrors inherently have negligible optical field

penetration depth, leading to larger overlap of the optical field and the organic semiconductor active layer. Metal-metal microcavities have thus been shown to exhibit massive Rabi splittings of ~300 meV.[172] Constructive interference from successive reflections in a DBR leads to a substantial optical field penetration into the reflector resulting in Rabi splittings that are considerably smaller than their metal-metal counterparts. This being said, these systems do exhibit a considerably larger quality factor and hence, narrower spectral features.[163] In addition, the photon and polariton lifetimes are considerable larger in systems constructed using low-loss DBRs.[132]

2.5.3 Moving Forward

Although both PL[124,129,130,132,133] and EL[127] from strongly coupled organic microcavities have been previously reported, the mechanism for the excitation of the polariton branches remains an area of continued research. Of interest is the significant difference in emission intensity between the lower and upper polariton branches observed under optical and electrical excitation.[111,112,114,127,132,134,173] Further, there has been only a single report of EL from strongly coupled organic microcavities, illustrating the need for more investigation into the mechanism for the population of polariton states under electrical excitation.[127] This thesis is aimed at understanding the mechanisms responsible for polariton excitation under both optical and electrical excitation and utilizing the knowledge gained to engineer novel polariton based optoelectronic devices. As such, the thesis is organized as follows. Chapter 3 is a systematic study of the discrepancy in emission intensity from the upper and lower branch polariton states under both optical and electrical pumping. A theoretical model is developed which elucidates the formation

mechanisms of polaritons. In Chapter 4, the knowledge gained in the modeling of polariton excitation mechanisms is applied and a novel device architecture is developed which permits efficient excitation of both the lower and upper branch polaritons. Chapter 5 seeks to utilize the newly developed architecture to study, more completely, the physics of strongly coupled metal-metal microcavities. Next, Chapter 6 employs the novel architecture developed in Chapter 4 in a hybrid organic-inorganic microcavity utilized to electrically excite inorganic polaritons without the need for charge carriers in the inorganic active layer. The work presented in Chapter 7 is focused on a different optical feedback structure to achieve strong exciton-photon in organic semiconductors which allows for a longer range strong exciton-photon than can be achieved in typical 1D microcavities. Finally, Chapter 8 discusses the implications of this work and potential future directions of the field of organic polariton devices.

Chapter 3 Thermally activated population of microcavity polariton states under optical and electrical excitation

3.1 Introduction

A key issue associated with organic semiconductor microcavities is that polariton emission does not correlate with branch photon character as discussed in Sec. 2.3.4 and shown in Fig. 3.1.[124,127,129,132] In these systems, emission from the upper polariton branch is many orders of magnitude smaller in intensity than that originating from the lower branch. In order to realize optoelectronic devices based on microcavity polaritons,[71,153,155] it is important to clearly understand the origin of this discrepancy, and the processes responsible for the population of the upper and lower polariton branches.[111,112,132,134,173,174] In this chapter, the formation mechanism for microcavity polaritons is elucidated by characterizing PL and EL from metal-metal microcavities containing the organic semiconductor tetraphenylporphyrin (TPP).[130] For consistency, the same microcavity structure is characterized using angle-resolved measurements of reflectivity, PL, and EL as a function of both temperature and exciton-photon detuning. The population of the upper polariton branch is modeled by means of thermal activation from an uncoupled exciton reservoir. Here, the activation energy for the population of the upper polariton branch is equal to the energetic separation between the exciton

reservoir and the upper branch at the angle of detection. Agreement between the model and the experimental data is obtained under both optical and electrical excitation.

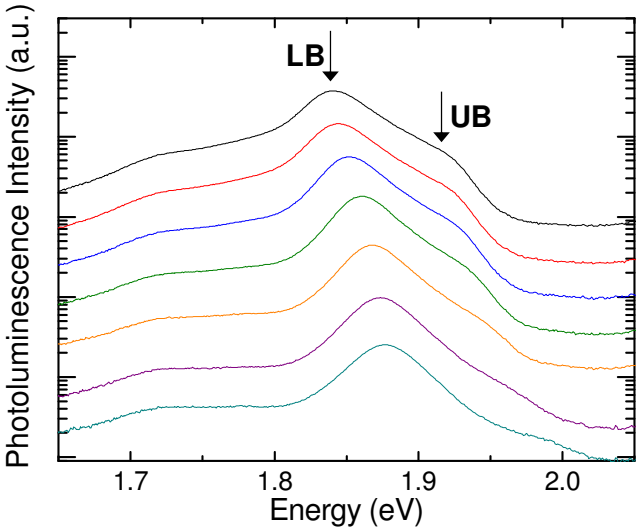

Figure 3.1 Angle-resolved photoluminescence (PL) of an organic semiconductor microcavity. Polariton emission does not correlate with the branch photon character. Emission from the upper polariton branch (denoted with UB) is many orders of magnitude smaller in intensity than that originating from the lower polariton branch (denoted with LB). The PL spectra are plotted on a logarithmic scale to better resolve the upper polariton branch emission.

This chapter is organized as follows. In Sec. 3.2, the experimental details including device fabrication and various characterization techniques are described. The theoretical basis used to interpret the experimental results is developed in Sec. 3.3, while experimental results are presented in Sec. 3.4. A discussion of the results is provided in Sec. 3.5, and the conclusions and future directions are presented in Sec. 3.6.

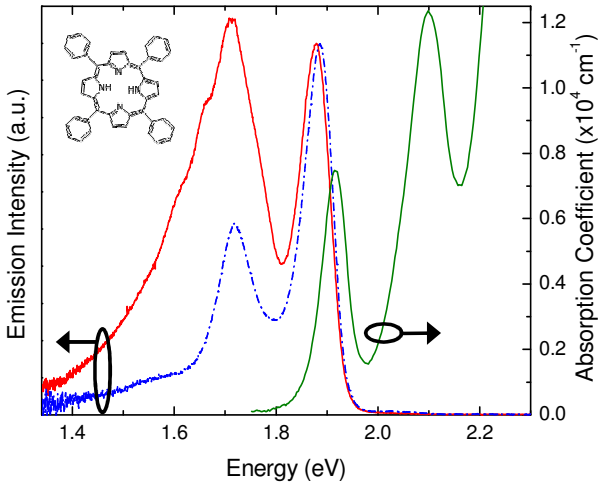

Figure 3.2 Absorption coefficient, photoluminescence (PL, broken line), and electroluminescence (EL, solid line) for a 70-nm-thick film of TPP collected at 300K. The PL spectrum was collected under excitation at a wavelength of 405 nm. The EL spectrum was collected using the bottom-emitting microcavity structure described in Sec. II with the Ag anode omitted. The driving current density was 100 mA/cm^2. Inset: The chemical structure of tetraphenylporphyrin.

3.2 Experimental

The absorption, PL and EL of the active material TPP are shown in Fig. 3.2. Two different microcavity architectures containing TPP were explored to facilitate the measurement of angle-resolved reflectivity, PL and EL at room temperature (Fig. 3.3a), and measurements of PL and EL as a function of temperature at fixed angle (Fig 3.3b). In both structures, all device layers were deposited using thermal sublimation at a pressure of ~8x10^{-7} Torr. For room temperature measurements of reflection, PL, and EL, a glass slide coated with a 150-nm-thick layer of indium-tin-oxide (ITO) was used as the substrate. The microcavity (Fig. 3.3a) consisted of a 50-nm-thick layer of Ag, a 30-nm-thick hole-transport layer of *N,N′*-Bis(naphthalen-1-yl)-*N,N′*-bis(phenyl)-benzidine

(NPD), a 70-nm-thick layer of TPP, and a 30-nm-thick electron-transport layer of bathocuproine (BCP). The device cathode consisted of a 0.5-nm-thick layer of LiF followed by a 50-nm-thick layer of Al. Here, light is collected through the semi-transparent Ag anode.

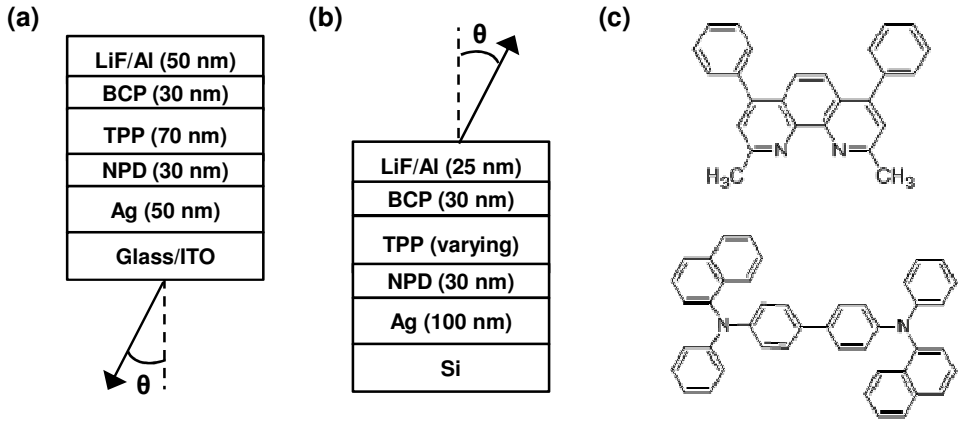

Figure 3.3 The microcavity architectures for luminescence measurements at (a) room temperature and (b) variable temperature. (c) The chemical structures for bathocuproine (BCP, top) and *N,N′*-Bis(naphthalen-1-yl)-*N,N′*-bis(phenyl)-benzidine (NPD, bottom).

For temperature-dependent measurements of microcavity luminescence, a polished Si wafer (intrinsic) was used as the substrate to improve thermal coupling to the device active layers. A top-emitting architecture was used to facilitate light extraction for measurements carried out in a cryostat. The device (Fig. 3.3b) consisted of a 100-nm-thick layer of Ag which serves as the anode, a 30-nm-thick layer of NPD, a 55- or 65-nm-thick layer of TPP, a 30-nm-thick layer of BCP and a cathode consisting of a 0.5-nm-thick layer of LiF followed by a 25-nm-thick layer of Al. Here, light is collected through the semi-transparent Al cathode. Due to the change in microcavity architecture, the TPP layer thickness is reduced slightly to permit the study of both the bottom- and top-emitting structures at similar exciton-photon detunings. In each structure, the Ag anode

and Al cathode serve both as electrodes and reflectors to form the optical microcavity.[127,172]

Optical microcavities were studied using angle-resolved measurements of reflectivity, PL, and EL. Reflectivity measurements were carried out using a variable-angle spectroscopic ellipsometer under p-polarized monochromated white light. Photo- and electroluminescence spectra were collected as a function of angle using an optical fiber-coupled spectrometer. Devices were optically excited using a laser at a wavelength of λ=405 nm (60 mW) for PL measurements. For EL measurements, the devices were held at a constant current density of 100 mA/cm^2.

A single port optical cryostat was used for temperature dependent measurements of PL and EL. For PL measurements, a longpass filter with a cut-off wavelength of λ=488 nm was used to prevent the detection of the pump laser, and the excitation was performed at an angle of 10° from normal. Under both optical and electrical excitation, normal incidence emission spectra were measured as a function of temperature.

3.3 Theory

This section outlines a model for the population of upper and lower branch polariton modes that builds off previous work by Ceccarelli et al.[134] Here, the emission intensity ratio between the upper and lower branches is modeled under optical and electrical excitation. Non-resonant excitation of the microcavity leads to the creation of energetic excitons which relax to form an exciton reservoir.[50] Further relaxation from the reservoir can occur by a variety of mechanisms (Fig. 3.4). Reservoir excitons may

undergo radiative or non-radiative decay without coupling (with a total rate of $k_{TOT}=k_R+k_{NR}$), may form states which are localized and unable to couple,[110] or may couple with the cavity photon mode and populate the upper (k^u) and lower (k^l) branch polariton states. Excitation from the exciton reservoir to the upper polariton branch requires an input of thermal energy. Such phonon-assisted processes are likely facilitated in TPP by the energetic breadth of the uncoupled exciton reservoir.[149-151,158,173] Since population of the upper branch is a thermally activated process, most reservoir excitons relax into the lower branch.

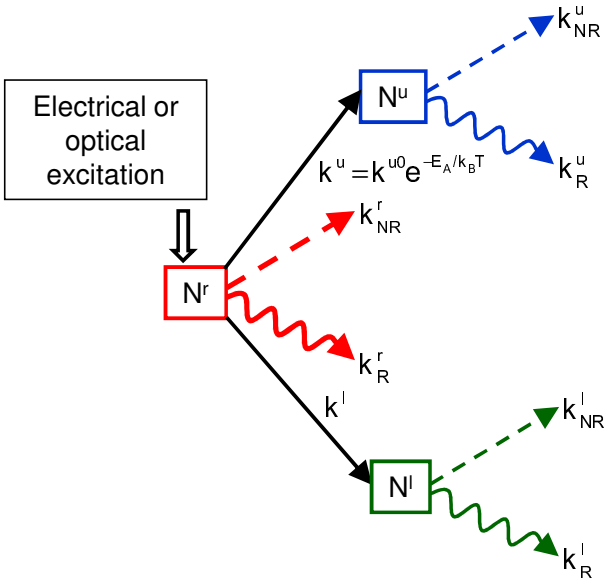

Figure 3.4 Exciton relaxation and microcavity polariton formation according to the proposed model. A full explanation of the model is provided in the text.

The polariton formation process described above is modeled using rate equations for the populations of the exciton reservoir (N^r) and the upper and lower polariton branches, N^u and N^l, respectively:

$$\frac{dN^r}{dt} = -k^r_{TOT}N^r - k^l N^r - k^{u0}e^{-E_A/k_BT}N^r + G \tag{3.1}$$

$$\frac{dN^u}{dt} = -k_{TOT}^u N^u + k^{u0} e^{-E_A/k_B T} N^r \quad (3.2)$$

$$\frac{dN^l}{dt} = -k_{TOT}^l N^l + k^l N^r \quad (3.3)$$

In Eqns. 3.1-3.3, k_B is the Boltzmann constant and T is the ambient temperature. Terms referring to the reservoir excitons, upper and lower branch polaritons are denoted by the superscripts *r*, *u*, and *l*, respectively. The total decay rates for each of the populations are defined as k_{TOT}^r, k_{TOT}^u, and k_{TOT}^l. The rates k^{u0} and k^l, are the temperature independent rates of relaxation and excitation from the reservoir into the upper and lower branches, respectively. The reservoir exciton generation rate (optical or electrical) is G. In this model, polaritons created with arbitrary in-plane wavevector do not undergo further relaxation in energy due to their short radiative lifetime.[132] For high finesse microcavity structures, polaritons may undergo relaxation in the upper and lower branches.[111,112] The upper polariton branch is populated by the excitation of reservoir excitons with activation energy, E_A.[134]

Equations 3.1-3.3 can be solved simultaneously under steady-state excitation to obtain expressions for N^r, N^u, and N^l. The corresponding emission intensity can be expressed as:[66]

$$I^j = \frac{\left(k_R^j\right)^2}{k_{TOT}^j} \frac{d_{Exc} hc}{\lambda^j} N^j \quad (3.4)$$

where h and c are the Planck constant and speed of light, respectively, and the superscript *j* denotes either *r, u, or l*. The emission wavelength in each case is denoted by λ^j, and d_{Exc} is the width of the exciton recombination zone. The width of the exciton recombination zone in an organic light-emitting device is typically tens of nanometers.[175,176] Under

optical excitation, d_{Exc} can be considerably larger and depends strongly on the absorption coefficient of the organic material. However, when calculating the ratio of luminescence intensities this term cancels, and therefore does not impact the analysis and conclusions drawn from this model. In terms of N^r, the intensities of Eqn. 4 can be re-written as:

$$I^r = \frac{\left(k_R^r\right)^2}{k_{TOT}^r}\frac{d_{Exc}hc}{\lambda^r}N^r \tag{3.5}$$

$$I^r = \frac{\left(k_R^u\right)^2}{k_{TOT}^u}\frac{d_{Exc}hc}{\lambda^u}k^{u0}e^{-E_A/k_BT}N^r \tag{3.6}$$

$$I^l = \frac{\left(k_R^l\right)^2}{k_{TOT}^l}\frac{d_{Exc}hc}{\lambda^l}k^l N^r \tag{3.7}$$

Using Eqns. 3.6 and 3.7, the ratio of upper to lower branch emission can be written as:

$$\ln\left(\frac{I^u}{I^l}\right) = \ln(\chi) - \frac{E_A}{k_BT} \tag{3.8}$$

where χ depends on the rates of polariton decay and transfer from the reservoir, and the respective emission wavelengths as:

$$\chi = \frac{\lambda^l}{\lambda^u}\frac{k^{u0}}{k^l}\left(\frac{k_R^u(k_R^l+k_{NR}^l)}{k_R^l(k_R^u+k_{NR}^u)}\right)^2 \tag{3.9}$$

with:[132]

$$k_R^{u,l} \approx \frac{\alpha_{u,l}^2}{\tau_{cav}} \tag{3.10}$$

where α^2 is the relative weight of the photon component of the branch of interest, and τ_{cav} is the lifetime of the cavity photon. Equation 3.10 reflects the fact that in TPP, τ_{cav} (~12 fs) is much shorter than the uncoupled exciton lifetime of 0.31 ns.[177] Similarly, the ratio of upper branch emission intensity to reservoir exciton emission intensity can be expressed using Eqns. 3.5 and 3.6 as:

$$\ln\left(\frac{I^u}{I^r}\right) = \ln(\Psi) - \frac{E_A}{k_B T} \tag{3.11}$$

with:

$$\Psi = k^{u0}\frac{\lambda^r}{\lambda^u}\left(\frac{k_R^u}{k_R^r}\right)^2 \frac{k_R^r + k_{NR}^r}{\left(k_R^u + k_{NR}^u\right)^2} \tag{3.12}$$

The emission wavelengths and radiative decay rates for the upper and lower branches (Eqn. 3.10) can be substituted into Eqns. 3.9 and 3.12 to estimate k^l and k^{u0}, the respective rates of polariton population from the reservoir.

3.4 Results

3.4.1 Microcavity reflectivity at room temperature

The room temperature thin film absorption coefficient, PL, and EL of TPP are shown in Fig. 3.2. The optical transition of interest for strong coupling is centered at (1.90 ± 0.02) eV with a full-width half-maximum (FWHM) of (61 ± 5) meV.[130,178] In PL and EL, the transitions of interest are centered at (1.89 ± 0.02) eV and (1.88 ± 0.02) eV, with FWHM of (69 ± 5) meV and (68 ± 5) meV, respectively. Angle-resolved reflectivity spectra for the microcavity structure of Fig. 3.3a are shown in Fig. 3.5a. Two prominent features are observed as a result of strong coupling between the cavity photon and the absorption resonance at 1.90 eV. These features show strong dispersion with angle of incidence and anti-cross around the uncoupled exciton energy.[99] Figure 3.5b shows the corresponding dispersion relation extracted by multi-peak fitting the spectra in Fig. 3.5a. The dispersion relation was fit using a coupled-oscillator model (Eqn. 2.21 without the broadening terms) to yield a Rabi splitting of (80 ± 5) meV.[99]

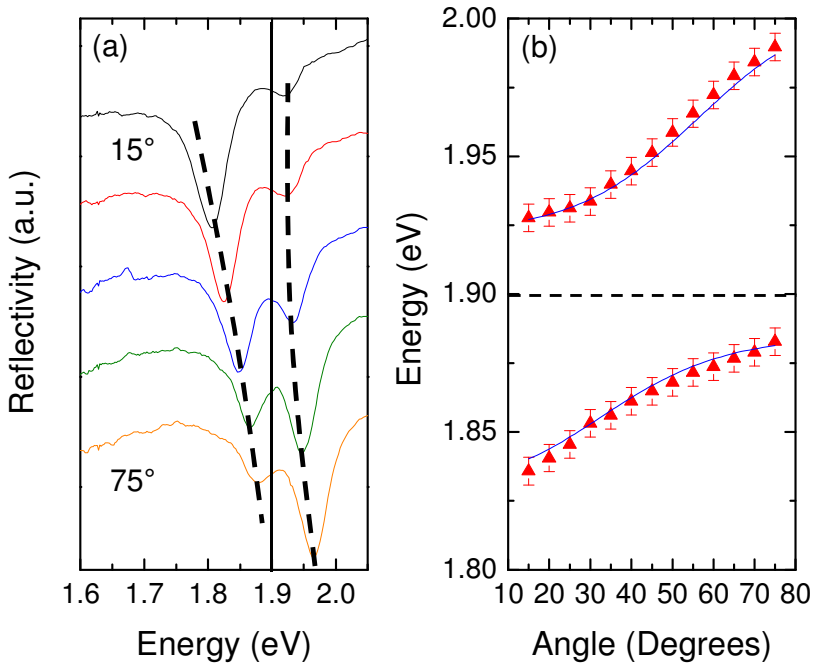

Figure 3.5 (a) Reflectivity spectra collected at angles of incidence ranging from 15° to 75° in steps of 15° for the microcavity of Fig. 3.3a. The broken lines highlight the dispersion of strongly coupled features with angle. The uncoupled exciton energy is denoted by a solid line. (b) Dispersion relation obtained from reflectivity. Solid lines are fits to the data based on a coupled-oscillator model. The broken line indicates the position of the exciton reservoir.

3.4.2 Room temperature measurements of microcavity luminescence

Figure 3.6a shows angle-resolved PL for the microcavity in Fig. 3.3a. Here, a logarithmic plot is used to better resolve emission from the upper polariton branch between 1.90 and 2.05 eV. This feature shows clear dispersion with angle, confirming its origin as the upper polariton branch. Due to the low cavity quality factor (Q~28),[66] significant uncoupled emission from TPP is also observed between 1.6 and 1.8 eV. Multi-peak fitting (Gaussian) was performed on the emission spectra to extract the position of each feature and construct a dispersion curve (Fig. 3.6b). As with the dispersions

obtained from measurements of reflectivity, fitting of the dispersion curve yields a Rabi splitting of (72 ± 5) meV.

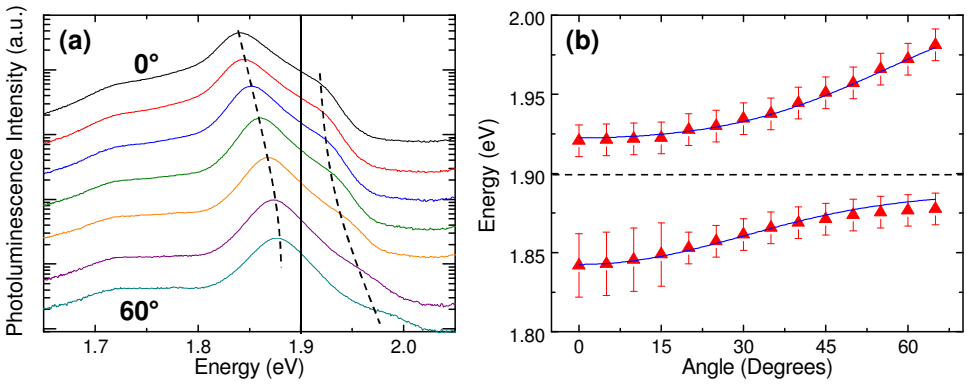

Figure 3.6 (a) Logarithmic plot of angle-resolved photoluminescence (PL) and the corresponding dispersion relation (b). For the spectra, broken lines indicate the position of the strongly coupled features while the solid lines indicate the position of the uncoupled exciton energy of TPP. For the dispersion relations, solid lines are fits to the data based on a coupled-oscillator model while the uncoupled exciton energy is indicated by a broken line.

Angle-resolved microcavity EL spectra are shown in Fig. 3.7a, and are similar to those obtained under optical excitation. Again, the spectra are shown on a logarithmic plot to accentuate the upper polariton branch. As in PL, significant uncoupled emission from TPP is observed between 1.6 and 1.8 eV. The corresponding dispersion relation is shown in Fig. 3.7b for the microcavity of Fig. 3.3a, characterized by a Rabi splitting of (72 ± 5) meV.

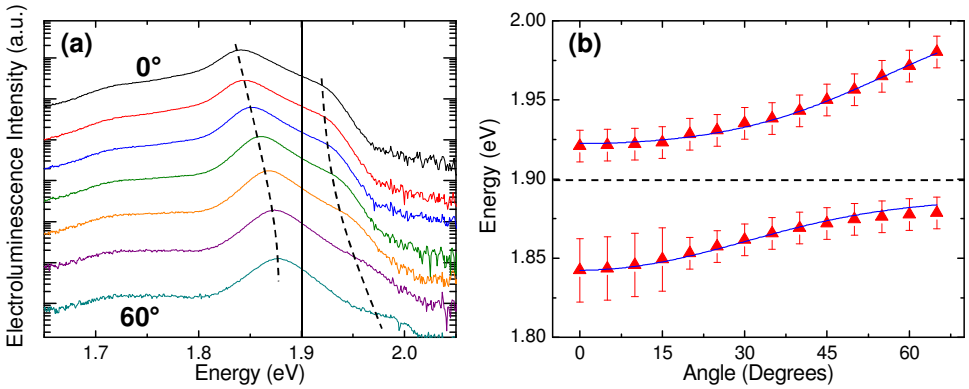

Figure 3.7 (a) Logarithmic plot of angle-resolved electroluminescence (EL) and the corresponding dispersion relation (b). For the spectra, broken lines indicate the position of the strongly coupled features while the solid lines indicate the position of the uncoupled exciton energy of TPP. For the dispersion relations, solid lines are fits to the data based on a coupled-oscillator model while the uncoupled exciton energy is indicated by a broken line.

3.4.3 Temperature dependence of microcavity luminescence

Microcavity luminescence was also examined as a function of temperature using the top-emitting device architecture described in Sec. 3.2 and shown in Fig. 3.3b. The PL and EL were collected as a function of temperature for microcavities containing either (55 ± 2) nm or (65 ± 2) nm of TPP. Varying the thickness of TPP changes the cavity mode energy, permitting a variation in the exciton-photon energy detuning. This in turn leads to a variation in the energetic separation between the polariton branches and the exciton reservoir.

Normal incidence PL was collected over a temperature range of 156K to 292K (Fig. 3.8a) or 130K to 298K (Fig. 3.8b) for devices containing either 55 nm or 65 nm of TPP, respectively. Similar EL spectra were also collected from microcavities containing

either 55 nm or 65 nm of TPP over a temperature range of 144K to 298K (Fig. 3.8c) or 140K to 295K (Fig. 3.8d), respectively. The upper and lower polariton branches and uncoupled exciton emission are denoted by the labels UB, LB and Unc., respectively. Significant uncoupled emission is observed as a result of the low microcavity quality factor (Q ~ 36).[132,134,179] The spectra in Fig. 3.8 demonstrate a clear increase in upper branch polariton emission intensity with increasing temperature while the uncoupled emission intensity decreases with increasing temperature, relative to the lower branch.

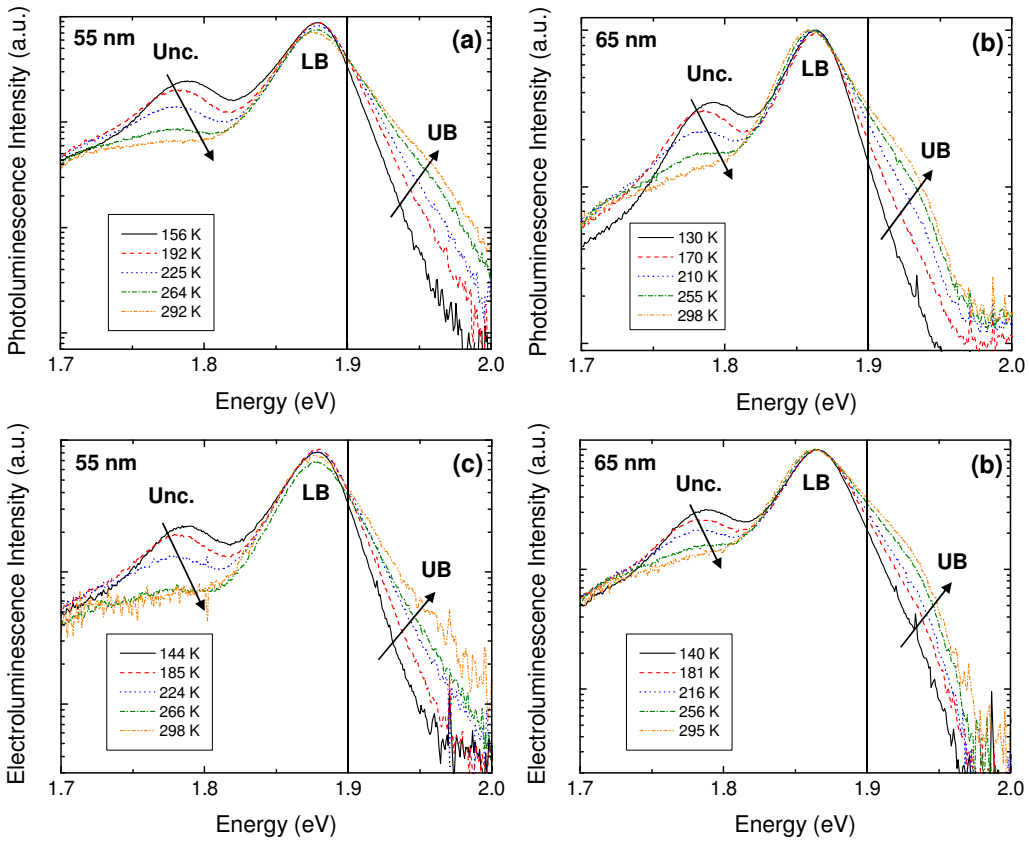

Figure 3.8 Photoluminescence (a) and (b) and electroluminescence (c) and (d) spectra collected at normal incidence as a function of temperature for the microcavity of Fig. 1c. Data for microcavities containing 55 nm of TPP is shown in parts (a) and (c) while data for microcavities containing 65 nm of TPP is shown in parts (b) and (d). The spectra shown in (a) through (d) are not normalized. The vertical solid line in each figure denotes the position of the uncoupled exciton energy of TPP, while the arrows denote the direction of increasing temperature. The labels Unc., LB and UB indicate emission from uncoupled reservoir excitons, lower branch polaritons and upper branch polaritons, respectively.

In order to extract peak positions and intensity from the spectra of Fig. 3.8, and throughout this chapter, multi-peak fitting (Gaussian) was performed on both PL and EL spectra. Figure 3.9 shows an example of this deconvolution for a PL spectrum collected at a temperature of 210K for a sample (Fig. 3.8c) containing a 65-nm-thick layer of TPP. The two polariton features are clearly identified along with uncoupled emission from TPP which is best fit using two peaks. Both peak centers and integrated emission intensities were obtained in this way to construct the intensity ratios used for comparison with Eqns. 3.8 and 3.11.

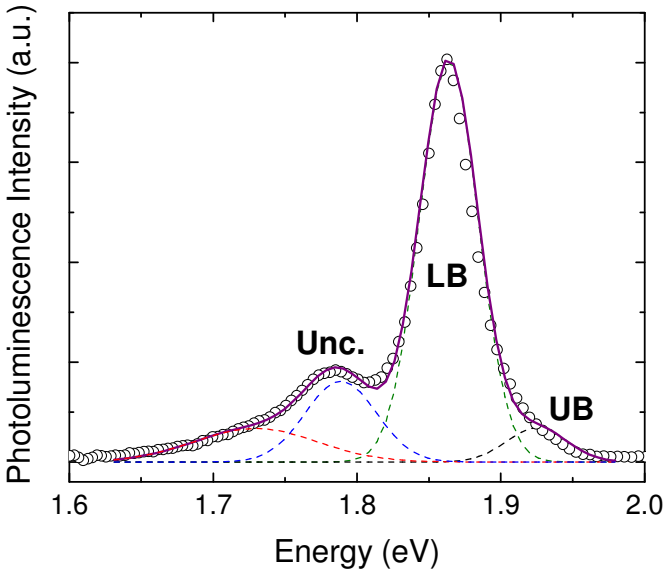

Figure 3.9 Multi-peak fitting for a photoluminescence spectrum from Fig. 3.7 collected at 210K on a device containing 65 nm of TPP (open circles). The spectrum is deconvoluted by multi-peak fitting with four Gaussian peaks representing uncoupled emission (Unc., 2 peaks), lower branch emission (LB) and upper branch emission (UB).

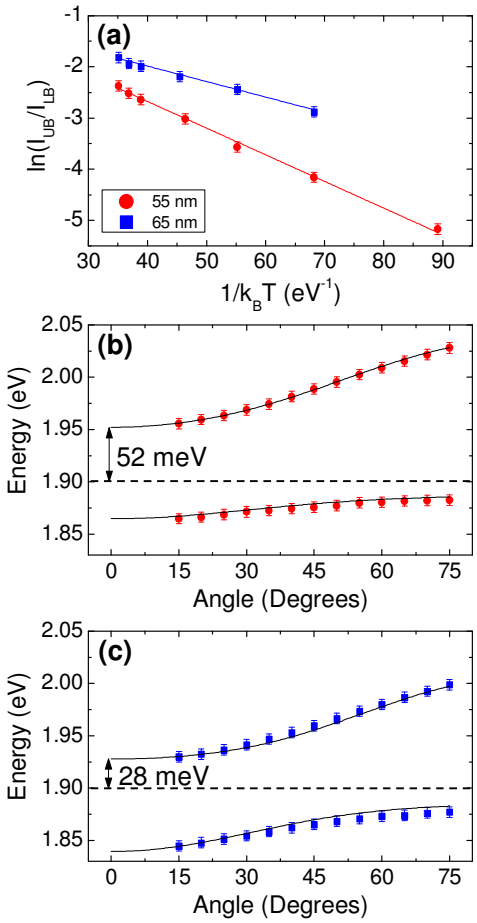

Figure 3.10 (a) Temperature dependent ratios of upper branch to lower branch photoluminescence intensity for the microcavity of Fig. 3.3b. Dispersion relations obtained from angle-resolved reflectivity for microcavities containing either 55 nm (b) or 65 nm (c) of TPP. In (b) and (c), the solid lines are fits based on a coupled-oscillator model while broken lines denote the position of the uncoupled exciton reservoir.

Figure 3.10a shows the dependence of the upper branch to lower branch PL ratio on temperature for microcavities (Fig. 3.3b) containing either 55 nm or 65 nm of TPP. The temperature dependence was fit using Eqn. 3.8 to yield activation energies of (52 ± 2) meV and (30 ± 2) meV, and χ values of (0.50 ± 0.03) and (0.55 ± 0.03) for microcavities containing either 55 nm or 65 nm of TPP, respectively. These parameters

are summarized in Table 3.1. The PL intensity of TPP was separately measured outside of the microcavity to have a negligible dependence on temperature. Dispersion relations obtained from angle-resolved reflectivity measurements performed on microcavities containing either 55 nm or 65 nm of TPP are shown in Figs. 3.10b and 3.10c. The dispersion relations were fit with a coupled-oscillator model.

The ratio of the upper branch to lower branch integrated EL intensity was also extracted and plotted as a function of temperature for each detuning (Fig. 3.11a). Fitting the temperature dependence with Eqn. 3.8 yields activation energies of (57 ± 2) meV and (30 ± 2) meV, and χ values of (0.46 ± 0.03) and (0.55 ± 0.03) for microcavities containing either 55 nm or 65 nm of TPP, respectively. These parameters are summarized in Table 3.1. Again, dispersion relations obtained from angle-resolved reflectivity are shown for each detuning in Figs. 3.11b and 3.11c, and were fit using a coupled-oscillator model.

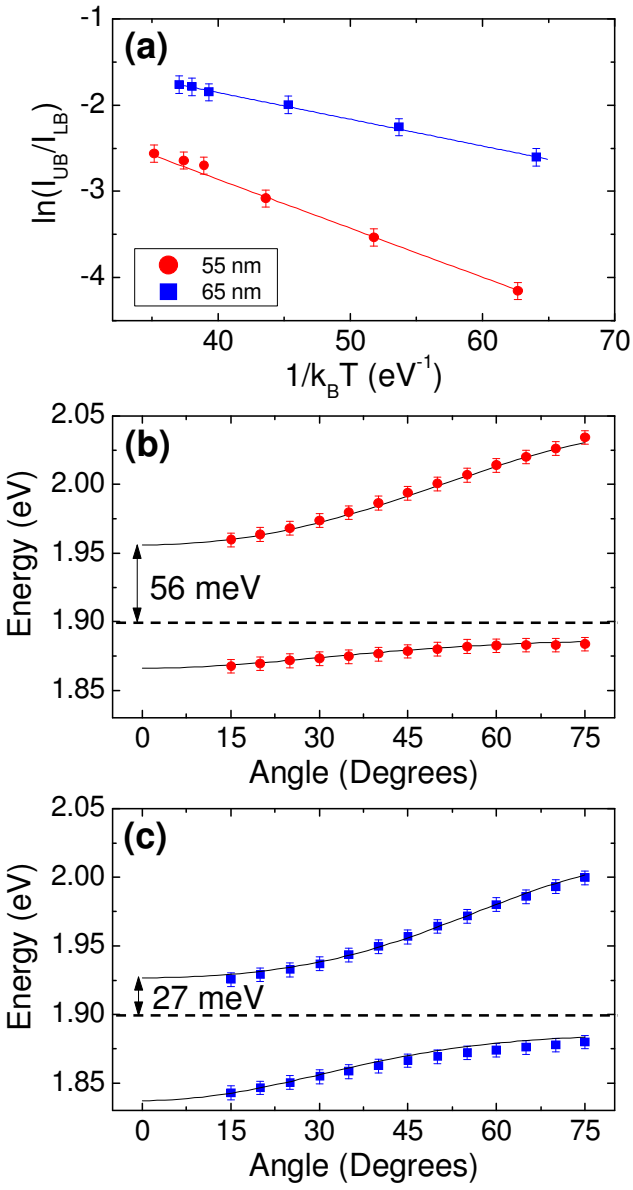

Figure 3.11 (a) Temperature dependent ratios of upper branch to lower branch electroluminescence intensity for the microcavity of Fig. 3.3b. Dispersion relations obtained from angle-resolved reflectivity for microcavities containing either 55 nm (b) or 65 nm (c) of TPP. In (b) and (c), the solid lines are fits based on a coupled-oscillator model while broken lines denote the position of the uncoupled exciton reservoir.

3.5 Discussion

3.5.1 Exciton-photon coupling at room temperature

The PL and EL spectra shown in Figs. 3.6 and 3.7 exhibit a significant intensity difference for emission from the lower and upper polariton branches. The lower branch emission intensity correlates well with the photon character of the branch. At angles below resonance, lower branch states are mostly photon-like, and have a shorter radiative lifetime giving rise to efficient emission. At angles above resonance, the emission intensity from lower branch states is reduced due to its exciton-like character and hence longer radiative lifetime. To summarize, lower branch polariton luminescence is more intense at low angles than high angles and emits consistent with the photon character. This observation is comparable with previous reports of PL from strongly coupled organic microcavities.[124,127,132] The emission intensity of the upper branch does not exhibit the same dependence on branch character and is instead described using the model of Sec. 3.3.

3.5.2 Temperature dependence of microcavity luminescence

3.5.2.1 Activated population of the upper polariton branch

At normal incidence, the energetic separations between the upper branch and the exciton reservoir are (52 ± 5) meV and (28 ± 5) meV for optically excited microcavities containing either 55 nm or 65 nm of TPP, respectively (Figs. 3.10b and 3.10c). These values compare favorably with the activation energies of (52 ± 2) meV and (30 ± 2) meV extracted from the fits in Fig. 3.10a. Similarly, Figs. 3.11b and 3.11c show dispersion curves obtained from angle-resolved reflectivity for samples examined under electrical

excitation. Upper branch-exciton reservoir energetic separations of (56 ± 5) meV and (27 ± 5) meV are observed at normal incidence for microcavities containing 55 nm or 65 nm of TPP, respectively. These values are in good agreement with the activation energies of (57 ± 2) meV and (30 ± 2) meV extracted from the fits in Fig. 3.11a. The correlation between the measured activation energies and the energetic separation between the exciton reservoir and the upper branch (Table 3.1) supports a model of upper branch population via thermal activation. Thus, while emission from the lower branch reflects the branch photon character, emission from the upper branch is determined by the rate of population from the exciton reservoir.

Table 3.1 Parameters for temperature dependent luminescence measurements

Parameters determined from fitting the model in Sec. 3.3 to the data in Figs. 3.10 and 3.11 for microcavities containing either 55 nm or 65 nm of TPP.

	Photoluminescence			**Electroluminescence**		
Thickness (nm)	σ (meV)[a]	E_A (meV)	χ	σ (meV)[a]	E_A (meV)	χ
55	52 ± 5	52 ± 2	0.50 ± 0.03	56 ± 5	57 ± 2	0.46 ± 0.03
65	28 ± 5	30 ± 2	0.55 ± 0.03	27 ± 5	30 ± 2	0.55 ± 0.03

[a]σ is the energetic separation between the upper polariton branch and the uncoupled exciton reservoir at an angle of zero degrees.

3.5.2.2 Population rates of the upper and lower polariton branches

While previous work has examined the ratio of upper to lower branch PL intensity as a function of temperature, there has not been an attempt to extract branch population rates from the temperature dependence of the luminescence.[134] The procedure for

extracting the polariton branch population rates is described as follows. First, the intercepts (χ) extracted from fits of Eqn. 3.8 in Figs. 3.10a and 3.11a are manipulated to obtain values for the ratio of the upper branch population rate (k^{u0}) to the lower branch population rate (k^{l}). Second, the intercepts extracted from fits of Eqn. 3.11 to the ratio of upper branch to reservoir exciton emission intensity (not shown) are used to calculate the upper branch transfer rate k^{u0}, allowing the lower branch excitation rate (k^{l}) to be extracted from the aforementioned ratio of k^{u0} to k^{l}.

The vertical-axis intercepts extracted from the fits of Figs. 3.10a and 3.11a can be used to calculate the ratio of k^{u0} to k^{l} using Eqn. 3.9. This calculation is made under two assumptions namely, that the non-radiative decay rate for lower and upper branch polaritons is the same as that of the uncoupled exciton, and that the non-radiative decay rate is much smaller than the rate of radiative decay from the upper and lower branches. The latter assumption suggests that non-radiative relaxation is not competitive with polariton or reservoir exciton luminescence. The cavity photon lifetime can be calculated from the quality factor yielding a value of 12 fs,[66] allowing the microcavity polariton radiative decay rates to be calculated using Eqn. 3.10. Since both the relaxation rate to the lower branch (k^{l}) and the rate of transfer from the exciton reservoir to the upper branch (k^{u0}) are unknown, only the ratio of k^{u0} to k^{l} can be determined from the fits of Fig. 3.10a and 3.11a. Substitution into Eqn. 3.9 yields k^{u0} to k^{l} ratios of (0.44 ± 0.05) and (0.53 ± 0.05), from PL measurements, and (0.48 ± 0.05) and (0.53 ± 0.05), from EL measurements. In both cases the ratios are determined for microcavities containing either 55 nm or 65 nm of TPP. The ratios of k^{u0} to k^{l} are summarized in Table 3.2 along with

their dependence on the energetic separation between the upper branch and the exciton reservoir. Although k^{u0} is defined as the temperature independent rate of transfer to the upper branch, ratios less than unity suggest that this rate is slower than the relaxation of excitons from the reservoir to the lower branch.

The model developed in Sec. 3.3 can be further examined by fitting the ratio of upper branch to reservoir emission intensity as a function of temperature with the Eqn. 3.11 as shown for PL and EL in Fig. 3.12a and 3.12b, respectively. These fits yield activation energies for the population of the upper branch that are identical to those extracted from Figs. 3.10a and 3.11a. The corresponding values of the intercept (ψ) are (1.60 ± 0.04) and (1.77 ± 0.04) for microcavities containing 65 nm of TPP for PL and EL, respectively. Values of ψ for microcavities containing 55 nm of TPP are (17.92 ± 0.04) and (19.22 ± 0.04) for PL and EL, respectively. Equation 3.12 can be used with ψ to calculate a value for the upper branch transfer rate k^{u0}. Assuming that the non-radiative decay rate is small with respect to the radiative rate, k^{u0} can be calculated in terms of the radiative decay rate of uncoupled reservoir excitons in the cavity. The results are (1.48 ± 0.05)*k_R^r and (1.64 ± 0.05)*k_R^r from PL and EL measurements on microcavities containing 65 nm of TPP. Based on k_R=3.2 x 10^9 s^{-1} for TPP,[177] and assuming that $k_R^r \sim k_R$, temperature independent upper branch excitation rates (k^{u0}) of 4.7 x 10^9 s^{-1} and 5.2 x 10^9 s^{-1}, are calculated from measurements of PL and EL, respectively. At 300K, these values for k^{u0} give overall rates of upper branch excitation (k^u) of 1.5 x 10^9 s^{-1} and 1.6 x 10^9 s^{-1}. The same method can be used to calculate temperature independent upper branch excitation rates for a microcavity containing 55 nm of TPP. These rates are

summarized in Table 3.2 for both microcavities along with the corresponding upper branch-exciton reservoir and lower branch-exciton reservoir energetic separations.

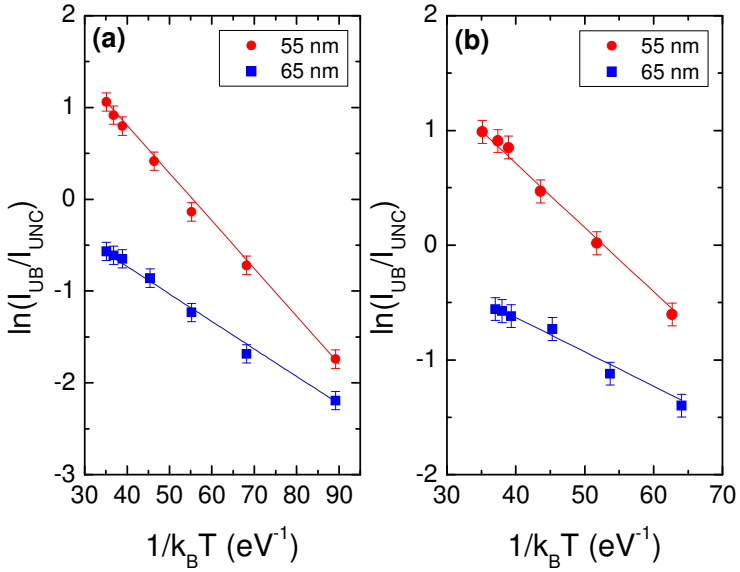

Figure 3.12 Temperature dependent ratios of upper branch to uncoupled photoluminescence (a) and electroluminescence (b) intensity for the microcavity of Fig. 3.3b containing either 55 nm or 65 nm of TPP.

Prior work suggests that the excitation rate from the reservoir to the upper branch should increase with the energetic separation (σ) between the upper branch and reservoir for branch energies close to the reservoir.[111] For higher energy states in the upper branch, the rate of excitation from the reservoir is expected to decrease with increasing σ.[111] The experimental results presented here for TPP reflect the behavior expected for low energy states near the exciton reservoir. In particular, k^{u0} for a microcavity containing a 55 nm-thick layer of TPP is a factor of ~10 larger than that obtained for a microcavity containing

a 65 nm-thick layer of TPP (Table 3.2). This is consistent with an increase in σ for microcavities containing 55 nm of TPP.

Table 3.2 Polariton excitation rates obtained from the model in Sec. 3.3.

Polariton excitation rates calculated from the fit parameters in Table 3.1 as discussed in Sec. 3.5.2.2 of the text.

	Photoluminescence		**Electroluminescence**	
	55 nm TPP	65 nm TPP	55 nm TPP	65 nm TPP
σ (meV)[a]	52 ± 5	28 ± 5	56 ± 5	27 ± 5
δ (meV)[b]	35 ± 5	61 ± 5	34 ± 5	63 ± 5
k^{u0}/k^{l}	0.44 ± 0.05	0.53 ± 0.05	0.48 ± 0.05	0.53 ± 0.05
k^{u0} (s^{-1})	$(5.2 \pm 0.1) \times 10^{10}$	$(4.7 \pm 0.2) \times 10^{9}$	$(5.6 \pm 0.1) \times 10^{10}$	$(5.2 \pm 0.2) \times 10^{9}$
k^{l} (s^{-1})	$(1.2 \pm 0.1) \times 10^{11}$	$(8.9 \pm 0.9) \times 10^{9}$	$(1.2 \pm 0.1) \times 10^{11}$	$(9.8 \pm 0.9) \times 10^{9}$

[a]σ is the energetic separation between the upper polariton branch and the uncoupled exciton reservoir at an angle of zero degrees.
[b]δ is the energetic separation between the uncoupled exciton reservoir and the lower polariton branch at an angle of zero degrees.

Combining the calculated values of k^{u0} with the ratios of k^{u0} to k^{l} previously determined allows the lower branch excitation rate to be estimated as a function of exciton-photon detuning (Table 3.2). Prior theoretical work on strong coupling in organic semiconductors has suggested that the rate of relaxation from the exciton reservoir to the lower branch should decrease as the energetic separation between these states (δ) is increased.[111] The data presented here for microcavities containing TPP show this trend as k^{l} is reduced by a factor of ~10 as the thickness of the TPP layer is increased from 55 nm

to 65 nm (Table 3.2). Increasing the thickness of the TPP layer leads to an increase in δ at normal incidence. Overall, the lower branch transfer rates k^l determined in this work for TPP (Table 3.2) are similar to those predicted for microcavities containing J-aggregate films.[111,180,181]

3.5.3 Summary

Previous studies of PL from strongly coupled organic microcavities have shown that luminescence from the upper polariton branch is very weak in intensity relative to that from the lower polariton branch.[111,112,134,173] In this chapter, the emission from an organic microcavity was examined under both optical and electrical excitation, and a formalism was developed that accurately predicted the difference between the lower branch and upper branch polariton emission intensities for both PL and EL. Fitting the temperature dependent microcavity luminescence intensities yielded activation energies that corresponded to the energy difference between the upper branch and the reservoir energy. Using this model, the rates of population of the upper and lower branches from the exciton reservoir were determined. The knowledge gained of the excitation mechanisms responsible for polariton excitation is paramount. The weak population of the upper polariton branch can be overcome by choosing an alternate excitation scheme. This scheme circumvents the exciton reservoir by exciting polaritons directly.

Chapter 4 Electrical excitation of microcavity polaritons by radiative pumping from a weakly coupled organic semiconductor

4.1 Introduction

In Chapter 3, it was revealed that the population of organic microcavity polariton states occurs via an uncoupled exciton reservoir. Consequently, this results in the inefficient excitation of the upper polariton branch, and a significant population of uncoupled excitons in the active material.[111,112,132,134] Since reservoir excitons may themselves undergo radiative or non-radiative decay prior to populating either the upper or lower branch, the intermediate population of the reservoir may constitute a potential loss channel, reducing the fraction of the pump excitation that results in microcavity polariton formation.[132,134] This is reflected by the observation of weak upper branch emission relative to the lower branch and significant uncoupled emission in microcavity luminescence measurements.[124,127,130,132] Bimolecular quenching processes between reservoir excitons and microcavity polaritons have also been suggested as a potential pathway for additional loss.[181]

In order to circumvent these complications, an alternate excitation approach is demonstrated in this chapter that permits the direct population of microcavity polariton states under both electrical and optical excitation without first forming an exciton reservoir. This is realized by introducing a weakly coupled emitter into an optical microcavity containing an organic semiconductor suitable for strong exciton-photon

coupling. In contrast to previous work on microcavity polariton luminescence in organic semiconductors, angle-resolved measurements of the photo- and electroluminescence show variations in upper and lower branch emission intensity consistent with the branch photon character.[99] These results confirm that the excitation of the microcavity polariton states is by radiative pumping from the weakly coupled emitter.

This chapter is organized as follows. In Sec. 4.2, the experimental details including the device structure and fabrication, and various characterization techniques are described. The radiative pumping scheme is also discussed in Sec. 4.2. The theoretical basis used to verify the existence of radiative pumping is developed in Sec. 4.3, while experimental results are presented in Sec. 4.4. A discussion of the results and summary is provided in Sec. 4.5.

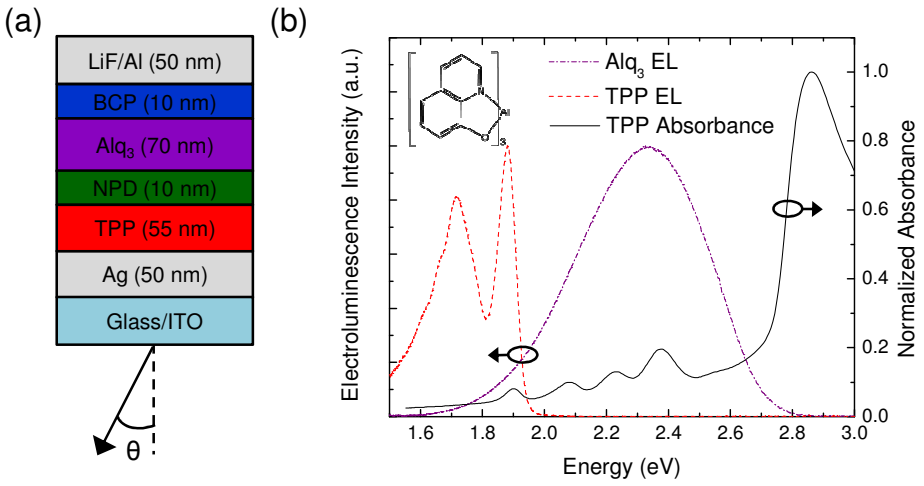

Figure 4.1 (a) Microcavity architecture of interest for the study of radiative pumping. (b) Absorption (solid line) and electroluminescence (EL, broken line) spectra of TPP, and the electroluminescence (dotted line) of Alq_3. The EL spectra of TPP and Alq_3 were obtained in device architectures consisting of ITO/30 nm NPD/70 nm TPP or Alq_3/30 nm BCP/0.5 nm LiF/50 nm Al, respectively at a current density of 100 mA/cm^2. Inset: Molecular structure of Alq_3.

4.2 Experiment

Optical microcavities were constructed by depositing organic and metallic layers onto a glass substrate coated with a 150-nm-thick layer of indium-tin-oxide (ITO) using vacuum thermal sublimation at 8×10^{-7} Torr. Prior to layer deposition, substrates were degreased with solvents and cleaned by exposure to UV-ozone ambient. The microcavity structure (Fig. 4.1a) consisted of a 50-nm-thick layer of Ag, a layer of tetraphenylporphyrin (TPP) of varying thickness (as discussed in Chapter 3), a 10-nm-thick layer of the hole-transporting material *N,N'*-Bis(naphthalen-1-yl)-*N,N'*-bis(phenyl)-benzidine (NPD), a 70-nm-thick layer of the electron-transporting material aluminum tris(8-hydroxyquinoline) (Alq_3), and a 10-nm-thick layer of the exciton/hole-blocking material bathocuproine (BCP). The device cathode consisted of a 0.5-nm-thick layer of LiF and a 50-nm-thick layer of Al. The metallic anode (Ag) and cathode (Al) of the device also serve as reflectors forming an optical microcavity.[127,172]

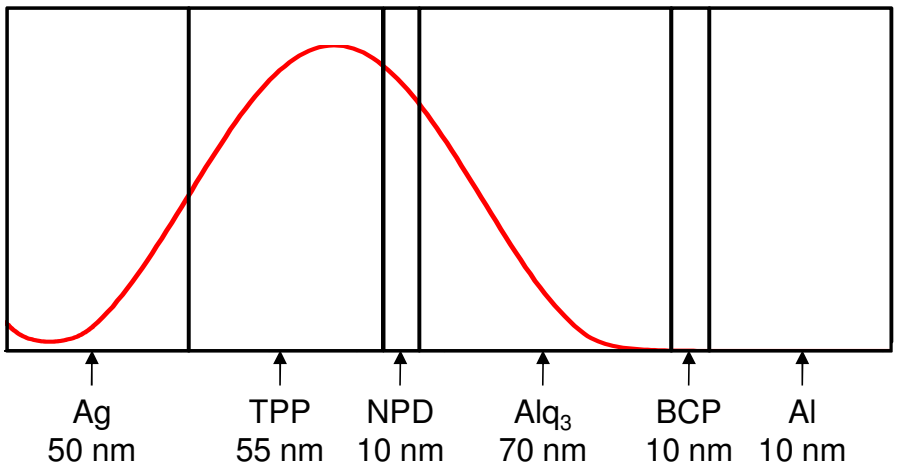

Figure 4.2 Simulated optical field via the transfer matrix formulism (Chapter 5) for the device of Fig. 3.1a. Significant overlap of the optical field with TPP is maintained despite the proximity of the TPP layer to the metallic anode.

The layer of TPP serves as the active material for the observation of strong exciton-photon coupling.[130] Despite the proximity of TPP to the metallic anode, significant overlap with the optical field is maintained as shown in Fig. 4.2. The microcavity is tuned to resonance with the excitonic transition of TPP at (1.90 ± 0.02) eV (Fig. 4.1b). The broad absorption and emission (Fig. 4.1b) features of Alq_3 ensure only a weak coupling with the cavity photon mode.[79] The energy gap of the NPD layer is larger than that of Alq_3, preventing the direct excitation of TPP by blocking electrons and also preventing Förster energy transfer from Alq_3.[182] As further evidence, devices constructed on ITO with no bottom reflector show EL only from Alq_3 (Fig. 4.3), confirming that there is no exciton formation on TPP. When excited, Alq_3 radiatively populates the polariton modes of the microcavity (Fig. 4.4), circumventing the need to first create an uncoupled exciton reservoir. This excitation mechanism drastically alters the resulting electro- (EL) and photoluminescence (PL) observed from the cavity.

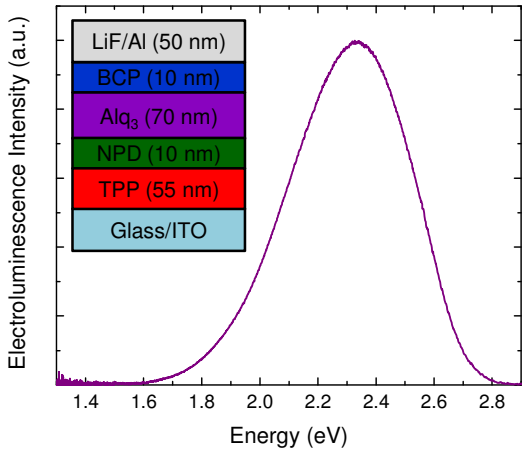

Figure 4.3 Electroluminescence (EL) spectra of Alq_3 obtained in a device architecture consisting of ITO/55 nm TPP/10 nm NPD/70 nm Alq_3/10 nm BCP/0.5 nm LiF/50 nm Al (Inset) driven at a current density of 100 mA/cm^2. EL is observed only from Alq_3 confirming that there is no exciton formation on TPP in the microcavity structure of Fig. 4.1a.

Microcavities were characterized using a variety of angle-resolved techniques. Reflectivity measurements were performed using a variable-angle spectroscopic ellipsometer under p-polarized light illumination. A polarizer was used to collect p-polarized EL and PL spectra as a function of detection angle. For measurements of EL, devices were excited at a constant current density of 100 mA/cm^2. For measurements of PL, microcavities were excited using a 60 mW laser at a wavelength of λ=405 nm. The laser was incident on the sample through the cathode in order to maximize the fraction of light absorbed in the Alq_3 layer.

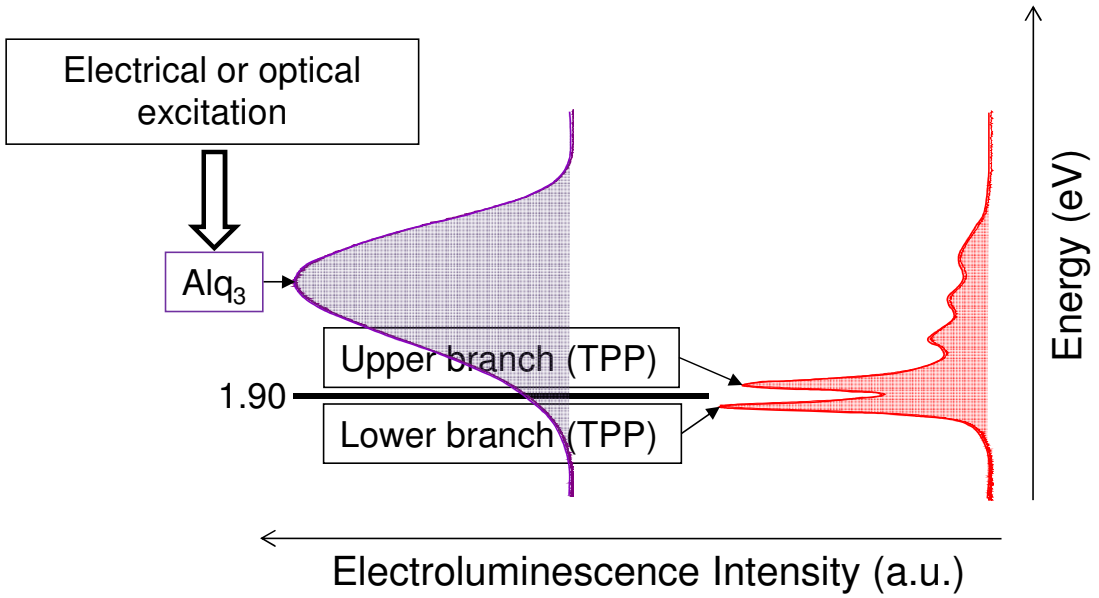

Figure 4.4 A schematic of the radiative pumping scheme. Broad luminescence from Alq_3 directly excites microcavity polariton states created by the coupling of the TPP exciton (1.90 eV) to the cavity photon. The result is clear, resolvable luminescence from both the upper and lower polariton branches.

4.3 Theory

The use of radiative pumping (Fig. 4.4) permits equal population of the upper and lower polariton branches. When both polariton branches are populated equally, the emission intensity is dictated by the relative photon character of each branch. To assess the degree to which the observed emission features vary according to their relative photon character, the integrated EL intensities are related to the photon character by building off of the following expression for emission from the lower (I^l) and upper (I^u) branches as developed in Chapter 3:[66]

$$I^{l,u} = \phi^{l,u} \frac{hcd_{Exc}}{\lambda^{l,u}} k_R^{l,u} N^{l,u} \tag{4.1}$$

where the emission efficiency and emission wavelength are denoted $\Phi^{l,u}$ and $\lambda^{l,u}$, respectively. The polariton population and radiative decay rates of the lower and upper branch are denoted by $N^{l,u}$ and $k_R{}^{l,u}$, respectively. Under electrical excitation, the exciton recombination zone (d_{Exc}) in Alq_3 is approximated as the layer thickness.[176] The emission efficiency is taken as unity for both the upper and lower branches assuming that the radiative decay rate is much larger than the non-radiative decay rate for polaritons. As given in Chapter 3, the radiative decay rate of a polariton is related to the cavity photon lifetime (τ_{cav}) and the relative weight of the photon component of the polariton (α^2) by:[132]

$$k_R^{u,l} \approx \frac{\alpha_{u,l}^2}{\tau_{cav}} \tag{4.2}$$

Assuming that the lower and upper branches are populated equally, the relative weight of the photon component of the upper branch ($\alpha_u{}^2$) can be written in terms of the EL intensity using Eqn. 4.1 as:

$$\alpha_u^2 = \frac{I^u \lambda^u}{I^l \lambda^l + I^u \lambda^u} \tag{4.3}$$

An analogous expression for the lower branch (α_l^2) can also be derived:

$$\alpha_l^2 = \frac{I^l \lambda^l}{I^l \lambda^l + I^u \lambda^u} \tag{4.4}$$

4.4 Results

Figure 4.5a shows angle-resolved reflectivity spectra for a microcavity containing a (55 ± 2) nm-thick layer of TPP. Two spectral features show strong dispersion with angle as a result of strong coupling between the cavity photon and the exciton resonance of TPP at 1.90 eV. A third feature observed at high energy results from coupling between the excitonic transition at 2.09 eV and the cavity mode. The dispersion relation of Fig. 4.5b was extracted from reflectivity and fit using a damped two-branch coupled-oscillator model (Eqn. 2.22) having the cavity length, the effective refractive index and the cavity mode linewidth as adjustable parameters, and the Rabi splitting and exciton energy as fixed parameters.[102] A Rabi splitting of (74 ± 10) meV was determined from the minimum energetic separation between the upper and lower branches. A cavity length of (142 ± 10) nm, a refractive index of (2.39 ± 0.04), and a cavity mode linewidth of (65 ± 3) meV were obtained from the fit. The obtained cavity length is close to the total organic layer thickness between the two electrodes.

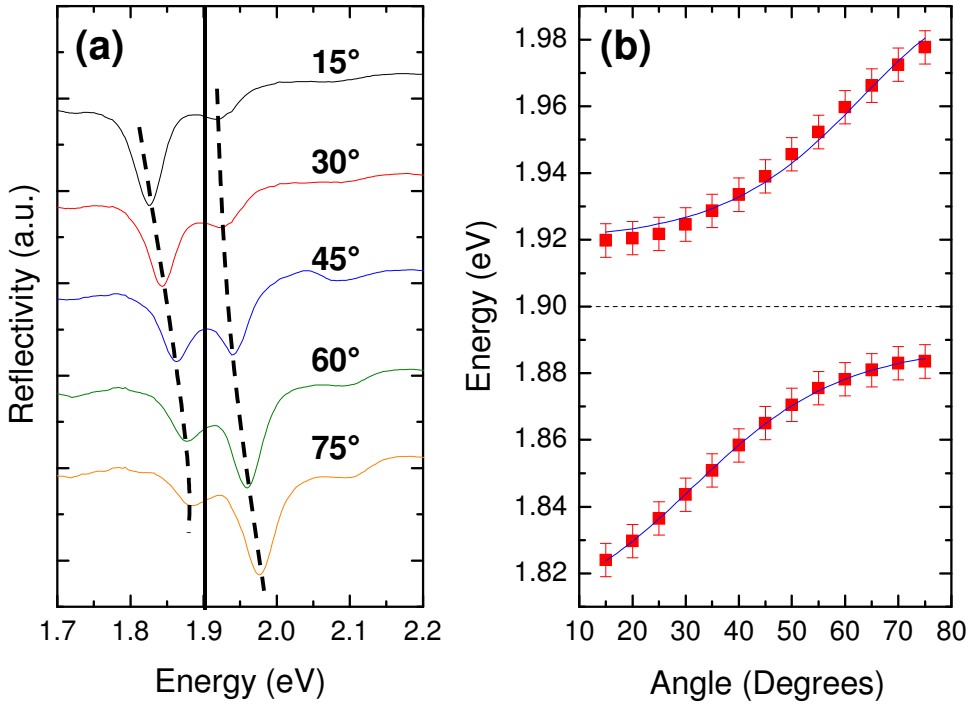

Figure 4.5 (a) Reflectivity spectra for a microcavity containing 55 nm of TPP. Broken lines highlight the dispersion of the lower and upper branch polariton features with angle. (b) Dispersion relation obtained from angle-resolved reflectivity measurements for the microcavity of (a). Solid lines are damped coupled-oscillator fits while the broken line indicates the position of the uncoupled excitonic transition of TPP.

Figures 4.6a and 4.6b show angle-resolved EL and PL spectra, respectively, for a device containing a (55 ± 2) nm-thick layer of TPP. As in reflectivity, two emission features exhibiting strong dispersion are observed as a result of coupling between the excitonic transition at 1.90 eV and the cavity photon. The additional feature observed at high energy again results from strong coupling between the cavity photon and the excitonic transition at 2.09 eV. Under electrical pumping, the intensity of the polariton features show dispersion with angle that reflects their photon character (Fig. 4.6a).

Emission from the two branches is nearly equal in intensity at ~45°, consistent with the reflectivity spectra of Fig. 4.5a. For measurements of PL (Fig. 4.6b), emission from the upper and lower branches is not equal in intensity at 45°. Here, the lower branch has additional weight due to direct optical pumping of TPP in addition to radiative pumping via Alq_3. The absorption coefficients for TPP, NPD, and Alq_3 at 405 nm were separately measured to be 3.6×10^5 cm^{-1}, 2.6×10^4 cm^{-1} and 3.1×10^4 cm^{-1}, respectively. As such, additional pumping of the exciton reservoir of TPP may occur via Förster energy transfer from NPD under optical pumping. Consequently, the electrically pumped structure is better-suited to examine radiative pumping of TPP since it permits the excitation to be localized to Alq_3. Nevertheless, intense emission from the upper branch is clearly observed under optical excitation as a result of radiative pumping from Alq_3.

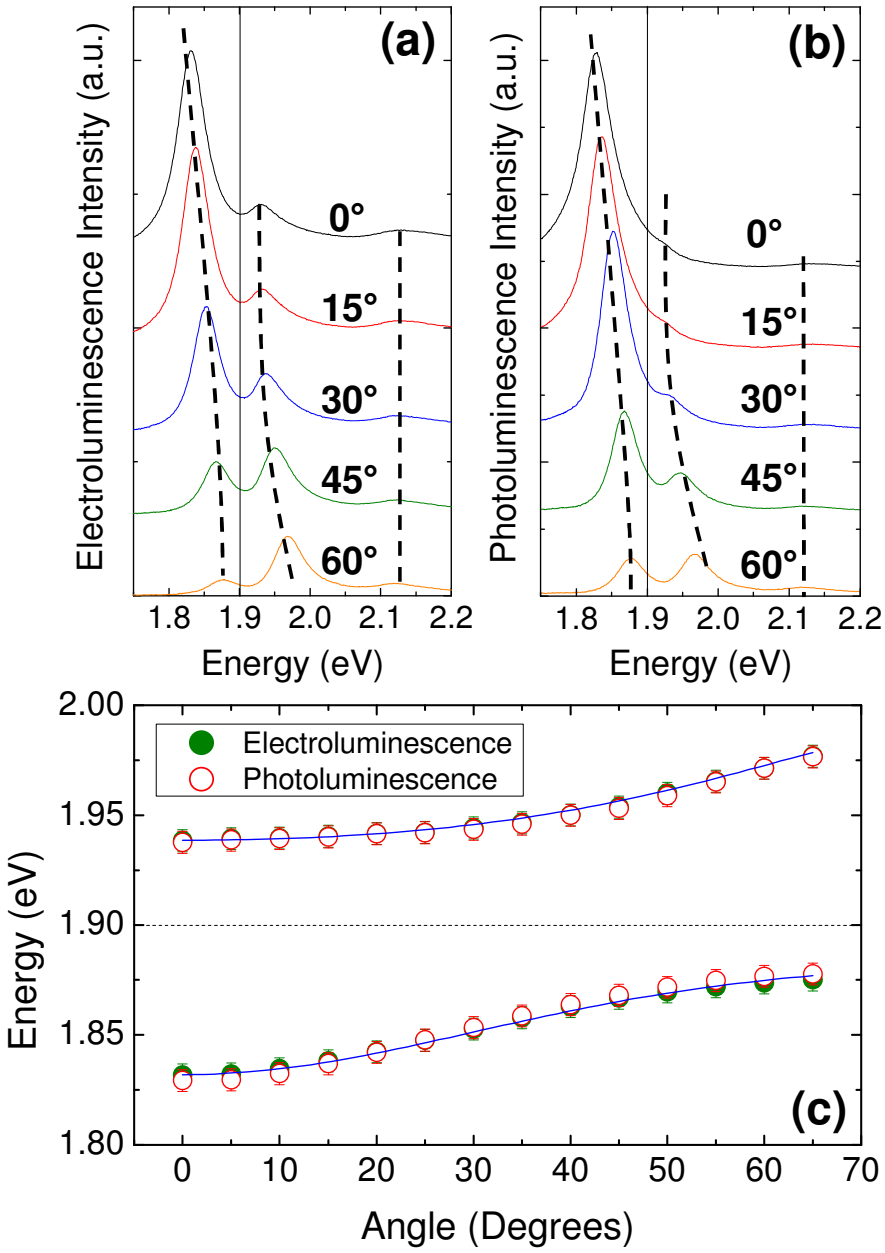

Figure 4.6 Angle-resolved electroluminescence (EL) (a) and photoluminescence (PL) (b) for the microcavity of Fig. 4.1a. Solid lines denote the position of the uncoupled excitonic transition of TPP while the broken lines highlight the dispersion of strongly coupled features with angle. (c) Dispersion relations extracted from angle-resolved measurements of EL and PL. The solid line is a damped coupled-oscillator fit of the EL and PL dispersions. The position of the TPP excitonic transition is indicated by the broken line.

The dispersion relations shown in Fig. 4.6c were constructed by using multi-peak fitting to extract peak centers from the spectra of Fig. 4.6a and 4.6b. Both the EL and PL dispersion relations were fit with a damped two-branch coupled-oscillator model (Eqn. 2.22). A Rabi splitting of (85 ± 5) meV was extracted from the energy difference between the upper and lower branches. The fit shown in Fig. 4.6c corresponds to a cavity length of (143 ± 10) nm, a refractive index of (2.36 ± 0.09) (the optical constants of TPP are given in Fig. 4.7) and a cavity mode linewidth of (76 ± 5) meV.

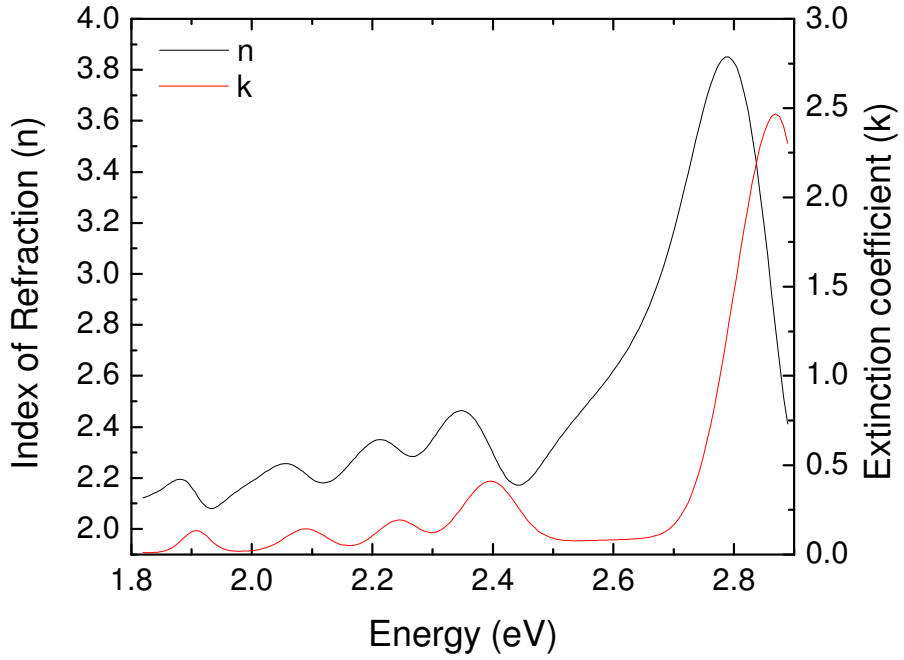

Figure 4.7 The index of refraction (n) and extinction coefficient (k) for a 75-nm-thick thin film of TPP on Si. The two damped two-branch coupled coupled-oscillator model fit of the microcavity dispersion of Fig. 4.6c yields a comparable index of refraction.

4.5 Discussion

Figures 4.8a and 4.8b show microcavity EL and PL for devices where the coupling medium (TPP) is excited either by radiative pumping from Alq_3 or through the TPP exciton reservoir. The microcavity architecture used for the radiative pumping of TPP is shown in Fig. 4.1a, while the microcavity used to study the pumping of TPP via the exciton reservoir consisted of a 50-nm-thick Ag anode, a 30-nm-thick layer of NPD, a 70-nm-thick layer of TPP, and a 30-nm-thick layer of BCP (Fig. 3.3a). The cathode consisted of a 5-nm-thick layer of LiF and a 50-nm-thick layer of Al. In the latter structure, the electrical or optical excitation leads to exciton formation in TPP and consequently polariton excitation via the exciton reservoir. Layer thicknesses were chosen to ensure a similar exciton-photon detuning for both structures. The pumping of TPP from the exciton reservoir (Figs. 4.8a and 4.8b, broken line) results mainly in the observation of lower branch emission, with only weak luminescence from the upper branch. When the TPP active layer is radiatively pumped (Fig. 4.8, solid line), luminescence from Alq_3 is absorbed by the microcavity polariton resonances.[130] This results in intense luminescence from both the upper and lower polariton branches, without first populating the exciton reservoir.[134] Due to the low cavity quality factor (Q~28), weak uncoupled emission from Alq_3 is also observed, with depressions in the spectra corresponding to absorption by the excitonic transitions of TPP at 2.22 eV and 2.38 eV.[132] No uncoupled emission is observed from TPP, suggesting that only polariton states are populated in the active layer.

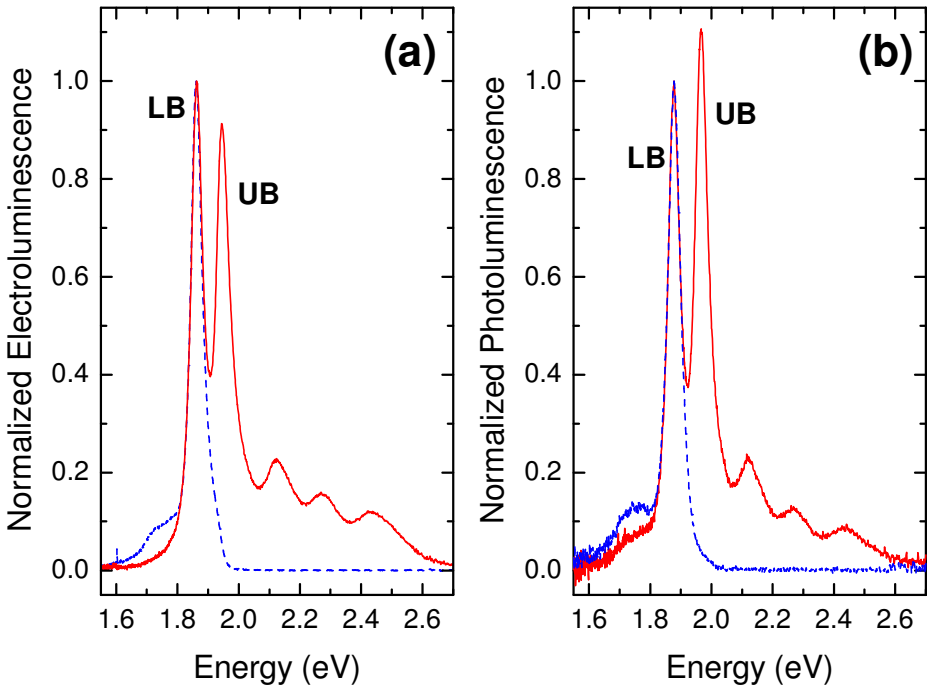

Figure 4.8 Normalized electroluminescence (EL) (a) and photoluminescence (PL) (b) for microcavity where the TPP active layer is excited via the exciton reservoir (broken line) or by radiative pumping (solid line). The spectra are for microcavities with similar detunings. Microcavity polariton luminescence is identified as originating from either the lower branch (LB) or upper branch (UB).

As discussed in Sec. 4.3, the degree to which the observed emission features vary according to their relative photon character can be assessed using Eqns. 4.3 and 4.4. The values obtained for the relative weight of the photon component from EL can be compared directly to the branch photon character extracted from the dispersion relation of Fig. 4.6c.[99] Figure 4.9 shows the result of this comparison for a microcavity containing 55 nm of TPP. The photon fraction derived from the peak EL intensities shows good agreement with the actual photon character obtained from the EL dispersion, confirming

that radiative pumping of microcavity polariton states circumvents any barrier for the population of the upper branch.

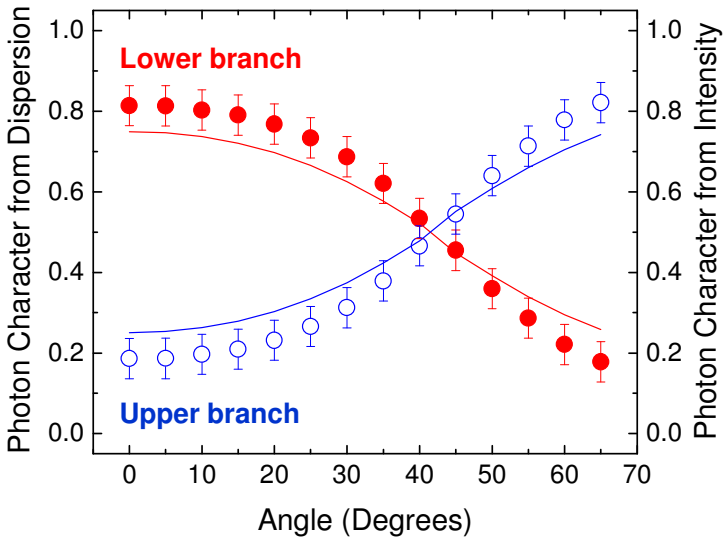

Figure 4.9 Photon character of the upper and lower polariton branches derived from the electroluminescence (EL) dispersion relation of Fig. 4.6c (solid lines) and the EL intensity of Fig. 4.6a using Eqn. 4.3 and Eqn. 4.4 (circles). The lower and upper branches are denoted by filled and open circles, respectively.

In many inorganic semiconductors, charge transport in the active coupling layer is problematic due to the potential for exciton screening and dissociation.[140,159] In order to radiatively pump such structures using the architecture discussed in this chapter, a thin, semi-transparent metal electrode can be included above the active layer to electrically pump the weakly coupled emitter. In this way, there is no charge transport through the active layer for strong coupling, and the excitation of polariton modes is exclusively by radiative pumping. This use of radiative pumping will ultimately facilitate the electrical excitation of polariton modes in inorganic semiconductors characterized by a small exciton binding energy (Chapter 7).

4.6 Radiative Pumping of Non-Emissive States

The utility of radiative pumping can be further examined by applying it to other systems where polariton states are not efficiently populated. In the case of optical microcavity systems containing a phosphorescent active layer, optical or electrical excitation results in the formation of singlet excitons which rapidly intersystem cross to triplet states before exciton-photon coupling can occur.[122,130] Consequently, a large fraction of the excitation results in uncoupled triplet emission with very little resulting in the formation of polaritons.[129,130] The radiative pumping technique described above offers a means to study emission from polariton states in these systems.

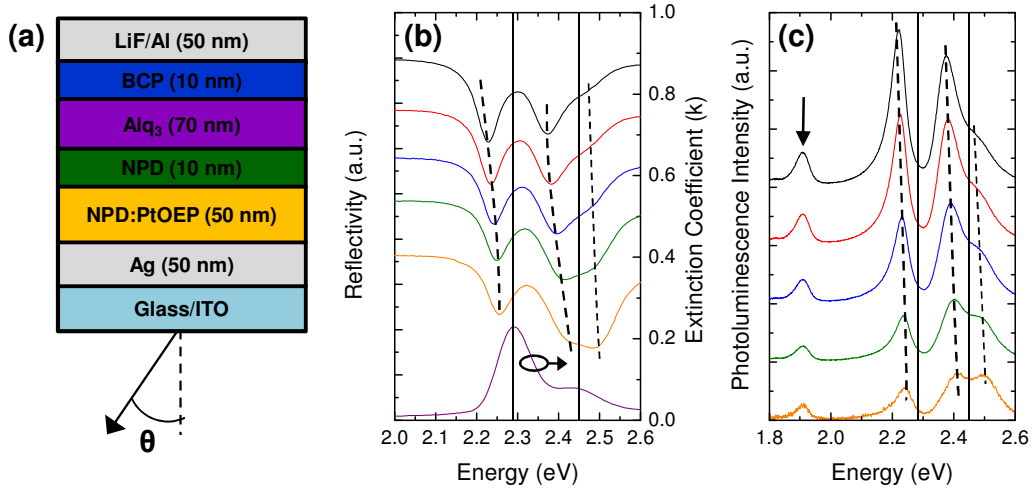

Figure 4.10 (a) Microcavity architecture of interest for the study of radiative pumping applied to a system containing a phosphorescent active layer. The extinction coefficient (b, broken line, also denoted with a circle and arrow) of a 50-nm-thick composite film of 1:1 NPD:PtOEP. The angle-resolved reflectivity (b, solid lines) and photoluminescence (c) for the microcavity of Fig. 4.10a. Broken lines serve as guides to the dispersion of the polariton resonances while the solid lines denote the position of the excitonic resonances of PtOEP. An arrow denotes the position of PtOEP triplet emission.

The microcavity structure (Fig. 4.10a) of interest consists of a 50-nm-thick layer of Ag, a 50-nm-thick composite film of 1:1 NPD:platinum octaethylporphyrin (PtOEP) (by wt.), a 10-nm-thick layer of the hole-transporting material *N,N′*-Bis(naphthalen-1-yl)-*N,N′*-bis(phenyl)-benzidine (NPD), a 70-nm-thick layer of the electron-transporting material aluminum tris(8-hydroxyquinoline) (Alq_3), and a 10-nm-thick layer of the exciton/hole-blocking material bathocuproine (BCP).[129,130] The device cathode consisted of a 0.5-nm-thick layer of LiF and a 50-nm-thick layer of Al. Platinum octaethylporphyrin serves as the active material for the observation of strong exciton-photon coupling.[130] As such, the microcavity is tuned to resonance with the excitonic transition of PtOEP at (2.29 ± 0.02) eV (Fig. 4.10b).[129,130]

Angle-resolved reflectivity and PL are shown in Fig. 4.10b and Fig. 4.10c, respectively for the microcavity of Fig. 4.10a. In both reflectivity and PL, two spectral features exhibit strong dispersion with angle of incidence as a result of strong coupling between the cavity photon and the exciton resonance of PtOEP at 2.29 eV. The additional feature observed at high energy results from coupling between the excitonic transition at 2.45 eV and the cavity photon (Fig. 4.10b). Significant uncoupled emission from the PtOEP triplet state is observed at low energies (~1.90 eV) in the angle-resolved PL spectra (Fig. 4.10c) as a consequence of the low cavity quality factor and direct excitation of PtOEP via the pump source. The use of radiative pumping results in efficient population of the PtOEP polariton states and effectively reduces the amount of excitation lost to intersystem crossing to the triplet state. In fact, polariton emission in this case is roughly 3 times as intense as triplet emission as demonstrated in Fig. 4.10c.

4.7 Summary

A microcavity architecture was demonstrated that permits the direct population of polariton states in an organic semiconductor, eliminating the need to first form an uncoupled exciton reservoir. Microcavity polaritons in this structure were radiatively pumped by a weakly coupled emissive layer under electrical or optical excitation. Luminescence originates from microcavity polariton modes and reflects the photon character of the upper and lower branches. The use of radiative pumping offers an alternate excitation scheme for the realization of polariton-based optoelectronic devices. Further, this excitation approach can serve as a novel platform through which to study polariton states which are typically not populated due to rapid exciton relaxation to lower energy, non-radiative states.[129,130,164,183,184] Additional physics, such as the behavior of microcavity polariton emission versus light polarization, can be examined now that clear upper and lower branch emission is observed.

Chapter 5 Polarization splitting an organic semiconductor microcavity with metallic reflectors

5.1 Introduction

As was the case in Chapters 3 and 4, measurements of polariton electroluminescence are often facilitated through the use of metallic reflectors that form the optical microcavity and also serve as device electrodes.[127] In this chapter, it is discovered that these structures exhibit a significant polarization splitting in measurements of angle-resolved reflectivity and electroluminescence (EL). A similar polarization splitting has been previously reported in microcavities where at least one reflector is a distributed Bragg reflector (DBR).[185,186] A DBR is a structure comprised of alternating layers of high and low index dielectrics selected for maximum refractive index contrast.[66] The dielectric layer thicknesses are chosen such that the reflections at each interface add constructively resulting in a high reflectivity stack.[66] As such, a polarization splitting arises due to the polarization-dependent, optical field penetration depth of the structure.[185,187,188] In this chapter, we characterize the polarization splitting in a metal-metal microcavity and attribute its origin to the polarization-dependent phase shift experienced by the optical field upon reflection from the metal electrodes.

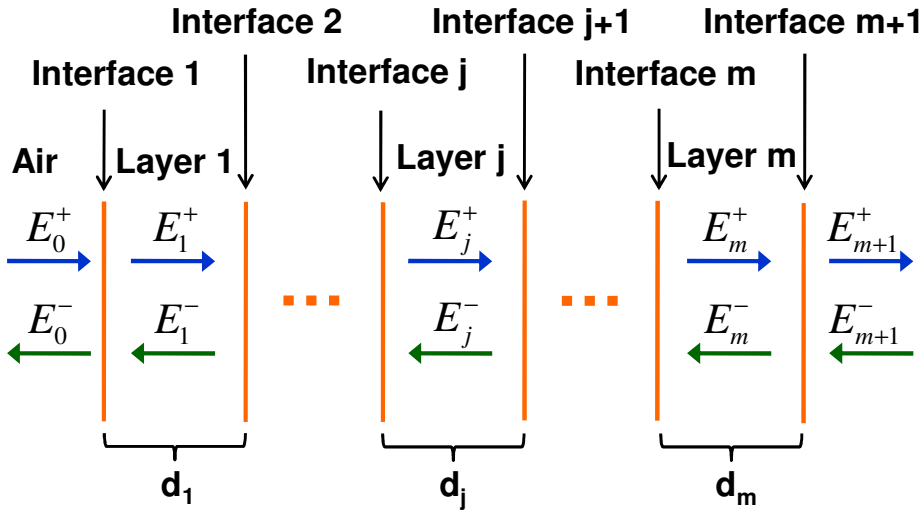

Figure 5.1 The transfer matrix formulism applied to a generic multilayer structure. E denotes the electromagnetic field in each layer while the superscripts indicate either a left-to-right (+) or a right-to left (-) traveling field. The thickness of each layer is denoted by d. The subscripts on both E and d indicate the layer of interest. The electromagnetic field in a given layer is calculated by multiplying the input field by the layer and interface matrices leading up to the layer of interest.

5.2 Theory

An optical transfer matrix formalism was employed to model the observed polarization dependent luminescence from organic semiconductor metal-metal microcavities. This one-dimensional transfer matrix model is outlined in Ref. 120 and assumes all layers are homogeneous and isotropic, interfaces between layers are parallel and flat, and incident light can be described by a plane wave. The optical properties of all layers and interfaces of the device are represented by a matrix:

$$I_j = \frac{1}{t_{jk}}\begin{bmatrix} 1 & r_{jk} \\ r_{jk} & 1 \end{bmatrix}, L_j = \begin{bmatrix} e^{-2\pi i q_j d_j/\lambda} & 0 \\ 0 & e^{2\pi i q_j d_j/\lambda} \end{bmatrix}, \quad (5.1)$$

where I is an interface matrix (subscript denotes which interface), L is a layer matrix (subscript denotes which layer), d_j is the thickness of layer j and λ is the wavelength. The complex index of refraction in the direction of propagation for layer j is denoted as q_j.

The Fresnel coefficients (r_{jk} and t_{jk}), which characterize the reflection (r_{jk}) and transmission (t_{jk}) at each interface, can be calculated with knowledge of the wavelength-dependent optical constants (the index of refraction n and the extinction coefficient k) of each material and the thickness of each layer.[189] As such, there are no free parameters in this simulation as all layer thicknesses and optical constants for the organic materials were measured via ellipsometry, and those for the metals were taken from literature.[190]

The propagation of an incident electromagnetic field through the structure is treated by considering the successive multiplication of layer and interface matrices.[120] Figure 5.1 shows a schematic of the process for multiple layers and interfaces. For instance, the electric field at layer 2 is the solution to the following matrix equation:

$$\begin{bmatrix} E_0^+ \\ E_0^- \end{bmatrix} = I_1 L_1 L_2 \begin{bmatrix} E_2^+ \\ E_2^- \end{bmatrix} \tag{5.2}$$

where E is the electromagnetic field (subscript denotes which layer the field is in and superscript denotes the direction of the field).

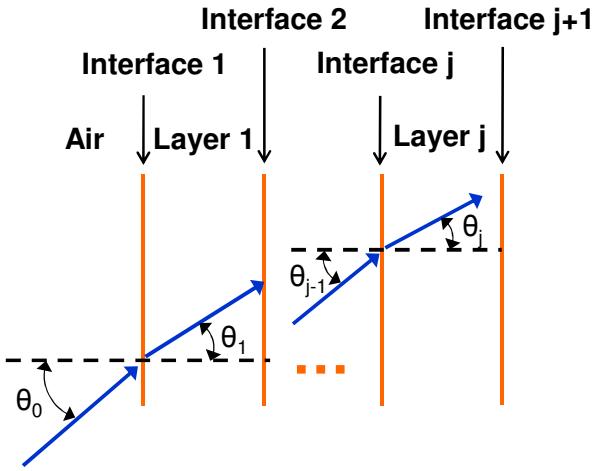

Figure 5.2 An illustration showing the angle of incidence (θ_0), and the angles of refraction in layers 1 (θ_1), j-1 (θ_{j-1}) and j (θ_j).

The complex index of refraction (q_j) for each layer ($\tilde{n} = n_j + ik_j$) in the direction of propagation is determined to calculate the reflection and transmission coefficients at each interface, and the layer matrices for each layer (Eqn. 5.1).[120]

$$q_j = \tilde{n}_j \cos(\theta_j) = \left[\tilde{n}_j^2 - n_0^2 \sin^2(\theta_0)\right]^{1/2} \tag{5.3}$$

θ_0 and θ_j are the angle of incidence on the structure and angle of refraction in layer j (Fig. 5.2) and n_0 is the index of refraction of the ambient (air). Assuming the incident light is polarized perpendicular to the plane of incidence (s-polarized) it follows that r_{jk} and t_{jk} at each interface jk (where k=j+1) are:[120]

$$r_{jk}^s = \frac{q_j - q_k}{q_j + q_k},\ t_{jk}^s = \frac{2q_j}{q_j + q_k} \tag{5.4}$$

Equation 5.4 can also be derived for the case when the incident light is polarized parallel to the plane of incidence (p-polarized):[120]

$$r_{jk}^p = \frac{\tilde{n}_j^2 q_j - \tilde{n}_k^2 q_k}{\tilde{n}_k^2 q_j + \tilde{n}_j^2 q_k},\ t_{jk}^p = \frac{2\tilde{n}_j^2 \tilde{n}_k^2 q_j}{\tilde{n}_k^2 q_j + \tilde{n}_j^2 q_k} \tag{5.5}$$

The total system transfer matrix (S) is derived by multiplying the interface and layer matrices in succession from the left to right in Fig. 5.1. This transfer matrix is then employed to evaluate the electromagnetic field output from the structure of interest by replicating Eqn. 5.2 for the entire device.[120]

$$\begin{bmatrix} E_0^+ \\ E_0^- \end{bmatrix} = S \begin{bmatrix} E_{m+1}^+ \\ E_{m+1}^- \end{bmatrix}, \text{ where } S = \begin{bmatrix} S_{11} & S_{12} \\ S_{21} & S_{22} \end{bmatrix} \tag{5.6}$$

The reflection and transmission coefficients for the entire structure are then determined for each polarization and wavelength as:

$$r = \frac{E_0^-}{E_0^+} = \frac{S_{21}}{S_{11}},\ t = \frac{E_{m+1}^+}{E_0^+} = \frac{1}{S_{11}} \tag{5.7}$$

The measured reflectivity R is $|r|^2$ and can be evaluated as a function of wavelength to generate a reflectivity spectrum for the structure at various angles of incidence (θ_0). As such, the angle resolved reflectivity for the organic semiconductor microcavity of interest can be simulated and compared to experimental results.

The polarization dependent EL is simulated using the optical transfer matrix model above that includes an infinitely thin source plane placed at the emission interface.[136] Source terms, based on dipole emission, are derived in Ref. 136 for both s-polarized and p-polarized emission. For the case of s-polarized emission the source terms are as follows for horizontally and vertically aligned dipoles:[136]

$$A^s_{\downarrow,\uparrow} = \pm\sqrt{\frac{3}{16\pi}} \text{ (horizontal)} \tag{5.8}$$

$$A^s_{\downarrow,\uparrow} = 0 \text{ (vertical)} \tag{5.9}$$

Analogous expressions for p-polarized emission source terms:

$$A^p_{\downarrow,\uparrow} = \pm\sqrt{\frac{3}{16\pi}}\frac{k_{z,1}}{k_1} \tag{5.10}$$

$$A^p_{\downarrow,\uparrow} = \pm\sqrt{\frac{3}{8\pi}}\frac{k_{\|}}{k_1} \text{ (vertical)} \tag{5.11}$$

The direction of emission from the source plane is denoted by the subscripts ↓ and ↑. The wavevectors indicated by k are expressed in terms of the angular frequency (ω), speed of light (c), external angle of emission (θ_{ext}), and index of refraction of the source (n_1):

$$k_1 = \frac{n_1\omega}{c},\ k_{z,1} = \frac{n_1\omega\cos(\theta_{ext})}{c}, \text{ and } k_{\|} = \frac{n_1\omega\sin(\theta_{ext})}{c} \tag{5.12}$$

The total source term for each polarization consists of a 1:1 weighted average of the square root of the power per unit solid angle of horizontally and vertically aligned dipoles:[136]

$$A^{s}_{\downarrow,\uparrow} = \pm\left[\frac{1}{2}\sqrt{\frac{3}{16\pi}}\right] \tag{5.13}$$

$$A^{p}_{\downarrow,\uparrow} = \pm\left[\frac{1}{2}\sqrt{\frac{3}{16\pi}}\frac{k_{z,1}}{k_1} + \frac{1}{2}\sqrt{\frac{3}{8\pi}}\frac{k_{\parallel}}{k_1}\right] \tag{5.14}$$

To obtain the polariton emission spectra, the source terms for each polarization must be propagated to their respective reflectors via the transfer matrix formulism as shown in Fig. 5.3. Subset transfer matrices are thus calculated from the left side reflector up to the designated source plane and from the source plane to the right side reflector. The subset transfer matrices can then be applied to obtain the following expressions for the electromagnetic field emitted from the bottom (E_B) or top of the structure (E_T):

$$\begin{bmatrix} 0 \\ E_B \end{bmatrix} = \begin{bmatrix} a_{11} & a_{12} \\ a_{21} & a_{22} \end{bmatrix}\begin{bmatrix} E^{+}_{left} \\ E^{-}_{left} \end{bmatrix}, \begin{bmatrix} E^{+}_{right} \\ E^{-}_{right} \end{bmatrix} = \begin{bmatrix} b_{11} & b_{12} \\ b_{21} & b_{22} \end{bmatrix}\begin{bmatrix} E_T \\ 0 \end{bmatrix} \tag{5.11}$$

E_{left} (E_{right}) is the electromagnetic field emitted from the left (right) of the source plane. The superscripts "+" and "-" designate right and left traveling electromagnetic fields (Fig. 1.2), respectively. The subset transfer matrices in Eqn. 5.11 are written in terms of their matrix elements "a" (left side reflector to source plane) and "b" (source plane to right side reflector). The source terms in Eqns. 5.7 and 5.8 can be used to determine E_{left} and E_{right} as follows:

$$\begin{bmatrix} E^{+}_{right} \\ E^{-}_{right} \end{bmatrix} - \begin{bmatrix} E^{+}_{left} \\ E^{-}_{left} \end{bmatrix} = \begin{bmatrix} A_{\uparrow} \\ A_{\downarrow} \end{bmatrix} \tag{5.12}$$

The system of equations established between Eqns. 5.11 and 5.12 permits the emitted electromagnetic intensity (E_B and E_T) from the structure to be calculated.[136] The MATLAB code used to generate the transfer matrix simulations of reflectivity, luminescence and confined electromagnetic field is shown in Appendix B.

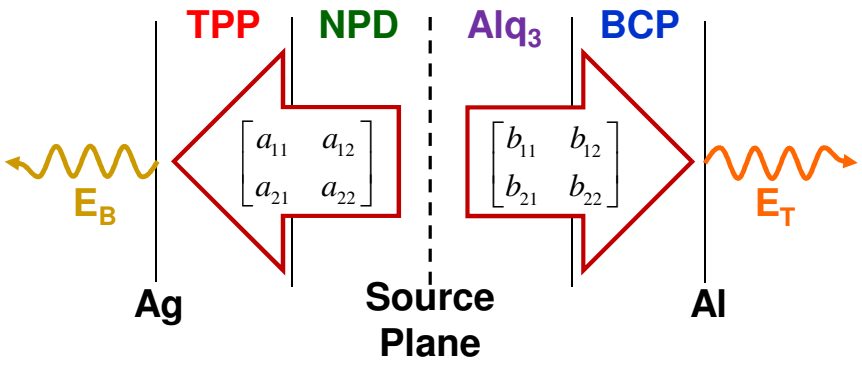

Figure 5.3 Schematic representation of an optical transfer matrix simulation of EL. Source terms at the emission interface (NPD/Alq_3) interface are propagated by subset transfer matrices (arrows) out of the device resulting in emission from the top (Al, E_T) and bottom (Ag, E_B) reflectors.

5.3 Experiment

The device fabrication procedure is similar to those outlined in Chapters 3 and 4. Here, the microcavity organic light-emitting device consists of a 50-nm-thick Ag anode, a 65-nm-thick layer of tetraphenylporphyrin (TPP), a 10-nm-thick layer of the hole-transporting material N,N'-bis(naphthalene-1-yl)-N,N'-bis(phenyl)-benzidine (NPD), a 70-nm-thick layer of the electron-transporting material aluminum tris(8-hydroxyquinoline) (Alq_3), and a 10-nm-thick layer of the exciton/hole-blocking material bathocuproine (BCP). The device structure (Fig. 5.4) is capped with a 0.5-nm-thick layer of LiF and a 50-nm-thick layer of Al which serves as the device cathode. Again, the

metallic anode (Ag) and cathode (Al) serve as reflectors forming the optical microcavity (Fig. 5.4).[127,172] The use of the radiative pumping structure presented in Chapter 4 permits the uniform population of both the upper and lower polariton branches. As such, the effect of light polarization on the dispersion of both upper and lower polariton branches can be investigated. Microcavities were characterized using polarization dependent angle-resolved reflectivity and EL. Reflectivity measurements were performed using a variable-angle spectroscopic ellipsometer to illuminate the sample with monochromatic p- or s-polarized light. The polarization state of light is determined by the orientation of the electric field component of the electromagnetic wave relative to the plane of incidence. P-polarized or s-polarized light refers to an electric field component which is parallel or perpendicular to the plane of incidence, respectively. P- and s- polarized electroluminescence spectra were collected from devices excited at 100 mA/cm^2 by placing a polarizer between the sample and detector using a manual goniometer.

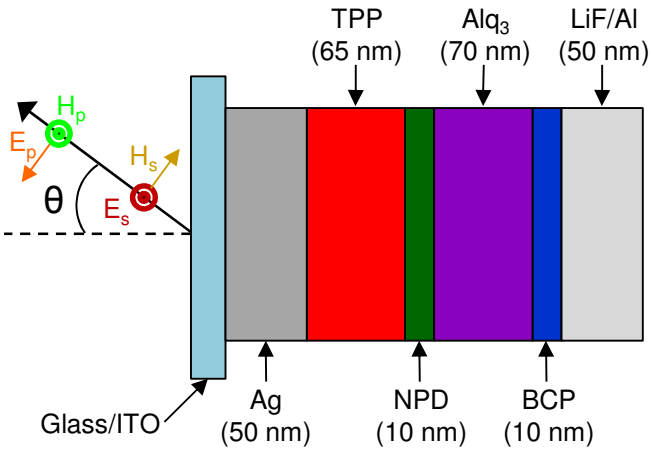

Figure 5.4 Microcavity device architecture discussed in the text. The electric and magnetic field components of the electromagnetic wave are denoted by either E or H with subscripts p or s indicating p- or s-polarized light, respectively. The electric field component of the electromagnetic wave is parallel (perpendicular) to the plane of incidence for p-polarized (s-polarized) light.

5.4 Results and Discussion

Figure 5.5a shows p- and s-polarized angle-resolved reflectivity spectra for the microcavity structure of Fig. 5.4. For both polarizations, two features showing strong dispersion with angle are observed as a result of the strong coupling between the cavity photon and the excitonic resonance of TPP at 1.90 eV.[130,191] The corresponding dispersion relations are shown in Fig. 5.5b, and are constructed by multi-peak fitting (Lorentzian) the reflectivity spectra. At low angle, the p- and s-polarized dispersion curves are similar, while at high angle, a clear divergence is observed reflecting a large polarization splitting. The dispersion curves were modeled using an optical transfer matrix formalism to simulate angle-resolved reflectivity spectra under p- and s-polarized

illumination.[120] Simulated reflectivity spectra were also multi-peak fit to extract a dispersion relation for each polarization (Fig. 5.5b). Excellent agreement is obtained between the measured and simulated dispersion curves.

Figure 5.5c shows the polarization splitting obtained by subtracting the p- and s-polarized dispersion relations of Fig. 5.5b for each polariton branch. The s-polarized uncoupled cavity photon mode has a steeper dispersion than the p-polarized case, and hence, the energetic separation between the uncoupled cavity modes becomes larger with increasing angle of incidence. At low angles, the polarization splitting of the lower branch reflects the energetic difference between the s- and p-polarized cavity photon modes with increasing angle. Since the excitonic transition energy is independent of polarization, the lower polariton branch in each case approaches the same energy at high angle, leading to a reduction in the polarization splitting (Fig. 5.5c). In contrast, the behavior of the upper branch at large angle reflects the uncoupled cavity mode dispersion, and the corresponding polarization splitting increases continuously with angle. A maximum polarization splitting of ~30 meV is achieved for both the lower and upper branch at angles of 60° and 75°, respectively. The observed dependence of the polarization splitting on angle is well-simulated using an optical transfer matrix simulation (Fig. 5.5c).

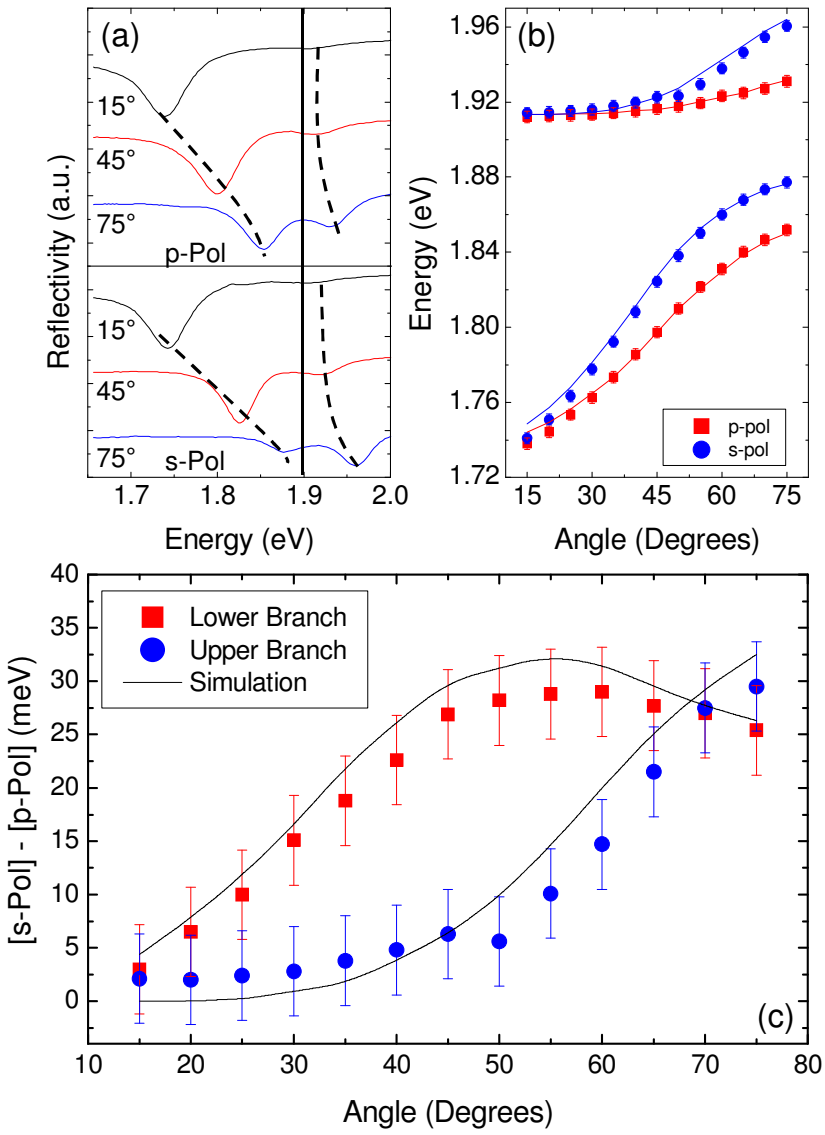

Figure 5.5 (a) Angle-resolved reflectivity spectra and (b) corresponding dispersion relations collected under p- and s-polarized illumination of the structure in Fig. 5.4. (c) Polarization splitting (symbols) for the upper and lower branches. Solid lines in parts (b) and (c) are the simulated dispersion curve and polarization splitting, respectively.

The mechanism for the observed polarization splitting in the metal-metal architecture differs from that of DBR-based microcavities where the optical penetration depth varies with light polarization.[185,187] In a metal-metal microcavity, optical penetration into the metal mirrors is exceedingly small, and the polarization splitting is instead a consequence of the polarization-dependent phase shift for the optical field upon reflection from the metal mirrors. Ultimately, this leads to a polarization-dependent cavity photon dispersion, and distinct polariton dispersions.[192,193] The polarization splittings observed here for metal-metal systems are comparable to those obtained for strongly coupled microcavities utilizing DBRs.[185] For instance, for a DBR-DBR system containing a J-aggregate active layer, the maximum observed polarization splitting for the lower and upper branch is 10 meV and 35 meV, respectively.[185]

The microcavity architecture of Fig. 5.4 was also examined under electrical excitation with angle-resolved EL collected through either a p- (Fig. 5.6a) or s-polarizer (Fig. 5.6b). As in reflectivity, two emission features exhibiting strong dispersion are observed for both polarizations as a result of strong coupling. Since radiative pumping is used to excite the polariton features, the upper and lower branch emission intensities are consistent with the branch photon character.[194] Additional emission observed at high energy (>2.05 eV) is attributed to uncoupled EL from Alq_3.[194] At normal incidence, the emission spectra for each polarization are indistinguishable since the energetic position of the cavity mode (and hence polariton mode) at 0° is independent of polarization. Consistent with measurements of reflectivity, the EL polarization splitting increases with the angle of detection for both polariton branches. The simulated EL spectra are shown

in Figs. 5.6a and 5.6b for each polarization and angle of detection. Excellent agreement is observed between the experimental and simulated spectra with the simulation correctly predicting the relative intensity, spectral position and linewidth of each polariton feature.

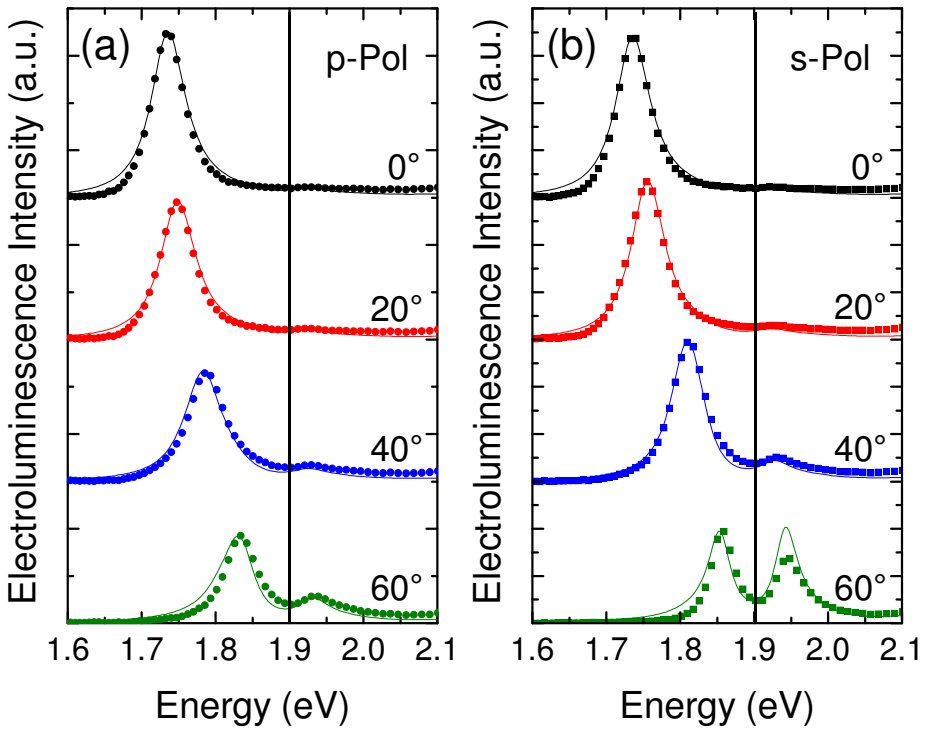

Figure 5.6 Measured (symbols) and simulated (solid lines) p- (a) and s-polarized (b) angle-resolved electroluminescence (EL) spectra for the device in Fig. 5.4. The vertical solid line denotes the position of the uncoupled excitonic resonance.

In order to extract the polarization splitting under electrical excitation, the measured EL spectra of Fig. 5.6 were multi-peak fit to construct a corresponding dispersion curve for each polarization (Fig. 5.7a). The polarization splitting shown in Fig. 5.7b for each branch was determined by subtracting the dispersion curves in Fig.

5.7a. As in reflectivity, the EL polarization splitting for the lower branch is a peaked function while the splitting for the upper branch increases with angle. The simulated dispersion relation (Fig. 5.7a, solid lines) and polarization splitting for each branch (Fig. 5.7b, solid lines) were obtained using the same method described for the analysis of microcavity reflectivity measurements. Good agreement is obtained between the experimental and simulated polarization splitting shown in Fig. 5.7b for each branch.

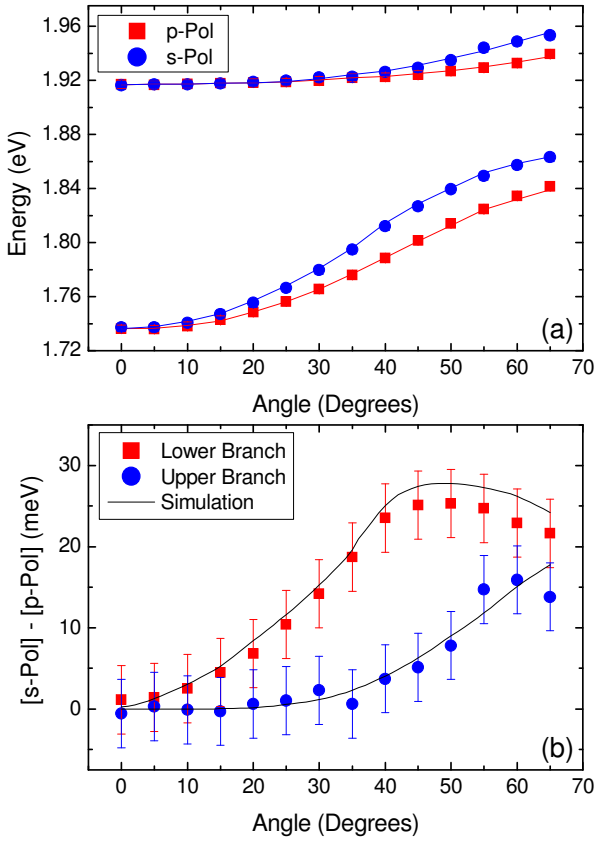

Figure 5.7 (a) Dispersion relations (symbols) determined from the p- and s-polarized electroluminescence spectra of Figs. 5.6a and 5.6b, respectively. (b) The polarization splitting (symbols) obtained from the dispersion relations in (a). Solid lines are simulations obtained using the optical transfer matrix model of Fig. 5.3.

5.5 Summary

In conclusion, a strongly coupled metal-metal organic microcavity is shown to exhibit a significant polarization splitting in both reflectivity and EL. The observed polarization splitting is a consequence of the polarization-dependent phase shift of the optical field upon reflection from the metal mirrors. This case represents an interesting contrast to DBR-based microcavities where the polarization splitting is due to the large, polarization-dependent, optical field penetration depth of the DBR. The use of metal-metal microcavities has become common for the study of organic semiconductors in the regimes of both strong and weak exciton-photon coupling,[192,193] as well as in many plasmonic structures.[195-197] Consequently, it is essential to fully quantify the presence of these effects as they play a substantial role in determining device emission characteristics.

Chapter 6 Long-range, photon-mediated exciton hybridization in all-organic photonic crystals

6.1 Introduction

Extensive attention has been devoted to the study of semiconductors embedded in optical nanostructures that confine the electromagnetic field and enhance the light-matter interaction.[66,96-99,107,137,198-201] Frequently, the regime of strong coupling is accessed by placing the absorbing semiconductor active layer at the antinodes of the confined electromagnetic field in an optical microcavity as is the case in Chapters 3-5.[76,99] Comparable exciton-photon interactions, however, have also been demonstrated in one-dimensional (1D) photonic crystals.[202-204] These structures are fabricated by periodically arranging the active layers for strong coupling in a uniform non-absorbing material or background dielectric.[205] The periodicity of the active coupling layers is an integer multiple of half the desired resonant photon wavelength.[205] Multiple reflections at the dielectric-active layer interfaces (due to the refractive index difference between the dielectric material and the active material) add constructively to establish the photon modes (or Bragg modes) of the system (Fig. 6.1).[206] A large index contrast between the dielectric and active layers is critical in realizing spectrally narrow photon modes and a resolvable exciton-photon coupling.[204]

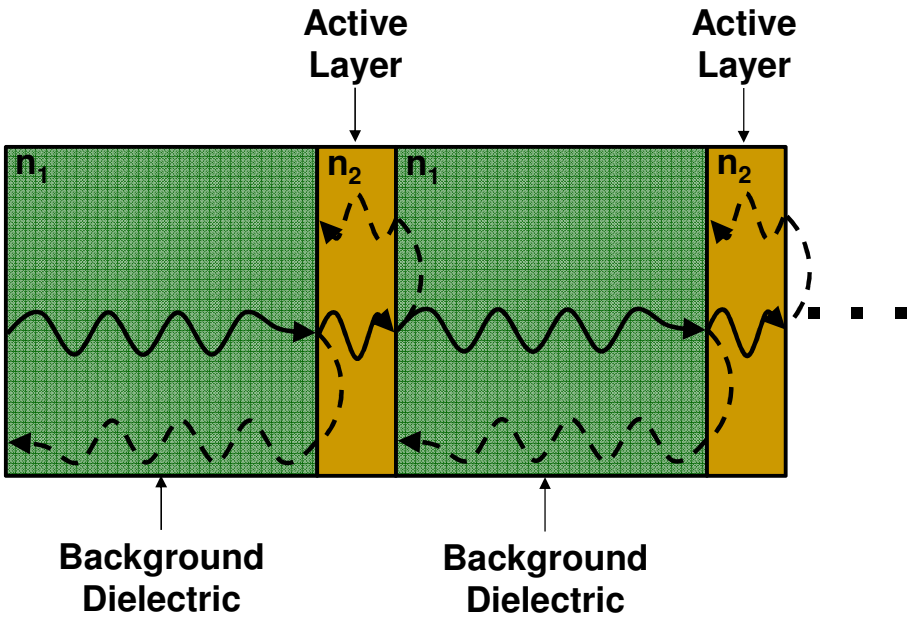

Figure 6.1 An illustration of a 1D photonic crystal consisting of an active layer dispersed in a background dielectric. The thicknesses of the layers are chosen such that reflections at the interfaces (due to large index contrast) between the two materials add constructively to establish the photon modes of the system.

Various active coupling layers including inorganic semiconductors and layered perovskites have been used to observe strong exciton-photon coupling in 1D photonic crystals.[202-204,207] The regime of strong coupling has also been observed in two-dimensional photonic crystals with semiconductor quantum dots used as the absorbing active material.[208,209] Most systems of this type, however, do not contain multiple absorbers, and often use a single quantum dot as the active coupling material. The first demonstration of strong exciton-photon coupling in a bulk semiconductor structure was observed recently by Goldberg et al.[203] The structure consisted of 70 periods of two GaAs quantum well active layers spaced in the larger band gap, lower refractive index background semiconductor $Al_{0.22}Ga_{0.78}As$. Strong exciton-photon coupling is observed between a photon mode of the structure and the light-hole and heavy-hole excitons of the

GaAs quantum wells as a result of the refractive index difference for the structure of 0.22 (Fig. 6.2).

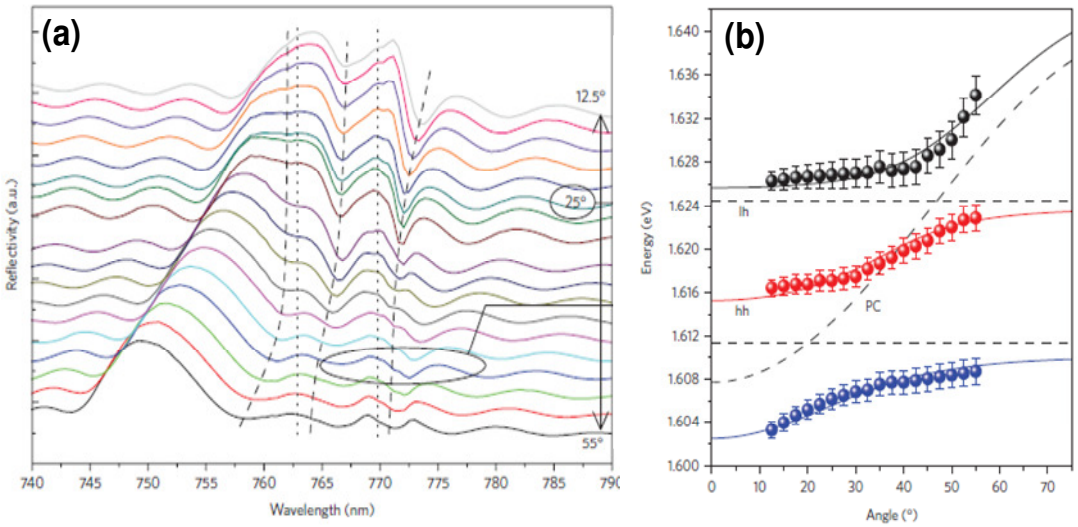

Figure 6.2 (a) Angle-resolved reflectivity spectra for a 70 period 1D photonic crystal consisting of two GaAs quantum wells distributed in a larger bandgap, lower refractive index semiconductor $Al_{0.22}Ga_{0.78}As$. Strong exciton-photon coupling is observed between a photon mode of the photonic crystal and the light-hole and heavy-hole excitons of GaAs. (b) The three branch dispersion relation for the angle resolved reflectivity spectra of (a).[203]

Following this preliminary demonstration of strong coupling, polariton amplification was realized in a 1D photonic crystal containing quantum wells of InGaAs as the active absorbing layers.[204] The large index difference between the InGaAs quantum wells and background semiconductor GaAs permit spectrally narrow photon modes and markedly more well resolved polariton features (Fig. 6.3a and 6.3b). Polariton amplification was demonstrated in this structure by ultrafast pump-probe spectroscopy, pumping the structure at the magic angle (discussed in Sec. 2.4.2) and measuring a peak gain of 6.4 in the probe pulse as exhibited by Fig. 6.3c and 6.3d.[204] This result is particularly exciting given the uniqueness of the 1D photonic crystal architecture and the potential ability of these structures to exhibit non-linear phenomena

such as lasing, and stimulated scattering. Organic semiconductors, given their advantageous exciton properties (as discussed in Sec. 2.4.6), could be incorporated into 1D photonic crystal structures providing new directions of investigation of organic exciton-photon coupling and potentially an alternate route to organic polariton amplification.

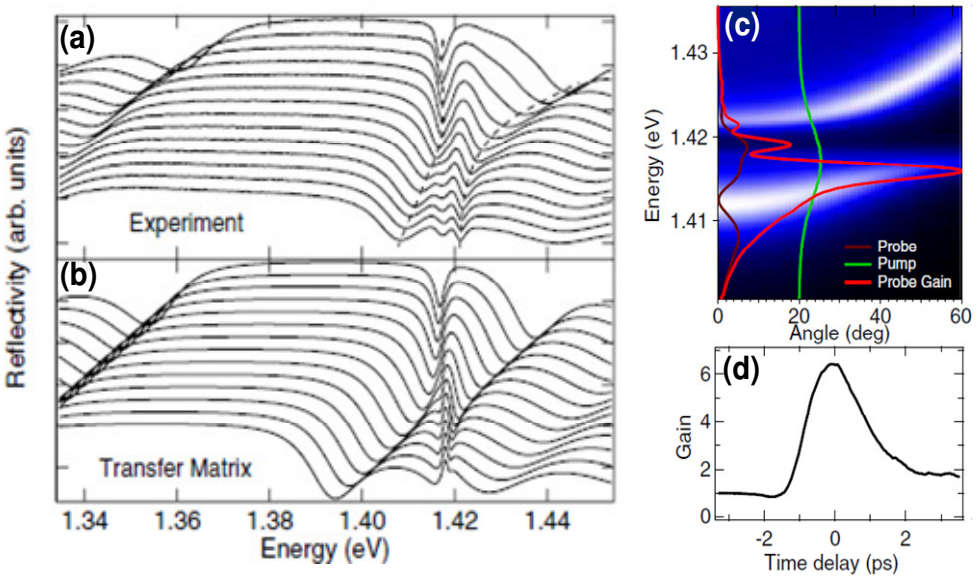

Figure 6.3 Experimental (a) and simulated (b) angle-resolved reflectivity of a 1D photonic crystal architecture consisting of 30 periods of InGaAs quantum wells in a background GaAs semiconductor. The large index contrast of this structure results in spectrally narrow polariton modes in the reflectivity spectra. (c) Ultrafast pump-probe spectroscopy measurement results of the InGaAs based 1D photonic crystal structure. The probe pulse exhibits strong amplification and a peak gain of 6.4 (d).

In this Chapter, an all-organic semiconductor 1D photonic crystal exhibits strong exciton-photon coupling between multiple layers of the active material tetraphenylporphyrin (TPP) spaced in a uniform dielectric background. The large exciton binding energy and absorption coefficient of TPP (Fig. 6.4) enables the observation of strong coupling in measurements of room temperature reflectivity with a Rabi splitting of

(75 ± 7) meV.[30,123] While previous work on all-inorganic 1D photonic crystals has also led to the observation of strong exciton-photon coupling, these studies have not investigated the crucial question of long-range coupling between individual active layers in the structure. Here, by including a second organic semiconductor active material, octaethylporphyrin (OEP, Fig. 6.4), in the photonic crystal, we demonstrate long-range, photon-mediated coupling between two different organic semiconductors. The resulting hybridization between the resonant photon mode of the photonic crystal and the two excitonic species (TPP and OEP) is studied as a function of the spatial position of the two absorbing active layers in the photonic crystal.[164]

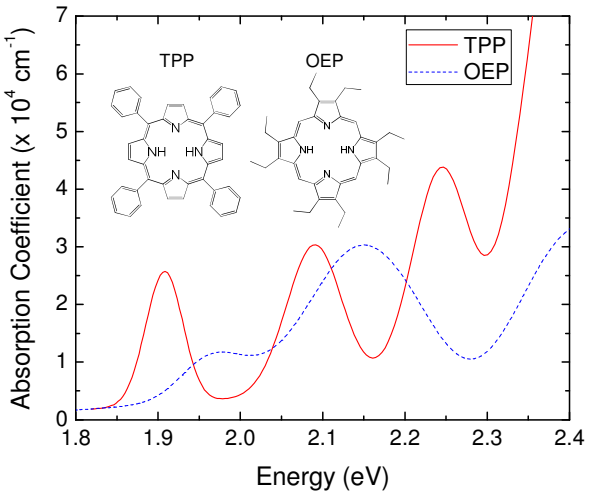

Figure 6.4 The absorption coefficient for 70-nm-thick films of TPP and OEP on glass substrates. Inset are the molecular structures of TPP and OEP.

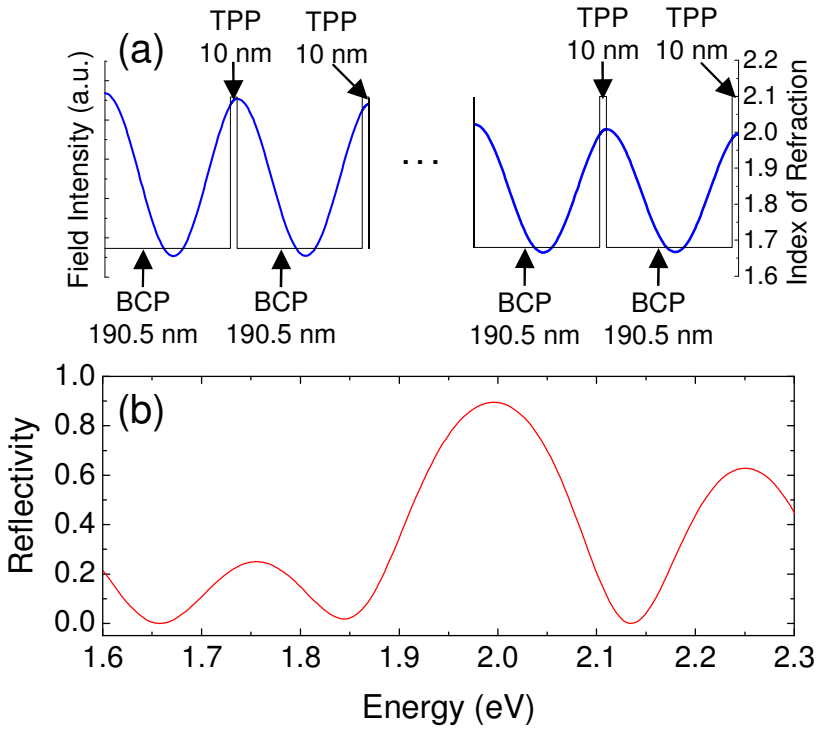

Figure 6.5 (a) One-dimensional photonic crystal discussed in the text for a structure containing eight periods of: 190.5 nm of BCP and 10 nm of TPP. The solid line overlaid over the index of refraction profile is the optical field intensity simulated using a transfer matrix formalism at strongest coupling, corresponding to an angle of incidence of 27.5° and photon wavelength of λ = 650 nm (1.91 eV). (b) Reflectivity spectrum at an angle of incidence of 15° simulated via an optical transfer matrix formalism for the structure of Fig. 1b with a static index of refraction n=2.1 and an extinction coefficient k=0 for TPP.

6.2 Experiment

One-dimensional photonic crystals were constructed by depositing organic thin films onto glass substrates using vacuum thermal sublimation at a pressure of 8×10^{-7} Torr. Prior to layer deposition, substrates were degreased with solvents. For 1D photonic crystals containing only a single absorbing active material, the structure consisted of 8 periods of a 190.5-nm-thick layer of the background dielectric material bathocuproine (BCP) and a 10-nm-thick layer of the active material TPP.[41,130,191] The layer sequence

and index of refraction profile for this structure is shown in Fig. 6.5a. A transfer matrix formalism was employed to simulate the optical field and confirm that the active layers are placed at the antinodes of the confined field in the structure (Fig. 6.5a).[120] The wide energy-gap material BCP was chosen as the background dielectric material in all structures in order to prevent parasitic absorption at the energies of interest for strong coupling. Reflectivity measurements were performed using a variable-angle spectroscopic ellipsometer with s-polarized light illumination to characterize the 1D photonic crystals.

In order to characterize the stop band of the 1D photonic crystal, reflectivity spectra were simulated using an optical transfer matrix formalism with a static index of refraction n=2.1 and an extinction coefficient k=0 for TPP (shown in Fig. 6.5b). The structure exhibits a 0.27 eV wide photonic band gap centered at ~2.0 eV with Q=17 corresponding to a photon Bragg mode linewidth of 68 meV (at FWHM). A single, 10-nm-thick active layer of TPP embedded within a photonic crystal was confirmed via optical transfer matrix simulations to not be sufficiently absorptive to reach the regime of strong coupling. Hence, the observation of a splitting using the structure shown in Fig. 1b would already suggest that the coupling occurs amongst multiple active layers and is thus long-range.

6.3 Theory

The coupled oscillator model (Eqn. 2.34) can be extended to account for photon-mediated coupling (hybridization) between two different excitonic resonances (TPP and

OEP). The system Hamiltonian is expanded to a 3x3 matrix with the additional exciton energy of OEP (E_{OEP}) added in the main diagonal of the matrix as follows:

$$\begin{bmatrix} E_{ph} & V_{TPP} & V_{OEP} \\ V_{TPP} & E_{TPP} & 0 \\ V_{OEP} & 0 & E_{OEP} \end{bmatrix} \begin{bmatrix} \alpha \\ \beta \\ \gamma \end{bmatrix} = E \begin{bmatrix} \alpha \\ \beta \\ \gamma \end{bmatrix} \tag{6.1}$$

The photon-exciton interaction terms for the TPP and OEP excitons are denoted by V_{TPP} and V_{OEP} while α, β, and γ designate the photon, TPP exciton and OEP exciton mixing coefficients of the polariton, respectively. The photon energy and TPP exciton energy are denoted by E_{ph} and E_{TPP}, respectively. The photon energy (E_{ph}) can be extracted by fitting the dispersion relation with a transfer matrix model whereas the interaction terms are determined as the minimum energetic separation between the middle and lower branches (V_{TPP}), and the upper and middle branches (V_{OEP}), respectively. The exciton energies of TPP and OEP are extracted from the absorption spectra of Fig. 6.4 and the polariton energies (E) are extracted from the dispersion relation. Finally, Eqn. 6.1 can be utilized to extract the degree of hybridization of each polariton branch by calculating α^2, β^2, and γ^2 for all angles of incidence. In the hybridized 1D photonic crystal structure, the middle branch should exhibit significant mixing between the photon mode of the photonic crystal and both excitons.

6.4 Results and Discussion

The photonic crystal of Fig. 6.5a was tuned to overlap with the excitonic transition of TPP at 1.908 eV (Fig. 6.4). Angle-resolved reflectivity spectra for the 1D photonic crystal of Fig. 6.5a are shown in Fig. 6.6a. Two spectral features clearly anti-

cross around the uncoupled excitonic resonance of TPP, indicating strong coupling between an optical mode of the photonic crystal and the excitonic transition. A third feature observed at high energy (>2.05 eV) results from the hybridization of the resonant photon mode with both the 1.908 eV and 2.091 eV excitonic resonances of TPP. The additional feature observed at low energy (<1.85 eV) is a lower order photon mode of the photonic crystal.

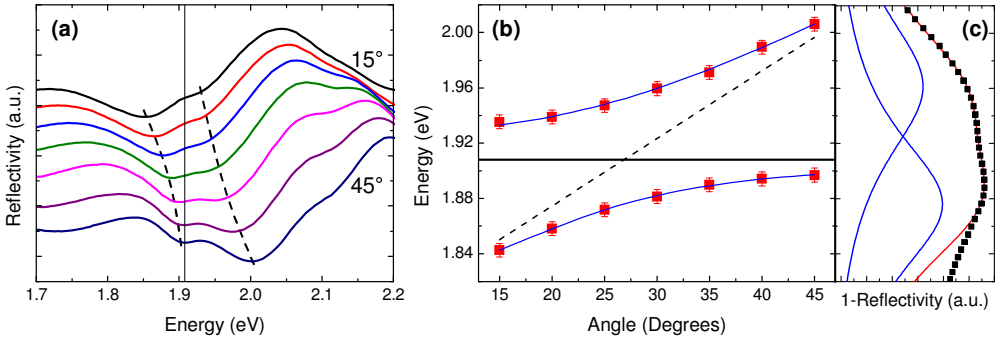

Figure 6.6 (a) Angle-resolved reflectivity spectra and the corresponding dispersion relation (b) collected under s-polarized light illumination for the structure in Fig. 1b. In part (a) the vertical solid line denotes the uncoupled exciton resonance of interest while the broken lines indicate the position of the strongly coupled features. In part (b), the horizontal solid line designates the uncoupled exciton resonance, the broken line is the simulated uncoupled photon dispersion and the solid lines are dispersion curves obtained from a damped two-branch coupled oscillator model. (c) Multi-peak fitting for the reflectivity spectrum of Fig. 2a collected at an angle of incidence of 30°. The spectrum is deconvoluted by multi-peak fitting with two Lorentzian peaks representing the lower and upper polariton branches.

The reflectivity spectra of Fig. 6.6a were multi-peak fit to construct a dispersion relation for the exciton-polariton resonances (Fig. 6.6b). Figure 6.6c shows an example of peak deconvolution for a reflectivity spectrum collected at an angle of incidence of 40° for the structure of Fig. 1b. The experimental dispersion curve is in good agreement with a damped two-branch coupled oscillator model (Fig. 6.6b, solid lines) with fixed

parameters that are separately determined. A Rabi splitting of (75 ± 7) meV was calculated as the minimum energetic separation between the upper and lower branches. The photon dispersion (Fig. 6.6b) and linewidth (FWHM = 72 meV) of the photonic crystal of interest were determined via an optical transfer matrix formalism with no free parameters as all layer thicknesses and optical constants for the organic materials were separately measured. The TPP exciton linewidth (FWHM = 69 meV) and energy (1.908 eV) were determined from the absorption spectrum of Fig. 6.4.

For the hybridized structure that contains two absorbing species (Fig. 6.7), the layer stack consisted of 4 periods of a 160.5-nm-thick layer of BCP and a 20-nm-thick layer of TPP, followed by 4 periods of a 90.5-nm-thick layer of BCP and a 80-nm-thick layer of OEP. In this structure, both TPP and OEP serve as the active layers for strong coupling. Transfer matrix simulations were again used to ensure maximum overlap between the optical field and each of the active layers (Fig. 6.7).[120] The absorption coefficient of OEP is roughly a factor of two smaller than that of TPP (Fig. 6.4). Since the Rabi splitting in strongly coupled organic semiconductor microcavities increases with active layer absorption,[123] the total layer thickness of OEP in the structure is made considerably thicker than that of TPP in order to realize a comparable exciton-photon interaction. By including a second active material, multiple excitonic transitions in the photonic crystal are hybridized via their common interaction with the resonant photon mode. The periods containing TPP and the periods containing OEP are located at opposite ends of the structure of Fig. 6.7. Since the optical excitation is through the periods containing TPP, this arrangement permits the spatial extent of strong coupling to

be studied as coupling to OEP will only occur if substantial optical field intensity is present throughout the structure.

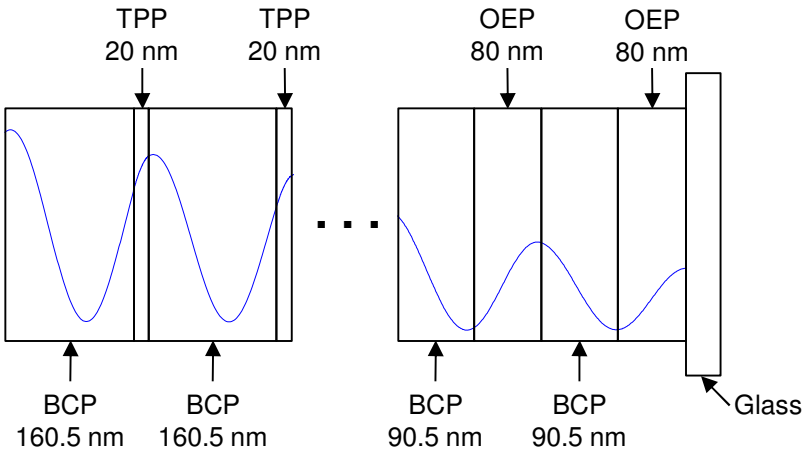

Figure 6.7 One-dimensional photonic crystal used to examine photon-mediated exciton hybridization. The structure consists of 4 periods of 160.5 nm BCP/20 nm TPP followed by 4 periods of 90.5 nm BCP/80 nm OEP. The solid line is an optical field intensity profile simulated using a transfer matrix formalism at the point of strongest mixing between the OEP and TPP excitons and photon mode corresponding to an angle of incidence of 70° and a photon wavelength of λ = 642 nm (1.93 eV).

Figure 6.8a shows angle-resolved reflectivity for the photonic crystal of Fig. 6.7 which contains two active materials, namely, TPP and OEP. Three prominent features, particularly at an angle of 70°, are observed due to the photon-mediated hybridization of the excitonic transitions of TPP at 1.908 eV and that of OEP at 1.958 eV with the optical mode of the photonic crystal. The two additional spectral features observed at high energy (>2.05 eV) are attributed to a coupling between a higher order mode of the photonic crystal and the TPP excitonic resonance at 2.09 eV while the additional spectral feature observed at low (<1.85 eV) energy is a lower-order photon mode of the photonic crystal. Multi-peak fitting was performed on the reflectivity spectra to extract the position of each feature and construct a dispersion curve (Fig. 6.8b). Branch splittings of

(40 ± 7) meV and (41 ± 7) meV are determined as the minimum energetic separation between the middle and lower branches (TPP exciton), and the upper and middle branches (OEP exciton), respectively. As in the case of the photonic crystal of Fig. 6.5a, an optical transfer matrix formalism was utilized to determine the photon dispersion and linewidth (FWHM = 39 meV) of the photonic crystal. The aforementioned parameters and exciton linewidths of TPP (FWHM = 69 meV) and OEP (FWHM = 70 meV) as determined from Fig. 6.4 were set as fixed parameters in a damped three-branch coupled oscillator model. Good agreement is obtained in Fig. 3c between the experimental (symbols) and damped three-branch coupled oscillator model (solid lines) dispersions for each branch.

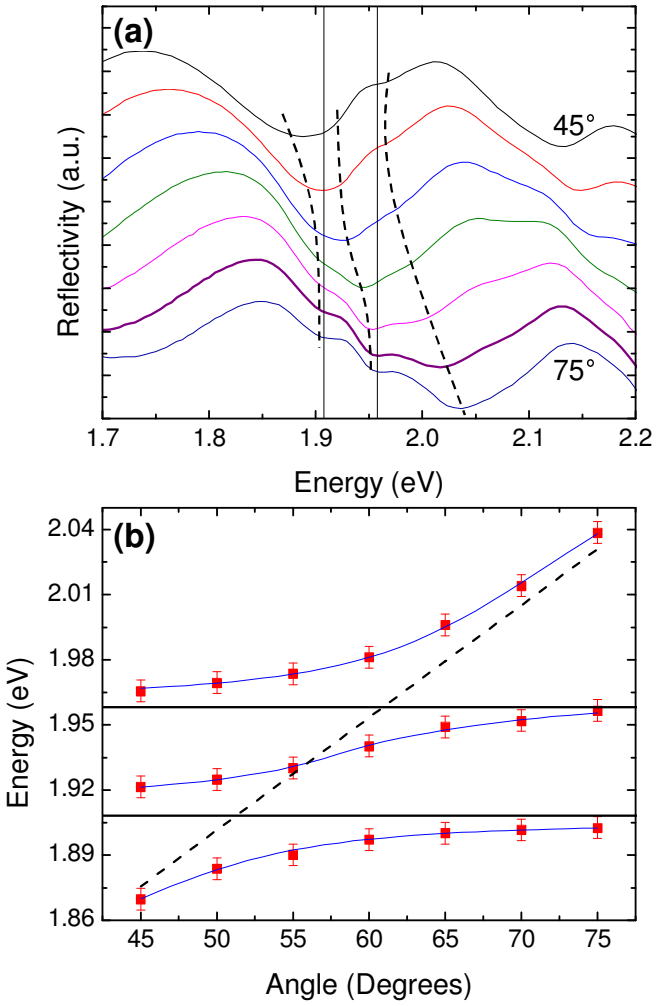

Figure 6.8 (a) Angle-resolved reflectivity spectra collected under s-polarized light illumination and (b) the corresponding dispersion relation. In (a), the reflectivity spectrum collected at angle of 70° (bold) exhibits three clear features confirming photon-mediated hybridization between the excitons of TPP and OEP and the photon mode. The vertical solid lines denote the uncoupled exciton resonances of interest while the broken lines indicate the position of the strongly coupled features. In (b), the solid horizontal lines denote the position of the uncoupled exciton resonances, the broken line is a simulated uncoupled photon dispersion curve and the solid lines are dispersion curves obtained from a damped three-branch coupled oscillator model.

Figure 6.9 shows the mixing coefficients extracted from the three-body coupled oscillator model of Eqn. 6.1 plotted versus angle for each branch of the dispersion relation in Fig. 6.8b.[204] The lower polariton branch exhibits symmetrically varying degrees of photon and TPP exciton character. The middle polariton branch demonstrates significant mixing between the photon, the TPP exciton and the OEP exciton. Maximum mixing occurs at an angle of ~55°, where the middle branch polariton character is equal parts TPP and OEP exciton (~42%) and ~16% photon. Consistent with previous reports of photon-mediated hybridization, the large branch splittings lead to a gradual middle branch dispersion with angle and a small photon contribution to the overall character of the middle branch.[164] The upper branch consists mainly of OEP exciton and photon character with some mixing of the TPP exciton occurring at large angles. The presence of hybrid exciton-polariton states in the structure confirms that long-range strong coupling is present as the resonant photon mode clearly samples the entire structure.

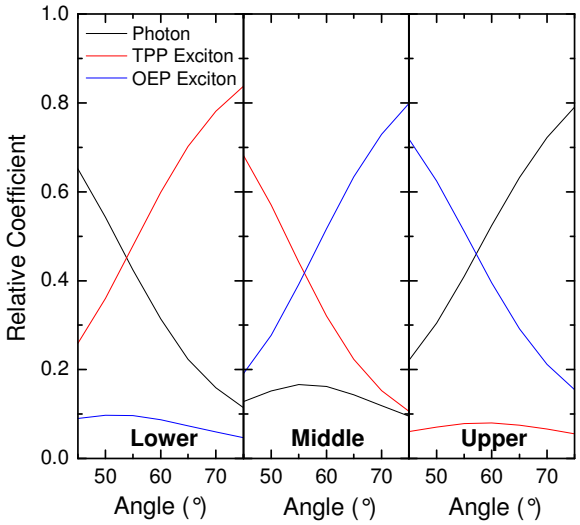

Figure 6.9 Mixing coefficients extracted from the dispersion relation of Fig. 6.8b. The middle branch demonstrates the most significant mixing between the TPP and OEP excitons and the photon mode of interest.

As previously noted in Chapter 2, the regime of strong exciton-photon coupling is reached when the respective transition linewidths of the exciton and photon are smaller than the characteristic Rabi splitting of the system. Here, the Rabi splittings observed in the structures of Fig. 1b and Fig. 3a are actually comparable to the respective exciton and photon linewidths. Interestingly, broad exciton transition linewidths are frequently observed in disordered organic semiconductors, and have been previously discussed in the context of polariton coherence. Work by Agranovich et al.[110] has proposed that depending on their energy and in-plane wavevector, polaritons in such systems could exhibit either coherent or incoherent behavior. In particular, states at large (small) wavevector in the lower (upper) branch would be incoherent for uncoupled excitonic

transition linewidths that rival the Rabi splitting. In this work, a closer examination of polariton coherence, could reveal a similar behavior.

6.5 Summary

An all-organic 1D photonic crystal was demonstrated that permits the observation of strong exciton-photon coupling at room temperature with Rabi splittings that are an order of magnitude larger than in inorganic analogs.[203] The long-range character of the coupling is confirmed through the observation of photon-mediated exciton hybridization between two different absorbers that are spatially separated in the structure. While in this work the separation between absorbers is 90.5 nm, the extended nature of the photon mode will permit hybridization to be observed over considerably larger distances as well. The unique attributes of 1D all-organic photonic crystals tuned to the regime of strong exciton-photon coupling make this an interesting platform for the examination of energy transfer between spatially separated excited states. Additionally, these structures could offer new opportunities for the development of polariton-based optoelectronic devices.

Chapter 7 Electrical excitation of inorganic microcavity polaritons by radiative pumping from a weakly coupled organic semiconductor

7.1 Introduction

This thesis has focused primarily on understanding and exploiting polariton excitation mechanisms in microcavities containing highly disordered or amorphous organic semiconductors. The work presented is extremely useful for understanding the fundamentals of organic optical microcavities in the regime of strong exciton-photon coupling but does not directly address the ultimate goal of an electrically injected polariton laser. To date, the main roadblock to an organic polariton laser is that, in general, electrical or optical excitation of these materials results in the creation of localized excited states.[110,181,210] The localization occurs as a result of the disorder-induced inhomogeneous broadening of the excitonic transition and the absence of intermolecular interaction.[71,100,110,181,210] In the strong exciton-photon coupling regime, incoherent excitations result in the creation of incoherent polaritons unable to undergo non-linear scattering processes as discussed in Sec. 2.4.1.[100,110,210] One exception is the case of highly ordered or crystalline organic microcavities which should, in principle, exhibit improved intermolecular interaction leading to larger fractions of coherent excitations and potentially enhanced non-linear properties such as polariton scattering in the regime of strong exciton-photon coupling.[71,166,167,211-215] Indeed, polariton lasing was

recently demonstrated in a single crystal anthracene optical microcavity but was realized through direct radiative scattering rather than polariton parametric processes (Sec. 2.4.4).[71] As such, it is unclear whether non-linear polariton parametric scattering processes in organic semiconductor microcavities are feasible.[122,216]

Various inorganic semiconductors confined to optical microcavities tuned to the strong exciton-photon coupling regime, however, have demonstrated non-linear polariton parametric scattering processes.[116,137,138,140-144,147,149,150,153,155-158,217] A major drawback to inorganic semiconductors is the inherent weak exciton binding energy rendering room temperature operation of inorganic polariton based optoelectronic devices difficult.[218,219] The exceptions are ZnO and GaN which have stable exciton states at room temperature.[49,141,146,161,220-231] Despite the enhanced exciton binding energy of these materials, electrical excitation of polaritons at room temperature has yet to be demonstrated most likely due to increased exciton dissociation probability with current injection.[139,159] To circumvent this problem, the radiative pumping utility described in Chapter 4 could facilitate electrical excitation of inorganic polariton states while eliminating charge transport in the active coupling layer. The advantages of such a device are two-fold: the inorganic exciton is not perturbed by electrical pumping since no charge transport occurs in the inorganic active layer, and the broad luminescence spectra of the organic semiconductor provides efficient radiative pumping of inorganic polariton states in the regime of strong exciton-photon coupling. In this case, the non-linear polariton parametric scattering processes of strongly coupled inorganic polaritons could be exploited under electrical excitation at room temperature.

The objective of this chapter is to demonstrate strong coupling and radiative pumping of inorganic polariton states in a hybrid organic/inorganic device. Here, a device is designed with an active coupling layer of ZnO which is electrically excited by radiative pumping from the weakly coupled organic semiconductor 2-(9,9-spirobifluoren-2-yl)-9,9-spirobifluorene (BSBF).[221,226-230,232-236] The device is characterized under angle-resolved reflectivity and electroluminescence (EL) to demonstrate the utility of radiative pumping in these structures. The work developed here, may ultimately provide a platform through which to develop a room temperature polariton-based coherent emitter under electrical excitation. This chapter is organized as follows: In Sec. 7.2, the experimental details including the device structures and fabrication are described. The experimental results and analysis are presented in Sec. 7.3 and summarized in Sec. 7.4.

7.2 Experiment

Two different microcavities containing either ZnO or ZnO and organic layers (hybrid device) were explored to facilitate the analysis of the hybrid organic/inorganic device. In both structures, ZnO was grown by atomic layer deposition (ALD) at a temperature of 200° C yielding a growth rate of 1.67 Å/loop.[237-241] Each loop consisted of successive pulses of 15 ms of the precursor gases diethylzinc and water vapor followed by a 5 s nitrogen purge between each pulse. Two extra 15 ms water vapor pulses were added at the end of the growth procedure to passivate any unbonded Zn atoms. In both structures, all device layers other than ZnO were deposited using thermal sublimation at a pressure of ~8×10^{-7} Torr. For measurements of microcavities containing only ZnO, a

{100} Si wafer (intrinsic) was used as the substrate. The microcavity consisted of a 100-nm-thick layer of Al, a ZnO layer of varying thickness, and a 25-nm-thick layer of Al (Fig. 7.1a). Here, light is collected through the semi-transparent top Al reflector.

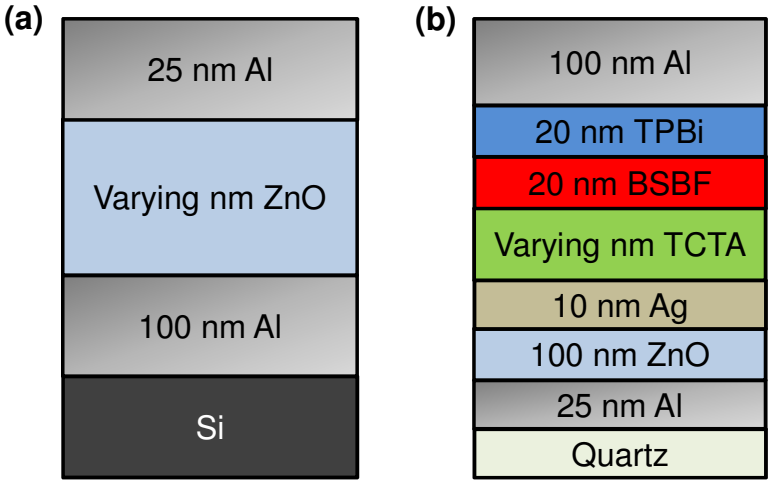

Figure 7.1 (a) The microcavity architectures of interest for devices containing only ZnO (a) or both ZnO and organic layers (b).

For measurements of the hybrid microcavity, a quartz slide was used as the substrate to eliminate any parasitic light absorption in the spectral range of the exciton-photon interaction (300-400 nm). The hybrid device shown in Fig. 7.1b consisted of a 25-nm-thick layer of Al, a 100-nm-thick layer of ZnO, a 10-nm-thick layer of Ag, a layer of the hole-transport material 4,4',4"-tris(carbazol-9-yl)triphenylamine (TCTA) of varying thickness, a 20-nm-thick emissive layer of BSBF (Fig. 7.2 inset), and a 20-nm-thick electron-transport layer of 2,2',2"-(1,3,5-benzinetriyl)-tris(1-phenyl-1-H-benzimidazole) (TPBi).[13,241] The device was capped with a cathode consisting of a 0.5-nm-thick layer of LiF followed by a 100-nm-thick layer of Al. Here, light is collected

through the semi-transparent bottom Al reflector. The transparent 10-nm-thick Ag layer serves as the device anode completely eliminating charge transport in the active coupling layer of ZnO without altering the cavity mode established between the Al reflectors. When excited, BSBF radiatively populates the polariton modes of the structure created by strong exciton-photon coupling between the cavity photon mode and the ZnO exciton. The broad absorption and emission (Fig. 7.2) features of BSBF ensure only a weak coupling with the cavity photon mode. In both cases, the reflectors forming the optical microcavity were chosen to be Al due to its high reflectivity extending well into the 300-400 nm spectral range.

Microcavities were characterized via angle resolved reflectivity and EL as a function of exciton-photon energy detuning. Varying the thickness of ZnO and TCTA in the case of the microcavity shown in Fig. 1a and Fig. 1b, respectively, changes the cavity mode energy, permitting a variation in the exciton-photon energy detuning. Reflectivity measurements were performed using a variable angle spectroscopic ellipsometer under s-polarized light illumination. For measurements of EL, devices were excited at a constant current density of 500 mA/cm^2. Uncoupled EL was collected as a function of detection angle.

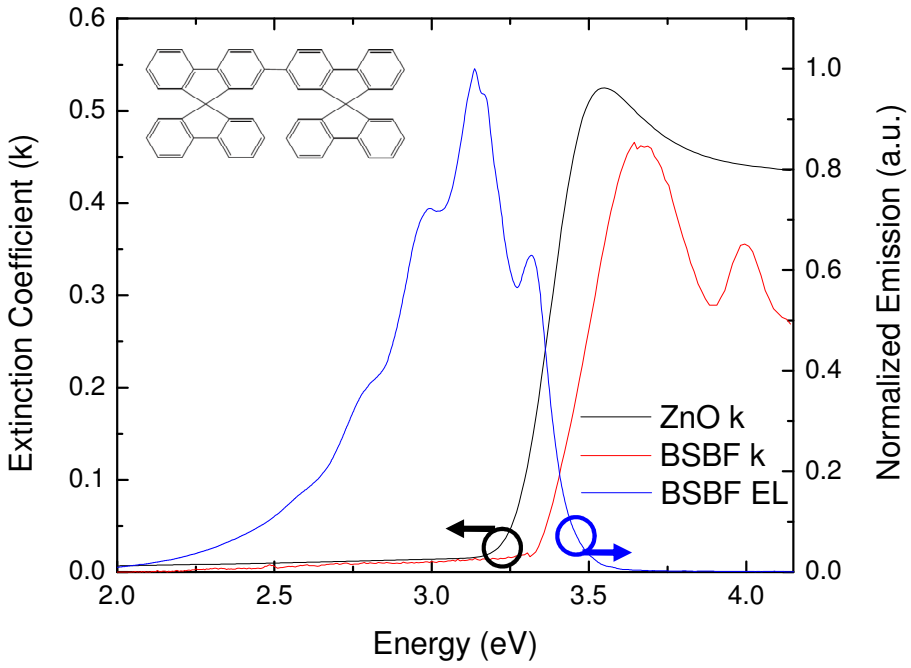

Figure 7.2 Extinction coefficients of ZnO and BSBF for 75- and 30-nm thick films, respectively. The electroluminescence spectra of BSBF was obtained in a device architecture consisting of ITO/40 nm TCTA/30 nm BSBF/30 nm TPBi/0.5 nm LiF/50 nm Al at a current density of 500 mA/cm^2. Inset: Molecular structure of BSBF.

7.3 Results and Discussion

Figure 7.2 shows the thin film extinction coefficients of ZnO and BSBF as well as the EL of BSBF. The optical transition of interest for strong coupling is centered at 3.55 eV, however, the absorption onset of ZnO is broad, suggesting that additional excitonic transitions could potentially exist in the 3.25 to 3.5 eV range. Zinc oxide grown via ALD crystallizes in a hexagonal wurtzite crystal structure and thus can have distinct excitonic transition energies along different crystallographic axes. The degree of crystallinity of ALD grown ZnO can differ drastically for different growth parameters, but under the

conditions here it is expected to be polycrystalline.[239] As such, the excitonic transition energies could be inconsistent as a result of the degree of crystallinity varying between separate ALD growths. Such considerations make it difficult to pinpoint a specific excitonic energy of interest for strong coupling.

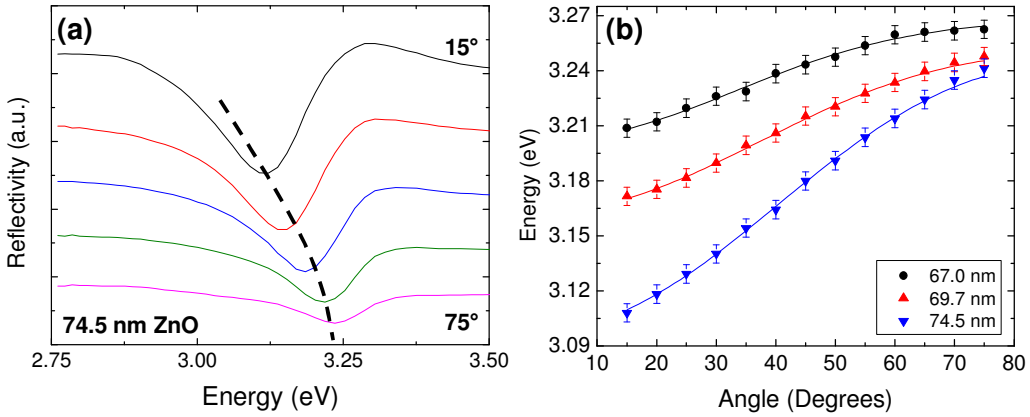

Figure 7.3 (a) Angle-resolved reflectivity spectra for the microcavity of Fig. 1a containing 74.5 nm of ZnO. A broken line highlights the dispersion of the lower branch polariton feature with angle. (b) Dispersion relations obtained from angle-resolved reflectivity measurements for microcavities containing 67.0, 69.7 and 74.5 nm-thick layers of ZnO. Solid lines are transfer matrix simulated dispersions for the microcavities of interest. Separately measured ZnO optical constants (n, k) and as-grown thicknesses were inputs to the transfer matrix simulation.

Angle-resolved reflectivity spectra for the microcavity of Fig. 1a containing a 74.5 nm-thick layer of ZnO are shown in Fig. 7.3a. A single spectral feature is observed which demonstrates strong dispersion with angle of incidence. The dispersion relations extracted from angle-resolved reflectivity spectra of three separate microcavities containing 67.0, 69.7 and 74.5 nm-thick layers of ZnO are shown in Fig. 7.3b. As the exciton-photon detuning is reduced with decreasing ZnO thickness, the three dispersion relations asymptote to different energies. This is uncharacteristic of a lower branch

polariton dispersion and could be attributed to the excitonic transition energy varying with growth conditions as each ZnO layer was grown separately. The energy of the asymptote, in each case, is much lower in energy than the peak in absorption (3.55 eV) which could be ascribed to the excitonic transition being buried in the broad absorption onset of ZnO. Additionally, as the cavity thickness is reduced, the dispersion relations start to flatten out, characteristic of lower polariton branch dispersions. The strong band-to-band absorption of ZnO as exhibited in Fig. 7.2 results in sufficient optical losses within the cavity at energies >3.45 eV making the observation of the upper branch polariton mode difficult. The dispersion relations of Fig. 7.3b were modeled using the optical transfer matrix model presented in Sec. 5.3 with appropriate device layer thicknesses and optical constants. Excellent agreement is obtained between the measured and simulated dispersion relations (solid lines, Fig. 7.3b).

Figure 7.4a shows angle-resolved reflectivity spectra for the hybrid microcavity of Fig. 7.1b containing a 25-nm-thick layer of TCTA. Consistent with measurements of reflectivity for the microcavity containing only ZnO, a single spectral feature is observed to exhibit strong dispersion with angle of incidence. The upper polariton branch is not observed for the same explanation described above. Figure 7.4b shows dispersion relations extracted from the angle-resolved reflectivity spectra of hybrid microcavities containing 20, 25 and 30-nm-thick layers of TCTA. Again, the dispersion relations flatten out with decreasing exciton-photon detuning (decreasing thickness) but asymptote to different energies which is uncharacteristic of a lower branch polariton dispersion (Fig. 7.4b). The energies of the asymptotes are more consistent with the uncoupled

exciton energy of 3.55 eV for ZnO. In fact, a coupled oscillator model fit (Sec. 2.3.2.1) of the dispersion relation for the microcavity containing a 20 nm-thick layer of TCTA yields an exciton energy of (3.55±0.10) eV, cavity length of (171.8±10) nm, refractive index of (2.1±0.1) and a Rabi splitting of (147±10) meV. The obtained cavity length is close to the total thickness of the device layers between the Al reflectors, the index of refraction is close to the expected value and the Rabi splitting is consistent with other demonstrations of strongly coupled ZnO microcavities. Coupled oscillator fits of the dispersion relations for microcavities containing 25 and 30 nm-thick layers of TCTA do not yield sensible values. However, excellent agreement is obtained between experimental and transfer matrix simulated dispersion curves for all TCTA thicknesses (Fig. 7.4b). This suggests that the exciton-photon detuning might be too large to obtain strong exciton-photon coupling for samples containing 25 and 30 nm-thick layers of TCTA and thus would be better fit as cavity photon modes. Samples containing <20 nm-thick layers of TCTA were not studied but would be a logical future extension of this work.

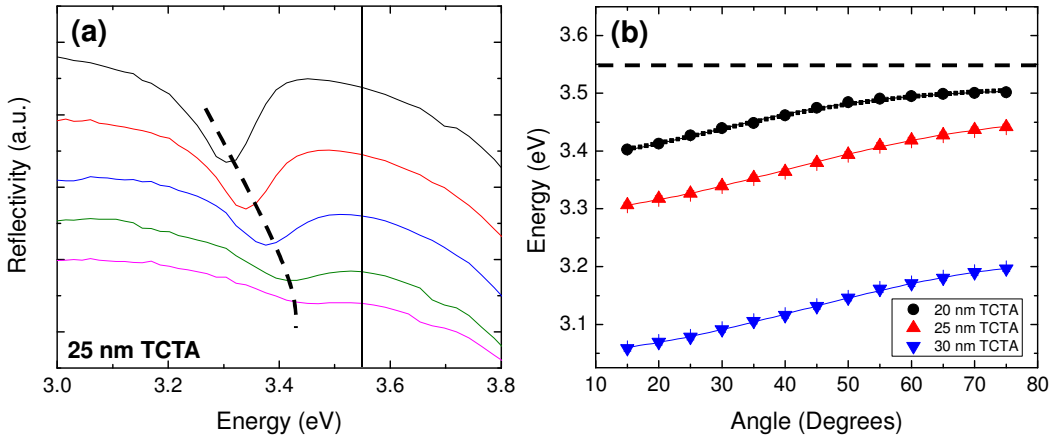

Figure 7.4 (a) Angle-resolved reflectivity spectra for the microcavity of Fig. 1b containing 25 nm of TCTA. A broken line highlights the dispersion of the lower branch polariton feature with angle while a solid line denotes the position of the uncoupled ZnO exciton. (b) Dispersion relations obtained from angle-resolved reflectivity measurements for microcavities containing 20, 25 and 30 nm-thick layers of TCTA. Solid lines are transfer matrix simulated dispersions for the microcavities of interest. The coupled oscillator model fit of the microcavity containing 20 nm TCTA is represented by the small solid boxes and overlays with the transfer matrix simulated dispersion (solid line). The broken line denotes the position of the uncoupled ZnO exciton.

Figure 7.5a shows angle-resolved EL for the microcavity of Fig. 7.1b containing a 35 nm-thick layer of TCTA. As in reflectivity, a single emission feature exhibits strong dispersion with angle of incidence. Significant emission intensity attenuation is observed with increasing angle of incidence characteristic of a lower polariton feature (as discussed in Sec. 2.3.4). However, excess ZnO on the backside of the substrate (an inherent problem of ALD) could also be the source of the observed intensity attenuation as the cavity mode approaches the tail of ZnO absorption with increasing angle of incidence. The additional feature observed at energies ~3.3 eV is attributed to uncoupled BSBF emission. The dispersion relations shown in Fig. 7.5b were constructed using peak fitting to extract peak centers from the EL spectra for microcavities (Fig. 1b) containing 35 and

40-nm-thick layers of TCTA. The dispersions of Fig. 7.5b asymptote to a common energy and flatten out with decreasing cavity thickness characteristic of lower branch polaritons. This is inconsistent, however, with the reflectivity results of Fig. 7.4b which indicate that hybrid microcavities containing ≥25 nm-thick layers of TCTA are uncoupled. Perhaps this could be attributed again to the ZnO excitonic transition varying in both oscillator strength and energy with growth conditions. The energy of the asymptote is much less than the ZnO excitonic transition (3.55 eV) which could be attributed to (as in the case of the ZnO only microcavity) the cavity photon mode coupling to a ZnO exciton transition buried in the broad absorption onset. The EL dispersion relations shown in Fig. 7.5b were modeled using the transfer matrix formulism presented in Sec. 5.3. Excellent agreement is obtained between the measured and simulated dispersion curves.

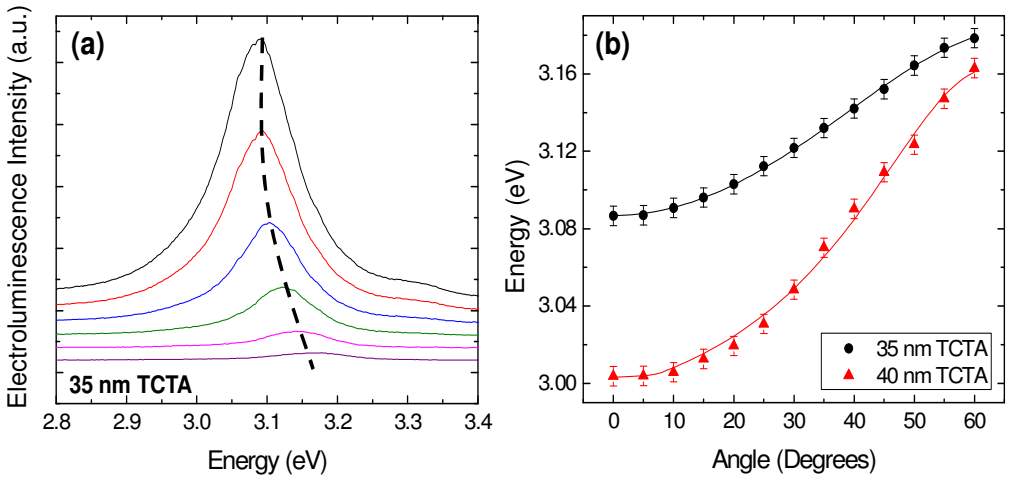

Figure 7.5 Angle-resolved EL (a) for the microcavity of Fig. 1b containing 35 nm of TCTA. A broken line highlights the dispersion of the lower branch polariton feature with angle. Dispersion relations extracted from angle-resolved measurements of EL for microcavities (Fig. 1b) containing 35 and 40-nm-thick layers of TCTA. The solid lines are transfer matrix simulated dispersions for the microcavities of interest.

7.4 Summary

In conclusion, a microcavity architecture was demonstrated which circumvents the problems associated with charge transport in an inorganic active coupling layer. Microcavity polaritons in this structure are radiatively pumped by a weakly coupled organic emissive layer under electrical excitation. Measurements of angle-resolved reflectivity and EL suggest that strong coupling under electrical excitation is realized but the absence of an upper branch and consistent ZnO exciton energy are issues which need to be resolved.[221,230] As such, potential improvements to this structure and the deposition process of ZnO are proposed in the following chapter. Additional characterization of ZnO thin films as a function of growth conditions is also suggested to clearly elucidate

the exciton energies of the material and to elucidate the inconsistencies presented in the data in this chapter.[240] Nevertheless, this device architecture provides an interesting platform to study the polariton dynamics of inorganic excitons under electrical excitation at room temperature.

I would like to acknowledge Rick Liptak for helping with the growth of the ZnO films studied in this work.

Chapter 8 Summary and Future Directions

This thesis has focused mainly on understanding and exploiting excitation mechanisms of polaritons in strongly coupled organic semiconductor microcavities. Even though some important developments have been established in this thesis, much work remains in the area with the ultimate goal being the realization of an electrically pumped coherent emitter based on microcavity polaritons operating at room temperature. This chapter will review the progress made in this work and provide potential directions for future research.

8.1 Summary

Chapter 3 provided the fundamental understanding of microcavity polariton excitation mechanisms in the metal-metal microcavities studied in this work. The population of microcavity polariton states was confirmed through temperature dependent luminescence measurements to occur via an uncoupled exciton reservoir. Consequently, this resulted in the inefficient excitation of the upper branch and a significant difference in emission intensity between the lower and upper polariton branches under optical and electrical excitation. In Chapter 4 an alternate excitation approach was devised that permit the direct population of microcavity polariton states under optical and electrical excitation without first forming an exciton reservoir. This was realized by introducing a weakly coupled emitter into an optical microcavity containing an organic semiconductor suitable for strong exciton-photon coupling. The angle-resolved measurements of the

photoluminescence (PL) and electroluminescence (EL) of this structure exhibited variations in the lower and upper branch emission intensity consistent with the branch photon character. The radiative pumping technique proved to be an important innovation leading to the elucidation of novel microcavity physics and polariton based optoelectronic devices.

In Sec. 4.6 the radiative pumping utility was extended to a phosphorescent microcavity system and shown to permit efficient population of microcavity polariton states reducing the amount of excitation lost via intersystem crossing to the triplet state. This technique also permits the study of the polarization dependence of both polariton branches under electrical excitation. As such, in Chapter 5 it was discovered that metal-metal microcavities exhibit a significant polarization splitting rivaling those observed in strongly coupled microcavities based on distributed Bragg reflectors characterized by a long optical penetration length. The polarization splitting was well simulated by an optical transfer matrix formulism and attributed to the polarization-dependent phase shift of optical field upon reflection from the metal mirrors. Chapter 7 employed yet another extension of the radiative pumping technique to facilitate electrical excitation of polariton modes in an inorganic semiconductor (ZnO) characterized by a small exciton binding energy.

Chapter 6 demonstrated a one-dimensional (1D) photonic crystal structure as an alternate architecture to confine light and establish strong exciton-photon coupling in organic semiconductors. The structure consisted of a high index of refraction light-absorbing active layer periodically distributed in a low index of refraction non-absorbing

background medium. The strongly coupled state in this structure was confirmed to be shared between multiple active layers separated by distances longer than the wavelength of light in the structure. In order to characterize the potential for long-range energy transfer, the photon-mediated exciton hybridization of multiple absorbing species was examined as a function of the spatial arrangement of the active layers in the photonic crystal. The device architectures and polariton excitation mechanisms presented here collectively contribute to the overall goal of this thesis to obtain a complete understanding of light-matter interactions in organic semiconductors and develop novel polariton-based optoelectronic devices.

8.2 Future Research

The understanding of organic strongly coupled microcavities and devices could be further expanded by extending the work presented in this thesis. The hybrid organic/inorganic microcavity shown in Chapter 7 needs to be further characterized to determine precisely the regime of exciton-photon coupling. It would be beneficial to experimentally analyze the polariton dynamics of the device architectures in Chapters 3, 4, 6 and 7 to precisely measure the relaxation processes in these structures and to conclude whether polariton non-linear scattering processes are present.

8.2.1 Hybrid Organic/Inorganic Microcavities

The hybrid microcavity in Chapter 7 needs to be further characterized and potentially improved to determine the effectiveness of radiative pumping as a technique to electrically excite inorganic polariton states. The dispersion relations for the hybrid

microcavity were demonstrated to asymptote to different energies under reflectivity and electroluminescence (EL) implying a potential discrepancy in the energy of the ZnO excitonic transition. Zinc oxide grown via atomic layer deposition (ALD) crystallizes in a hexagonal wurtzite crystal structure potentially resulting in distinct excitonic transition energies along different crystallographic axes (Fig. 8.1).[239,240] Temperature-dependent absorption measurements of thin films of ZnO would elucidate the exciton absorption features by reducing inhomogeneous broadening effects with decreasing temperature (Fig. 8.1).[230] X-ray diffraction experiments performed in parallel would connect the temperature dependent absorption results to the microstructure of ZnO, perhaps providing insight into a preferred morphology.[239,240] The atomic layer deposition (ALD) growth parameters could then tailored to obtain the desired morphology for a microcavity structure of interest.

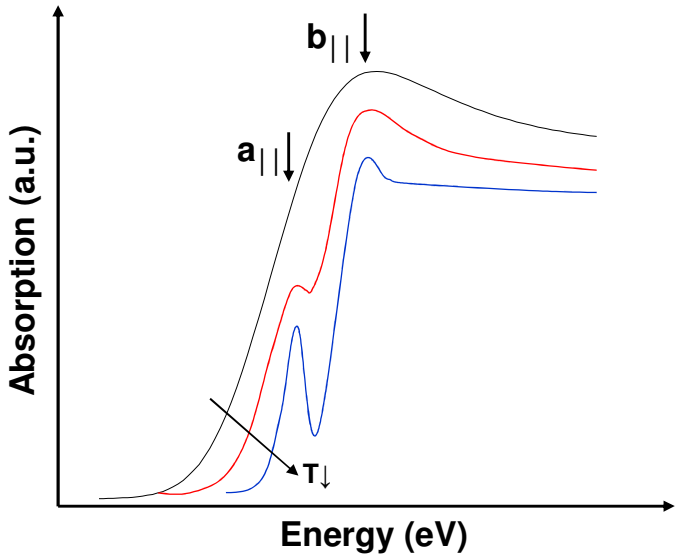

Figure 8.1 Schematic of potential results from temperature-dependent absorption measurements of a thin film of ZnO. Inhomogeneous broadening is reduced with decreasing temperature, elucidating the excitonic transitions of ZnO oxide corresponding to the a-axis ($a_{\perp}$) and b-axis ($b_{\perp}$) of the hexagonal wurtzite crystal structure. There could also be a c-axis excitonic transition which is not shown here.

Another potential problem of the hybrid structure presented in Chapter 7 is that the 2-(9,9-spirobifluoren-2-yl)-9,9-spirobifluorene (BSBF) emission is lower in energy than the ZnO excitonic transition. This could prove to be an issue for efficient radiative pumping of the strongly coupled state, specifically the upper polariton branch. One plausible solution would be to use a blue-shifted organic emitter. Such a material, however, would have a wide energy gap possibly making electrical injection problematic. Another potential solution would be to employ GaN instead of ZnO as the active coupling material in the microcavity.[141,161,220,223,234,242] The excitonic transition of GaN is 3.42 as opposed to 3.55 eV for ZnO, providing better overlap with BSBF emission (Fig. 8.2a).[142] The optical properties of GaN are sensitive to defects posing growth challenges. However, the tensile strain incurred during growth (cause of defects) can be alleviated by choosing a lattice matched substrate such as an $Al_{0.85}In_{0.15}N/Al_{0.2}Ga_{0.8}N$ distributed Bragg reflector (DBR).[142] Figure 8.2b shows a potential GaN hybrid architecture similar to the structure shown in Chapter 7. This structure would have a much larger cavity quality factor (Q) due to the bottom DBR potentially making possible the realization of non-linear polariton processes.

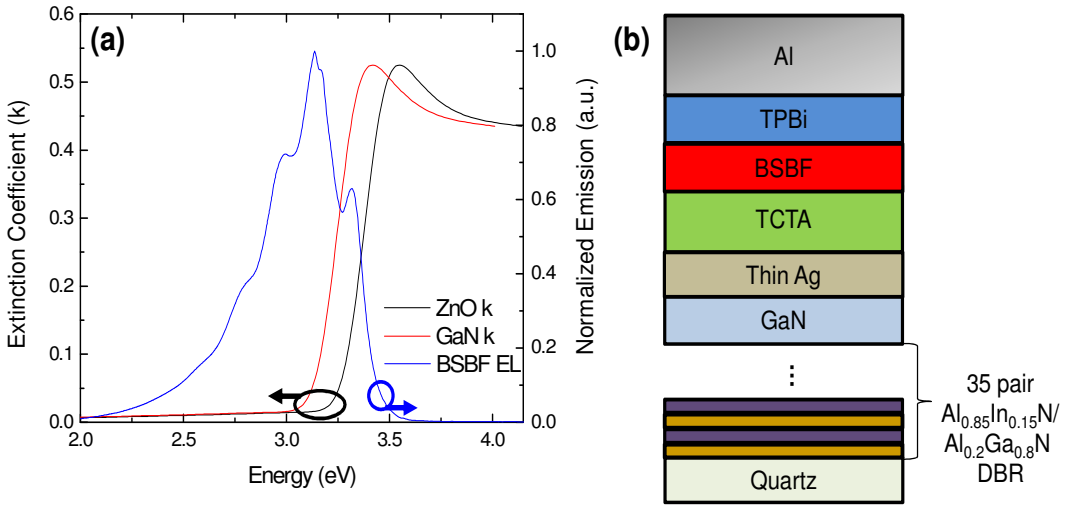

Figure 8.2 (a) Extinction coefficients of ZnO and GaN (arbitrary but energy shifted appropriately). The electroluminescence spectra of BSBF exhibits better spectral overlap with GaN absorption than that of ZnO permitting more efficient radiative pumping. (b) Potential hybrid microcavity structure incorporating GaN as the active coupling layer.

8.2.2 Ultrafast Spectroscopy

In order to engineer both electrically pumped polariton light-emitting devices for the realization of organic polariton coherent light emitters (polariton lasers) polariton scattering processes must be present. To date, it is inconclusive whether organic microcavities exhibit the polariton scattering phenomena required to force the system towards a macroscopic occupancy of polariton states.[122,174,216] Since polaritons are mixed states of photon and exciton character, their lifetimes are a function of the constituent lifetimes.[132] For the metal-metal microcavities studied in this work, the low cavity Q implies that the polariton time dynamics are very short, on the order of 10's of fs, owing to the photon lifetime in the metal-metal resonator. Consequently, polaritons created with arbitrary in-plane wave vector do not undergo further relaxation in energy and momentum.

The microcavity architectures presented in Chapters 3 and 4 could be modified to enhance the degree of optical confinement by increasing the reflectivity of the resonator mirrors.[163] This could be accomplished by employing DBR reflectors to form the optical microcavity.[163] By creating polariton states with longer lifetimes, it may be possible to observe polariton scattering processes. A potential device architecture is shown in Fig. 8.3 for the microcavity studied in Chapter 3, respectively. Electrical excitation, although more difficult to accomplish with insulating DBRs as cavity reflectors could be realized, for example, by introducing thin metallic or transparent conducting contact layers into the microcavity of interest as demonstrated in Chapter 7. The inter-cavity contact layers would require optimization to ensure that the high cavity Q is retained. Such a device would be an attractive platform to study potential polariton scattering processes under both optical and electrical excitation.

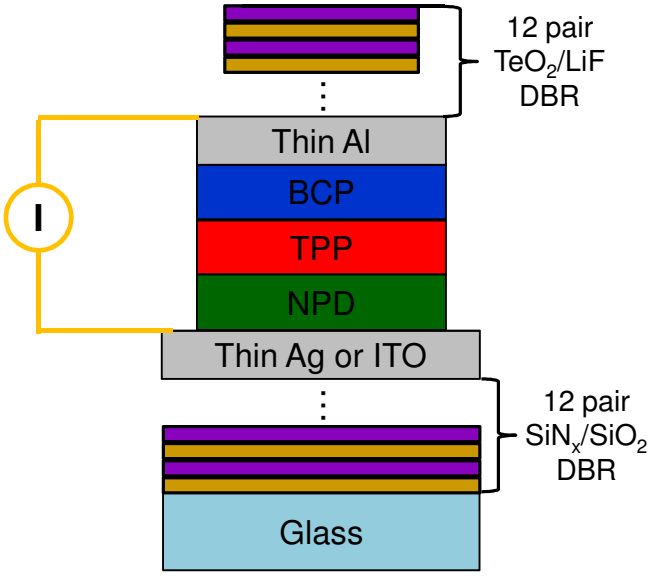

Figure 8.3 A potential high-Q organic microcavity architecture to facilitate the study of the polariton scattering dynamics. The top TeO_2/LiF DBR could be thermally evaporated to prevent damage to the underlying organic layers. The intercavity contact layers could either consist of thin layers of metal or transparent conductors. BCP, TPP and NPD are defined in Chapter 3.

Ultrafast laser spectroscopy would allow for direct measurement of polariton population mechanisms and scattering dynamics.[122,174,216] For instance, the rates of polariton excitation for the lower and upper branch calculated in Chapter 3 could be confirmed through measurements of ultrafast laser spectroscopy. In such a measurement, polaritons would be created optically by a pump source by either resonant (magic angle on lower polariton branch as discussed in Sec. 2.42) or non-resonant excitation (Sec. 2.43). This would require that the pump source be wavelength (energy) and angle of incidence tunable to target precise energy and in-plane angular momentum (angle of incidence) polariton states in the dispersion relation. A time-delayed (from the pump) pulse from another tunable ultrafast light source would be used to probe the device. Several configurations of the experiment could be envisioned to analyze the polariton relaxation dynamics.

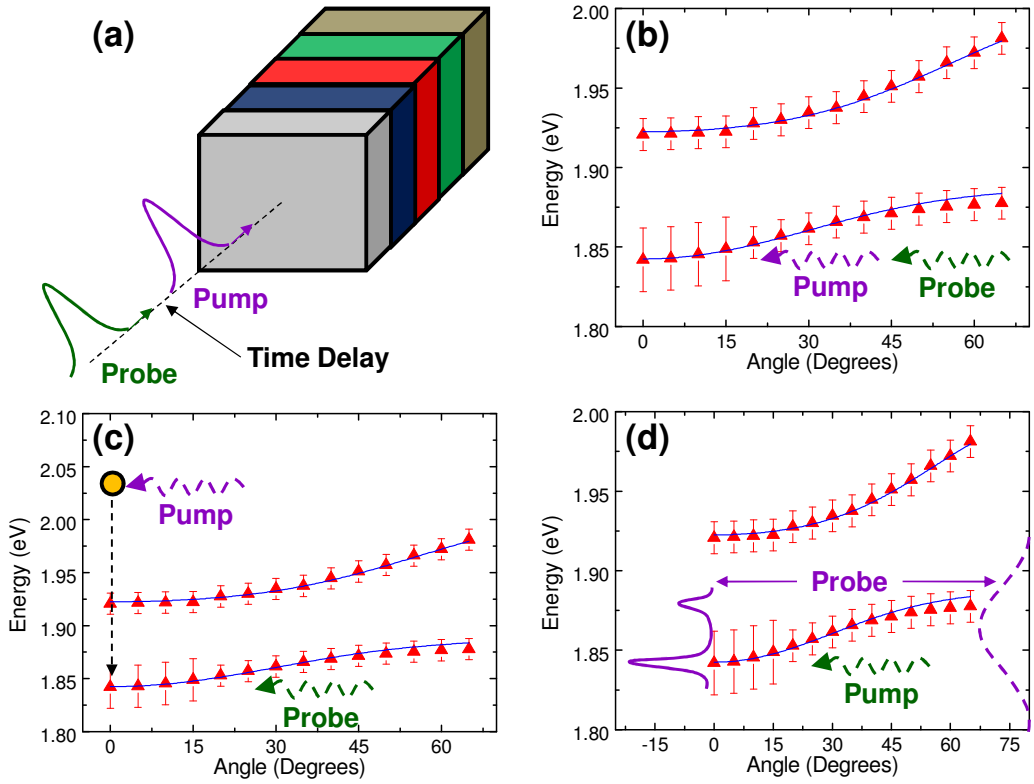

Figure 8.4 (a) A generic schematic of an ultrafast laser experiment. The response of the probe pulse is measured as a function of the pump power and pump/probe delay time. (b) A proof of concept experiment pumping and probing at $k_{||}=0$ to examine if a macroscopic population of polariton states at $k_{||}=0$ is feasible. (c) A non-resonant pumping experiment. The pump excites a population of excitons (filled circle) of the active material. The relaxation of the active material excitons to $k_{||}=0$ polaritons is measured by monitoring the intensity change of the probe pulse before and after being transmitted through the sample. (d) A resonant pumping experiment where the probe is incident at the magic angle. The probe pulse intensity and spectral shape is examined before and after being transmitted through the sample. Parametric scattering would result in two dominant peaks (as shown by the output pulse left of the dispersion) in intensity, one at $k_{||}=0$ and the other at high momentum and energy.

An interesting study would be to monitor the transmission of the probe pulse at $k_{||}=0$ (on the lower polariton branch dispersion) with and without the pump pulse as a function of the pump power and pump/probe delay time as shown in Fig. 8.4a and 8.4b.

Enhancement of the probe pulse intensity would imply gain signifying the existence of a macroscopic occupancy of polariton states at $k_{||}=0$ created by the pump. This experiment would serve as a simple check to confirm that macroscopic population at $k_{||}=0$ is in fact possible for the microcavity of interest. The experiment could then be extended to pump the sample non-resonantly at the wavelength (energy) of the active material absorption peak (Fig. 8.4c). In this configuration, the probe beam at $k_{||}=0$ would again be monitored as a function of pump power/probe delay time. The pump pulse, in this case, creates active layer uncoupled excitons which relax to create polaritons with arbitrary energy and in-plane momentum thus requiring polariton relaxation to build-up a macroscopic population at $k_{||}=0$. Gain exhibited by the probe pulse would confirm the existence of polariton relaxation processes. Finally, the sample of interest could be pumped under resonant excitation (Sec. 2.4.2) at the magic angle (Fig. 8.4d). Again, the probe transmission intensity would be monitored as a function of pump power/probe delay time. Parametric (pair-wise) polariton scattering processes could be observed in this process by choosing a spectrally broad probe pulse (broad enough to span the lower polariton branch) tuned by angle of incidence. Observation of two spectral features (one at $k_{||}=0$ and another at high momentum and energy) exhibiting gain would indicate parametric scattering. Any of these experiments, if successful, would be a major breakthrough in the field as non-linear polariton processes have not been demonstrated to date in any organic semiconductor microcavity.

Perhaps the most interesting device to study via ultrafast laser spectroscopy would be the 1D photonic crystal architecture presented in Chapter 6. By engineering the

amount of high-index/low-index pairs, the optical confinement of the structure can be significantly enhanced potentially permitting polariton relaxation processes. Recently, polariton amplification was demonstrated in an inorganic based 1D photonic crystal structure by ultrafast laser spectroscopy.[204] This result is exciting and could potentially be applied to the organic structure presented in this thesis. Preliminary angle-resolved photoluminescence measurements of the all-organic photonic crystal architecture developed in Chapter 6 suggest that resonant excitation is required due to the presence of significant uncoupled emission under non-resonant excitation. In fact, dispersionless uncoupled TPP emission dominates the angle-resolved PL spectra making the resolution of any angle-dependent features difficult. Resonant excitation of the lower polariton branch would avoid direct optical pumping of TPP and eliminate altogether uncoupled TPP emission in this structure. More investigation into this novel architecture could prove to be beneficial and result in the first demonstration of polariton scattering processes in organic materials.

8.3 Afterword

With the recent development of room temperature polariton lasing, the future is certainly bright for organic polariton-based optoelectronic devices. The fundamental device physics and novel architectures presented in this work could be instrumental to the future development of the field. It is felt by the author that an electrically pumped polariton-based coherent emitter will be realized in the near future.

Chapter 9 Bibliography

1 D. A. Neamen, *Semiconductor Physics and Devices* (McGraw-Hill, New York, 2003).

2 G. Bjork, H. Heitmann, and Y. Yamamoto, Phys. Rev. A **47**, 4451 (1993).

3 H. Morkoc, S. Strite, G. B. Gao, M. E. Lin, B. Sverdlov, and M. Burns, J. Appl. Phys. **76**, 1363 (1994).

4 R. F. Pierret, *Advanced Semiconductor Fundamentals* (Pearson Education, New Jersey, 2003), VI.

5 C. W. Tang, Appl. Phys. Lett. **48**, 183 (1986).

6 C. W. Tang and S. A. Vanslyke, Appl. Phys. Lett. **51**, 913 (1987).

7 C. W. Tang, S. A. VanSlyke, and C. H. Chen, J. Appl. Phys. **65**, 3610 (1989).

8 C. Adachi, R. Kwong, P. Djurovich, V. Adamovich, M. Baldo, M. Thompson, and S. Forrest, Appl. Phys. Lett. **79**, 2082 (2001).

9 M. Ikai, S. Tokito, Y. Sakamoto, T. Suzuki, and Y. Taga, Appl. Phys. Lett. **79**, 156 (2001).

10 L. Hung and C. Chen, Mater. Sci. Eng. R-Rep. **39**, 143 (2002).

11 U. Mitschke and P. Bauerle, J. Mater. Chem. **10**, 1471 (2000).

12 R. Friend, R. Gymer, A. Holmes*, et al*, Nature **397**, 121 (1999).

13 Z. Gao, C. Lee, I. Bello, S. Lee, R. Chen, T. Luh, J. Shi, and C. Tang, Appl. Phys. Lett. **74**, 865 (1999).

14 N. Tessler, Adv Mater **11**, 363 (1999).

15 R. Gupta, M. Stevenson, A. Dogariu, M. McGehee, J. Park, V. Srdanov, A. Heeger, and H. Wang, Appl. Phys. Lett. **73**, 3492 (1998).

16 V. Kozlov, V. Bulovic, P. Burrows, and S. Forrest, Nature **389**, 362 (1997).

17 M. Berggren, O. Inganas, T. Granlund, S. Guo, G. Gustafsson, and M. Andersson, Synth. Met. **76**, 121 (1996).

18 V. Kozlov, G. Parthasarathy, P. Burrows, V. Khalfin, J. Wang, S. Chou, and S. Forrest, IEEE J. Quant. Electron. **36**, 18 (2000).

19 C. Adachi, M. Baldo, S. Forrest, and M. Thompson, Appl. Phys. Lett. **77**, 904 (2000).

20 J. Sheats, H. Antoniadis, M. Hueschen, W. Leonard, J. Miller, R. Moon, D. Roitman, and A. Stocking, Science **273**, 884 (1996).

21 D. Wohrle and D. Meissner, Adv Mater **3**, 129 (1991).

22 A. Hagfeldt and M. Gratzel, Acc. Chem. Res. **33**, 269 (2000).

23 P. Peumans, A. Yakimov, and S. Forrest, J. Appl. Phys. **93**, 3693 (2003).

24 P. Peumans, S. Uchida, and S. Forrest, Nature **425**, 158 (2003).

25 H. Spanggaard and F. Krebs, Solar Energy Mater. Solar Cells **83**, 125 (2004).

26 C. Brabec, Solar Energy Mater. Solar Cells **83**, 273 (2004).

27 B. P. Rand, J. Genoe, P. Heremans, and J. Poortmans, Prog. Photovoltaics **15**, 659 (2007).

28 B. Kippelen and J. Bredas, Energy Environ. Sci. **2**, 251 (2009).

29 J. Bredas, J. E. Norton, J. Cornil, and V. Coropceanu, Acc. Chem. Res. **42**, 1691 (2009).

30 M. Pope and C. E. Swenberg, *Electronic Processes in Organic Crystals and Polymers* (Oxford University Press, New York, 1999).

31 H. Katz, Chem. Mat. **16**, 4748 (2004).

32 S. Forrest, Nature **428**, 911 (2004).

33 F. C. Krebs, S. A. Gevorgyan, and J. Alstrup, J. Mater. Chem. **19**, 5442 (2009).

34 R. Gaudiana and C. Brabec, Nat. Photonics **2**, 287 (2008).

35 H. Klauk, M. Halik, U. Zschieschang, F. Eder, D. Rohde, G. Schmid, and C. Dehm, IEEE Trans. Electron Devices **52**, 618 (2005).

36 C. Newman, C. Frisbie, D. da Silva, J. Bredas, P. Ewbank, and K. Mann, Chem. Mat. **16**, 4436 (2004).

37 D. Knipp, R. Street, A. Volkel, and J. Ho, J. Appl. Phys. **93**, 347 (2003).

38 R. Xia, G. Heliotis, Y. Hou, and D. Bradley, Org. Electron. **4**, 165 (2003).

39 B. Crone, A. Dodabalapur, Y. Lin, R. Filas, Z. Bao, A. LaDuca, R. Sarpeshkar, H. Katz, and W. Li, Nature **403**, 521 (2000).

40 A. Dodabalapur, L. J. Rothberg, and T. M. Miller, Electron. Lett. **30**, 1000 (1994).

41 D. Datta, S. S. K. Iyer, and S. Kumar, in *Photovoltaic Specialists Conference (PVSC), 2010 35th IEEE*, 2010), p. 000508.

42 Y. Liang, Z. Xu, J. Xia, S. Tsai, Y. Wu, G. Li, C. Ray, and L. Yu, Adv Mater **22**, E135 (2010).

43 N. Tessler, Y. Preezant, N. Rappaport, and Y. Roichman, Adv Mater **21**, 2741 (2009).

44 I. D. W. Samuel and G. A. Turnbull, Chem. Rev. **107**, 1272 (2007).

45 S. Shaheen, D. Ginley, and G. Jabbour, MRS Bull **30**, 10 (2005).

46 C. Adachi, M. Baldo, S. Forrest, S. Lamansky, M. Thompson, and R. Kwong, Appl. Phys. Lett. **78**, 1622 (2001).

47 P. I. Djurovich, E. I. Mayo, S. R. Forrest, and M. E. Thompson, Org. Electron. **10**, 515 (2009).

48 S. Tadayyon, H. Grandin, K. Griffiths, L. Coatsworth, P. Norton, H. Aziz, and Z. Popovic, Org. Electron. **5**, 199 (2004).

49 P. Harrison, *Quantum Wells, Wires and Dot: Theoretical and Computational Physics* (John Wiley and Sons, Inc., New York, 2000).

50 N. J. Turro, *Modern Molecular Photochemistry* (University Science Books, Sausalito, California, 1991).

51 F. Gutmann and L. E. Lyons, *Organic Semiconductors* (John Wiley and Sons, Inc., New York, 1967).

52 J. R. Lakowicz, *Principles of Fluorescence Spectroscopy* (Plenum Press, New York, 1983).

53 H. Nakanotani, H. Sasabe, and C. Adachi, Appl. Phys. Lett. **86**, 213506 (2005).

54 M. A. Baldo, R. J. Holmes, and S. R. Forrest, Phys. Rev. B **66**, 035321 (2002).

55 C. Kittel, *Introduction to Solid State Physics* (John Wiley and Sons, Inc., New York City, 2005).

56 N. W. Ashcroft and N. D. Mermin, *Solid State Physics* (Brooks Cole, Salt Lake City, 1976).

57 R. Holmes, B. D'Andrade, S. Forrest, X. Ren, J. Li, and M. Thompson, Appl. Phys. Lett. **83**, 3818 (2003).

58 C. Adachi, M. Baldo, M. Thompson, and S. Forrest, J. Appl. Phys. **90**, 5048 (2001).

59 S. Lamansky, P. Djurovich, D. Murphy, F. Abdel-Razzaq, H. Lee, C. Adachi, P. Burrows, S. Forrest, and M. Thompson, J. Am. Chem. Soc. **123**, 4304 (2001).

60 M. Baldo, M. Thompson, and S. Forrest, Nature **403**, 750 (2000).

61 M. Baldo, D. O'Brien, Y. You, A. Shoustikov, S. Sibley, M. Thompson, and S. Forrest, Nature **395**, 151 (1998).

62 J. D. Wright, *Molecular Crystals* (Cambridge University Press, Cambridge, 1995).

63 S. Forrest, Chem. Rev. **97**, 1793 (1997).

64 Y. Shirota, J. Mater. Chem. **10**, 1 (2000).

65 M. Baldo, D. O'Brien, M. Thompson, and S. Forrest, Phys. Rev. B **60**, 14422 (1999).

66 A. Yariv, *Optical Electronics in Modern Communications* (Oxford University Press, New York, 1997).

67 M. Berggren, A. Dodabalapur, R. Slusher, A. Timko, and O. Nalamasu, Appl. Phys. Lett. **72**, 410 (1998).

68 V. Bulovic, V. Kozlov, V. Khalfin, and S. Forrest, Science **279**, 553 (1998).

69 M. Berggren, A. Dodabalapur, and R. Slusher, Appl. Phys. Lett. **71**, 2230 (1997).

70 M. Berggren, A. Dodabalapur, R. Slusher, and Z. Bao, Nature **389**, 466 (1997).

71 S. Kena-Cohen and S. R. Forrest, Nat. Photonics **4**, 371 (2010).

72 S. Frolov, Z. Vardeny, K. Yoshino, A. Zakhidov, and R. Baughman, Phys. Rev. B **59**, R5284 (1999).

73 S. Frolov, M. Shkunov, Z. Vardeny, and K. Yoshino, Phys. Rev. B **56**, R4363 (1997).

74 S. Frolov, M. Ozaki, W. Gellermann, Z. Vardeny, and K. Yoshino, Jpn. J. Appl. Phys. Part 2 - Lett. **35**, L1371 (1996).

75 N. Tessler, G. Denton, and R. Friend, Nature **382**, 695 (1996).

76 C. Weisbuch, M. Nishioka, A. Ishikawa, and Y. Arakawa, Phys. Rev. Lett. **69**, 3314 (1992).

77 C. Zenz, W. Graupner, S. Tasch, G. Leising, K. Mullen, and U. Scherf, Appl. Phys. Lett. **71**, 2566 (1997).

78 D. Fichou, S. Delysse, and J. Nunzi, Adv Mater **9**, 1178 (1997).

79 A. Dodabalapur, L. J. Rothberg, R. H. Jordan, T. M. Miller, R. E. Slusher, and J. M. Phillips, J. Appl. Phys. **80**, 6954 (1996).

80 A. Dodabalapur, L. J. Rothberg, and T. M. Miller, Appl. Phys. Lett. **65**, 2308 (1994).

81 A. Dodabalapur, L. J. Rothberg, T. M. Miller, and E. W. Kwock, Appl. Phys. Lett. **64**, 2486 (1994).

82 N. Takada, T. Tsutsui, and S. Saito, Appl. Phys. Lett. **63**, 2032 (1993).

83 E. F. Schubert, Y. H. Wang, A. Y. Cho, L. W. Tu, and G. J. Zydzik, Appl. Phys. Lett. **60**, 921 (1992).

84 E. F. Schubert, N. E. J. Hunt, M. Micovic, R. J. Malik, D. L. Sivco, A. Y. Cho, and G. J. Zydzik, Science **265**, 943 (1994).

85 H. Deneve, J. Blondelle, R. Baets, P. Demeester, P. Vandaele, and G. Borghs, IEEE Photonics Technol. Lett. **7**, 287 (1995).

86 M. Steiner, F. Schleifenbaum, C. Stupperich, A. Failla, A. Hartschuh, and A. Meixner, ChemPhysChem **6**, 2190 (2005).

87 I. H. Tan, J. J. Dudley, D. I. Babic, D. A. Cohen, B. D. Young, E. L. Hu, J. E. Bowers, B. I. Miller, U. Koren, and M. G. Young, IEEE Photonics Technol. Lett. **6**, 811 (1994).

88 S. Murtaza, I. Tan, J. Bowers, E. Hu, K. Anselm, M. Islam, R. Chelakara, R. Dupuis, B. Streetman, and J. Campbell, J. Lightwave Technol. **14**, 1081 (1996).

89 M. Gokkavas, B. Onat, E. Ozbay, E. Ata, J. Xu, E. Towe, and M. Unlu, IEEE J. Quant. Electron. **35**, 208 (1999).

90 A. Green, D. Gevaux, C. Roberts, and C. Phillips, Physica E **20**, 531 (2004).

91 N. E. J. Hunt, E. F. Schubert, R. A. Logan, and G. J. Zydzik, Appl. Phys. Lett. **61**, 2287 (1992).

92 N. E. J. Hunt, E. F. Schubert, and G. J. Zydzik, Appl. Phys. Lett. **63**, 391 (1993).

93 T. Singh, U. Waghmare, and K. Narayan, Appl. Phys. Lett. **80**, 1213 (2002).

94 M. Unlu, M. Emsley, O. Dosunmu, P. Muller, and Y. Leblebici, J. Vac. Sci. Technol. A **22**, 781 (2004).

95 K. H. An, B. O'Connor, K. P. Pipe, and M. Shtein, Org. Electron. **10**, 1152 (2009).

96 H. Benisty, J. -. Gerard, R. Houdre, J. Rarity, and C. Weisbuch, *Confined Photon Systems: Fundamentals and Applications* (Springer, Berlin, 1998).

97 E. Burnstein and C. Weisbuch, *Confined Electrons and Photons: New Physics and Applications* (Plenum Press, New York, 1995).

98 Y. Yamamoto, F. Tassone, and H. Cao, *Semiconductor Cavity Quantum Electrodynamics* (Springer-Verlag, New York, 2000).

99 M. S. Skolnick, T. A. Fisher, and D. M. Whittaker, Semicond. Sci. Technol. **13**, 645 (1998).

100 V. M. Agranovich and Y. N. Gartstein, Phys. Rev. B **75**, 075302 (2007).

101 V. M. Kenkre and P. Reineker, *Exciton Dynamics in Molecular Crystals and Aggregates* (Springer-Verlag, New York, 1982).

102 V. Savona, L. C. Andreani, P. Schwendimann, and A. Quattropani, Solid State Commun. **93**, 733 (1995).

103 E. M. Purcell, Physical Review B **69**, 681 (1946).

104 J. Gerard and B. Gayral, J. Lightwave Technol. **17**, 2089 (1999).

105 H. Yokoyama, K. Nishi, T. Anan, H. Yamada, S. D. Brorson, and E. P. Ippen, Appl. Phys. Lett. **57**, 2814 (1990).

106 H. Yokoyama, Science **256**, 66 (1992).

107 H. Benisty, H. De Neve, and C. Weisbuch, IEEE J. Quant. Electron. **34**, 1612 (1998).

108 D. G. Deppe, C. Lei, C. C. Lin, and D. L. Huffaker, J. Mod. Opt. **41**, 325 (1994).

109 R. H. Jordan, L. J. Rothberg, A. Dodabalapur, and R. E. Slusher, Appl. Phys. Lett. **69**, 1997 (1996).

110 V. M. Agranovich, M. Litinskaia, and D. G. Lidzey, Phys. Rev. B **67**, 085311 (2003).

111 P. Michetti and G. C. La Rocca, Phys. Rev. B **77**, 195301 (2008).

112 P. Michetti and G. C. La Rocca, Phys. Rev. B **79**, 035325 (2009).

113 G. C. La Rocca, F. Bassani, and V. M. Agranovich, J. Opt. Soc. Am. B-Opt. Phys. **15**, 652 (1998).

114 L. Mazza, L. Fontanesi, and G. C. La Rocca, Phys. Rev. B **80**, 235314 (2009).

115 C. Ciuti, P. Schwendimann, B. Deveaud, and A. Quattropani, Phys. Rev. B **62**, R4825 (2000).

116 G. Ramon, R. Rapaport, A. Qarry, E. Cohen, A. Mann, A. Ron, and L. Pfeiffer, Phys. Rev. B **65**, 085323 (2002).

117 V. Savona, Z. Hradil, A. Quattropani, and P. Schwendimann, Phys. Rev. B **49**, 8774 (1994).

118 V. Agranovich, H. Benisty, and C. Weisbuch, Solid State Commun. **102**, 631 (1997).

119 D. J. Griffiths, *Introduction to Quantum Mechanics* (Pearson Education, New Jersey, 1995).

120 L. A. A. Pettersson, L. S. Roman, and O. Inganas, J. Appl. Phys. **86**, 487 (1999).

121 L. C. Andreani, F. Tassone, and F. Bassani, Solid State Commun. **77**, 641 (1991).

122 P. G. Savvidis, L. G. Connolly, M. S. Skolnick, D. G. Lidzey, and J. J. Baumberg, Phys. Rev. B **74**, 113312 (2006).

123 D. G. Lidzey, D. D. C. Bradley, M. S. Skolnick, T. Virgili, S. Walker, and D. M. Whittaker, Nature **395**, 53 (1998).

124 D. G. Lidzey, D. D. C. Bradley, T. Virgili, A. Armitage, M. S. Skolnick, and S. Walker, Phys. Rev. Lett. **82**, 3316 (1999).

125 J. Wenus, S. Ceccarelli, D. G. Lidzey, A. I. Tolmachev, J. L. Slominskii, and J. L. Bricks, Org. Electron. **8**, 120 (2007).

126 J. Wenus, L. G. Connolly, D. M. Whittaker, M. S. Skolnick, and D. G. Lidzey, Appl. Phys. Lett. **85**, 5848 (2004).

127 J. R. Tischler, M. S. Bradley, V. Bulovic, J. H. Song, and A. Nurmikko, Phys. Rev. Lett. **95**, 036401 (2005).

128 R. Houdre, R. P. Stanley, U. Oesterle, M. Ilegems, and C. Weisbuch, Phys. Rev. B **49**, 16761 (1994).

129 S. Kena-Cohen and S. R. Forrest, Phys. Rev. B **76**, 075202 (2007).

130 R. J. Holmes and S. R. Forrest, Phys. Rev. B **71**, 235203 (2005).

131 R. Houdre, C. Weisbuch, R. P. Stanley, U. Oesterle, P. Pellandini, and M. Ilegems, Phys. Rev. Lett. **73**, 2043 (1994).

132 D. G. Lidzey, A. M. Fox, M. D. Rahn, M. S. Skolnick, V. M. Agranovich, and S. Walker, Phys. Rev. B **65**, 195312 (2002).

133 N. Takada, T. Kamata, and D. D. C. Bradley, Appl. Phys. Lett. **82**, 1812 (2003).

134 S. Ceccarelli, J. Wenus, M. S. Skolnick, and D. G. Lidzey, Superlattices Microstruct. **41**, 289 (2007).

135 Y. Yamamoto and R. E. Slusher, Phys Today **46**, 66 (1993).

136 H. Benisty, R. Stanley, and M. Mayer, J. Opt. Soc. Am. A-Opt. Image Sci. Vis. **15**, 1192 (1998).

137 M. S. Skolnick, A. I. Tartakovskii, R. Butte, D. M. Whittaker, and R. M. Stevenson, IEEE J. Sel. Top. Quantum Electron. **8**, 1060 (2002).

138 F. Tassone and Y. Yamamoto, Phys. Rev. B **59**, 10830 (1999).

139 D. Bajoni, E. Semenova, A. Lemaitre, S. Bouchoule, E. Wertz, P. Senellart, and J. Bloch, Phys. Rev. B **77**, 113303 (2008).

140 R. Butte, G. Delalleau, A. I. Tartakovskii, M. S. Skolnick, V. N. Astratov, J. J. Baumberg, G. Malpuech, A. Di Carlo, A. V. Kavokin, and J. S. Roberts, Phys. Rev. B **65**, 205310 (2002).

141 G. Christmann, R. Butte, E. Feltin, J. Carlin, and N. Grandjean, Appl. Phys. Lett. **93**, 051102 (2008).

142 S. Christopoulos, G. B. H. von Hogersthal, A. J. D. Grundy*, et al*, Phys. Rev. Lett. **98**, 126405 (2007).

143 H. Deng, G. Weihs, C. Santori, J. Bloch, and Y. Yamamoto, Science **298**, 199 (2002).

144 R. Huang, Y. Yamamoto, R. Andre, J. Bleuse, M. Muller, and H. Ulmer-Tuffigo, Phys. Rev. B **65**, 165314 (2002).

145 P. G. Lagoudakis, M. D. Martin, J. J. Baumberg, G. Malpuech, and A. Kavokin, J. Appl. Phys. **95**, 2487 (2004).

146 G. Malpuech, A. Di Carlo, A. Kavokin, J. Baumberg, M. Zamfirescu, and P. Lugli, Appl. Phys. Lett. **81**, 412 (2002).

147 G. Messin, J. Karr, A. Baas, G. Khitrova, R. Houdre, R. Stanley, U. Oesterle, and E. Giacobino, Phys. Rev. Lett. **87**, 127403 (2001).

148 D. Porras, C. Ciuti, J. Baumberg, and C. Tejedor, Phys. Rev. B **66**, 085304 (2002).

149 S. Pau, H. Cao, J. Jacobson, G. Bjork, Y. Yamamoto, and A. Imamoglu, Phys. Rev. A **54**, R1789 (1996).

150 S. Pau, J. Jacobson, G. Bjork, and Y. Yamamoto, J. Opt. Soc. Am. B-Opt. Phys. **13**, 1078 (1996).

151 S. Pau, G. Bjork, J. Jacobson, H. Cao, and Y. Yamamoto, Phys. Rev. B **51**, 7090 (1995).

152 F. Quochi, G. Hayes, R. Andre, G. Bongiovanni, A. Mura, J. Staehli, and L. Dang, J. Cryst. Growth **184**, 754 (1998).

153 M. Saba, C. Ciuti, J. Bloch*, et al*, Nature **414**, 731 (2001).

154 L. Sapienza, A. Vasanelli, R. Colombelli, C. Ciuti, Y. Chassagneux, C. Manquest, U. Gennser, and C. Sirtori, Phys. Rev. Lett. **100**, 136806 (2008).

155 P. G. Savvidis, J. J. Baumberg, R. M. Stevenson, M. S. Skolnick, D. M. Whittaker, and J. S. Roberts, Phys. Rev. Lett. **84**, 1547 (2000).

156 R. Stevenson, V. Astratov, M. Skolnick, D. Whittaker, M. Emam-Ismail, A. Tartakovskii, P. Savvidis, J. Baumberg, and J. Roberts, Phys. Rev. Lett. **85**, 3680 (2000).

157 A. I. Tartakovskii, M. Emam-Ismail, R. M. Stevenson, M. S. Skolnick, V. N. Astratov, D. M. Whittaker, J. J. Baumberg, and J. S. Roberts, Phys. Rev. B **62**, R2283 (2000).

158 F. Tassone, C. Piermarocchi, V. Savona, A. Quattropani, and P. Schwendimann, Phys. Rev. B **56**, 7554 (1997).

159 S. I. Tsintzos, N. T. Pelekanos, G. Konstantinidis, Z. Hatzopoulos, and P. G. Savvidis, Nature **453**, 372 (2008).

160 F. Boeuf, R. Andre, R. Romestain, L. Dang, E. Peronne, J. Lampin, D. Hulin, and A. Alexandrou, Phys. Rev. B **62**, R2279 (2000).

161 R. Butte, G. Christmann, E. Feltin, J. Carlin, M. Mosca, M. Ilegems, and N. Grandjean, Phys. Rev. B **73**, 033315 (2006).

162 R. J. Holmes and S. R. Forrest, Org. Electron. **8**, 77 (2007).

163 L. Connolly, D. Lidzey, R. Butte, A. Adawi, D. Whittaker, M. Skolnick, and R. Airey, Appl. Phys. Lett. **83**, 5377 (2003).

164 D. G. Lidzey, D. D. C. Bradley, A. Armitage, S. Walker, and M. S. Skolnick, Science **288**, 1620 (2000).

165 R. J. Holmes and S. R. Forrest, Phys. Rev. Lett. **93**, 186404 (2004).

166 S. Kena-Cohen, M. Davanco, and S. R. Forrest, Phys. Rev. Lett. **101**, 116401 (2008).

167 S. Kena-Cohen and S. R. Forrest, Phys. Rev. B **77**, 073205 (2008).

168 E. Potma and D. Wiersma, J. Chem. Phys. **108**, 4894 (1998).

169 K. Misawa, H. Ono, K. Minoshima, and T. Kobayashi, Appl. Phys. Lett. **63**, 577 (1993).

170 D. Mobius, Adv Mater **7**, 437 (1995).

171 M. Bradley, J. Tischler, and V. Bulovic, Adv Mater **17**, 1881 (2005).

172 P. A. Hobson, W. L. Barnes, D. G. Lidzey, G. A. Gehring, D. M. Whittaker, M. S. Skolnick, and S. Walker, Appl. Phys. Lett. **81**, 3519 (2002).

173 J. Chovan, I. E. Perakis, S. Ceccarelli, and D. G. Lidzey, Phys. Rev. B **78**, 045320 (2008).

174 T. Virgili, D. Coles, A. M. Adawi, C. Clark, P. Michetti, S. K. Rajendran, D. Brida, D. Polli, G. Cerullo, and D. G. Lidzey, Phys. Rev. B **83**, 245309 (2011).

175 N. C. Giebink and S. R. Forrest, Phys. Rev. B **77**, 235215 (2008).

176 J. Kalinowski, L. C. Palilis, W. H. Kim, and Z. H. Kafafi, J. Appl. Phys. **94**, 7764 (2003).

177 K. Tanimura, T. Kawai, and T. Sakata, J. Phys. Chem. **83**, 2639 (1979).

178 D. Dolphin, *The Porphyrins* (Academic Press, New York, 1978), Vol. 3.

179 J. R. Tischler, M. S. Bradley, Q. Zhang, T. Atay, A. Nurmikko, and V. Bulovic, Organic Electronics **8**, 94 (2007).

180 M. Litinskaya, P. Reineker, and V. M. Agranovich, J Lumin **110**, 364 (2004).

181 M. Litinskaya, P. Reineker, and V. M. Agranovich, J Lumin **119**, 277 (2006).

182 I. G. Hill, A. Kahn, J. Cornil, D. A. dos Santos, and J. L. Bredas, Chem. Phys. Lett. **317**, 444 (2000).

183 D. G. Lidzey, J. Wenus, D. M. Whittaker, G. Itskos, P. N. Stavrinou, D. D. C. Bradley, and R. Murray, J Lumin **110**, 347 (2004).

184 R. J. Holmes, S. Kena-Cohen, V. M. Menon, and S. R. Forrest, Phys. Rev. B **74**, 235211 (2006).

185 A. Camposeo, L. Persano, P. Del Carro, T. Virgili, R. Cingolani, and D. Pisignano, Org. Electron. **8**, 114 (2007).

186 G. Panzarini, L. Andreani, A. Armitage, D. Baxter, M. Skolnick, V. Astratov, J. Roberts, A. Kavokin, M. Vladimirova, and M. Kaliteevski, Phys. Rev. B **59**, 5082 (1999).

187 T. Virgili, D. G. Lidzey, D. D. C. Bradley, and S. Walker, Synth. Met. **116**, 497 (2001).

188 M. Oda, K. Hirata, T. Inoue, Y. Obara, T. Fujimura, and T. Tani, **6**, 291 (2009).

189 F. L. Pedrotti and L. S. Pedrotti, *Introduction to optics* (Prentice Hall International, Englewood Cliffs, N.J., 1996).

190 W. M. Haynes, *Handbook of Chemistry and Physics* (CRC, 2010).

191 G. H. Lodden and R. J. Holmes, Phys. Rev. B **83**, 075301 (2011).

192 F. Ma and X. Liu, Appl. Opt. **46**, 6247 (2007).

193 H. Becker, S. E. Burns, N. Tessler, and R. H. Friend, J. Appl. Phys. **81**, 2825 (1997).

194 G. H. Lodden and R. J. Holmes, Phys. Rev. B **82**, 125317 (2010).

195 N. C. Lindquist, W. A. Luhman, S. Oh, and R. J. Holmes, Appl. Phys. Lett. **93**, 123308 (2008).

196 V. J. Sorger, R. F. Oulton, J. Yao, G. Bartal, and X. Zhang, Nano Lett. **9**, 3489 (2009).

197 R. Ameling and H. Giessen, Nano Lett. **10**, 4394 (2010).

198 T. Yoshie, A. Scherer, J. Hendrickson, G. Khitrova, H. Gibbs, G. Rupper, C. Ell, O. Shchekin, and D. Deppe, Nature **432**, 200 (2004).

199 J. Reithmaier, G. Sek, A. Loffler, C. Hofmann, S. Kuhn, S. Reitzenstein, L. Keldysh, V. Kulakovskii, T. Reinecke, and A. Forchel, Nature **432**, 197 (2004).

200 D. Englund, A. Faraon, I. Fushman, N. Stoltz, P. Petroff, and J. Vuckovic, Nature **450**, 857 (2007).

201 D. Englund, D. Fattal, E. Waks, G. Solomon, B. Zhang, T. Nakaoka, Y. Arakawa, Y. Yamamoto, and J. Vuckovic, Phys. Rev. Lett. **95**, 013904 (2005).

202 M. Hubner, J. P. Prineas, C. Ell, P. Brick, E. S. Lee, G. Khitrova, H. M. Gibbs, and S. W. Koch, Phys. Rev. Lett. **83**, 2841 (1999).

203 D. Goldberg, L. I. Deych, A. A. Lisyansky, Z. Shi, V. M. Menon, V. Tokranov, M. Yakimov, and S. Oktyabrsky, Nat. Photonics **3**, 662 (2009).

204 A. Askitopoulos, L. Mouchliadis, I. Iorsh, G. Christmann, J. J. Baumberg, M. A. Kaliteevski, Z. Hatzopoulos, and P. G. Savvidis, Phys. Rev. Lett. **106**, 076401 (2011).

205 R. H. Dicke, Phys. Rev. **93**, 99 (1954).

206 M. V. Erementchouk, L. I. Deych, and A. A. Lisyansky, Phys. Rev. B **71**, 235335 (2005).

207 K. Sumioka, H. Nagahama, and T. Tsutsui, Appl. Phys. Lett. **78**, 1328 (2001).

208 K. Hennessy, A. Badolato, M. Winger, D. Gerace, M. Atatuere, S. Gulde, S. Faelt, E. L. Hu, and A. Imamoglu, Nature **445**, 896 (2007).

209 D. Englund, A. Majumdar, A. Faraon, M. Toishi, N. Stoltz, P. Petroff, and J. Vuckovic, Phys. Rev. Lett. **104**, 073904 (2010).

210 V. M. Agranovich, M. Litinskaia, and D. G. Lidzey, Phys. Status Solidi B-Basic Res. **234**, 130 (2002).

211 H. Zoubi and G. La Rocca, Phys. Rev. B **72**, 125306 (2005).

212 H. Zoubi and G. La Rocca, Phys. Rev. B **71**, 235316 (2005).

213 H. Zoubi, Phys. Rev. B **74**, 045317 (2006).

214 H. Zoubi and G. C. La Rocca, Phys. Rev. B **76**, 035325 (2007).

215 H. Zoubi and G. C. La Rocca, Phys. Rev. B **77**, 159905 (2008).

216 J. Song, Y. He, A. Nurmikko, J. Tischler, and V. Bulovic, Phys. Rev. B **69**, 235330 (2004).

217 A. I. Tartakovskii, V. D. Kulakovskii, A. V. Larionov, J. P. Reithmaier, and A. Forchel, Phys. Status Solidi A-Appl. Res. **164**, 81 (1997).

218 R. Houdre, J. L. Gibernon, P. Pellandini, R. P. Stanley, U. Oesterle, C. Weisbuch, J. Ogorman, B. Roycroft, and M. Ilegems, Phys. Rev. B **52**, 7810 (1995).

219 H. Cao, S. Pau, J. Jacobson, G. Bjork, Y. Yamamoto, and A. Imamoglu, Phys. Rev. A **55**, 4632 (1997).

220 G. Christmann, R. Butte, E. Feltin, A. Mouti, P. A. Stadelmann, A. Castiglia, J. Carlin, and N. Grandjean, Phys. Rev. B **77**, 085310 (2008).

221 S. Faure, T. Guillet, P. Lefebvre, T. Bretagnon, and B. Gil, Phys. Rev. B **78**, 235323 (2008).

222 N. Antoine-Vincent, F. Natali, D. Byrne, A. Vasson, P. Disseix, J. Leymarie, M. Leroux, F. Semond, and J. Massies, Phys. Rev. B **68**, 153313 (2003).

223 K. Torii, T. Deguchi, T. Sota, K. Suzuki, S. Chichibu, and S. Nakamura, Phys. Rev. B **60**, 4723 (1999).

224 C. Klingshirn, R. Hauschild, H. Priller, M. Decker, J. Zeller, and H. Kalt, Superlattices Microstruct. **38**, 209 (2005).

225 M. Zamfirescu, A. Kavokin, B. Gil, G. Malpuech, and M. Kaliteevski, Phys. Rev. B **65**, 161205 (2002).

226 S. Chichibu, A. Uedono, A. Tsukazaki*, et al*, Semicond. Sci. Technol. **20**, S67 (2005).

227 R. Schmidt-Grund, B. Rheinlaender, C. Czekalla, G. Benndorf, H. Hochmut, A. Rahm, A. Lorenz, and A. Grundmann, Superlattices Microstruct. **41**, 360 (2007).

228 R. Shimada, J. Xie, V. Avrutin, U. Ozgur, and H. Morkoc, Appl. Phys. Lett. **92**, 011127 (2008).

229 R. Schmidt-Grund, B. Rheinlaender, C. Czekalla, G. Benndorf, H. Hochmuth, M. Lorenz, and M. Grundmann, Appl. Phys. B-Lasers Opt. **93**, 331 (2008).

230 M. Nakayama, S. Komura, T. Kawase, and D. Kim, J. Phys. Soc. Jpn. **77**, 093705 (2008).

231 R. Johne, D. D. Solnyshkov, and G. Malpuech, Appl. Phys. Lett. **93**, 211105 (2008).

232 J. Chen, T. Lu, Y. Wu, S. Lin, W. Liu, W. Hsieh, C. Kuo, and C. Lee, Appl. Phys. Lett. **94**, 061103 (2009).

233 C. Sturm, H. Hiimer, R. Schmidt-Grund, and M. Grundmann, New J. Phys. **13**, 033014 (2011).

234 S. -. Lin, J. -. Chen, and T. -. Lu, Appl. Phys. B-Lasers Opt. **103**, 137 (2011).

235 J. Chen, T. Lu, Y. Wu, S. Lin, W. Hsieh, S. Wang, and H. Deng, Opt. Express **19**, 4101 (2011).

236 T. Chao, Y. Lin, C. Yang, T. Hung, H. Chou, C. Wu, and K. Wong, Adv Mater **17**, 992 (2005).

237 B. Sang and M. Konagai, Jpn. J. Appl. Phys. Part 2 - Lett. **35**, L602 (1996).

238 A. Yamada, B. Sang, and M. Konagai, Appl. Surf. Sci. **112**, 216 (1997).

239 T. A. Krajewski, G. Luka, L. Wachnicki, R. Jakiela, B. Witkowski, E. Guziewicz, M. Godlewski, N. Huby, and G. Tallarida, Opt. Appl. **39**, 865 (2009).

240 T. A. Krajewski, G. Luka, L. Wachnicki*, et al*, Semicond. Sci. Technol. **26**, 085013 (2011).

241 Y. Kuwabara, H. Ogawa, H. Inada, N. Noma, and Y. Shirota, Adv Mater **6**, 677 (1994).

242 R. Chesterfield, C. Newman, T. Pappenfus, P. Ewbank, M. Haukaas, K. Mann, L. Miller, and C. Frisbie, Adv Mater **15**, 1278 (2003).

Appendix

A. List of Publications and Presentations

Publications:

1) ”Electrical excitation of microcavity polaritons by radiative pumping from a weakly coupled organic semiconductor,” **G.H. Lodden** and R.J. Holmes, *Physical Review B*, 82, 125317 (**2010**).

2) “Thermally activated population of microcavity polariton states under optical and electrical excitation,” **G.H. Lodden** and R.J. Holmes, *Physical Review B*, 83, 075301 (**2011**).

3) “Polarization splitting in polariton electroluminescence from an organic semiconductor microcavity with metallic reflectors,” **G.H. Lodden** and R.J. Holmes, *Applied Physics Letters*, 98, 233301 (**2011**).

4) “Long-range, photon-mediated exciton hybridization in an all-organic, one-dimensional photonic crystal,” **G.H. Lodden** and R.J. Holmes, *Physical Review Letters*, 109, 096401 (**2012**).

Presentations and Posters:

1) “Optical Microcavities for Organic Optoelectronic Devices,” IPRIME Annual Meeting, Minneapolis, MN (May 2008). (Presentation)

2) “Optical Microcavities for Organic Optoelectronic Devices,” IPRIME Annual Meeting, Minneapolis, MN (May 2008). (Poster)

3) “The Origin of Electro- and Photoluminescence in Strongly Coupled Organic Microcavities,” IPRIME Annual Meeting, Minneapolis, MN (May 2009). (Poster)

4) “The Origin of Electro- and Photoluminescence in Strongly Coupled Organic Microcavities,” 3M Sponsored Poster Session, Minneapolis, MN (October 2009). (Poster)

5) “The Origin of Electro- and Photoluminescence in Strongly Coupled Organic Microcavities,” Minnesota Nanotechnology Conference, Minneapolis, MN (November 2009). (Poster)

6) “The Origin of Electro- and Photoluminescence in Strongly Coupled Organic Microcavities,” MRS Fall Meeting, Boston MA (December 2009). (Presentation)

7) "The population of exciton-polariton states in microcavity organic light-emitting devices," IPRIME Annual Meeting, Minneapolis, MN (June 2010). (Poster)

8) "The population of exciton-polariton states in microcavity organic light-emitting devices," Minnesota Nanotechnology Conference, Minneapolis, MN (October 2010). (Poster)

9) "Light-matter interactions in optical nanostructures based on organic semiconductors," IPRIME Annual Meeting, Minneapolis, MN (June 2011). (Poster)

10) "Microcavity polariton electroluminescence via radiative pumping from a weakly coupled organic semiconductor," SPIE Photonics and Optics, San Diego, CA (August 2011). (Presentation)

B. Transfer Matrix Simulation Code

The microcavities studied in Chapters 5, 6, and 7 were modeled using the transfer matrix formulism presented in Chapter 5. The code provided in this Appendix is specifically tailored to the microcavity of Chapter 5 but can be extended to model other structures such as those shown in Chapters 6 and 7. The code was developed and compiled in Matlab.

```
clear
clc

%Define angle of incidence
angle=15;
phi=angle*(pi/180);

%Define thicknesses
d=[0 50 65 10 70 10 50 0];

%Define # of layers
[z,x]=size(d);
layers=x;

%Define emitting interface
emitting=4;

%Get material optical constants
load('Ag.txt');
load('Aloptical.txt');
load('Alqoptical.txt');
load('BCPoptical.txt');
load('NPDoptical.txt');
load('TPPoptical.txt');

%Define wavelength
lambda=400:1:800;
wavelength=transpose(lambda);

for a=1:1:size(wavelength)
   one(a)=1;
   zero(a)=0;
end

Airreal=transpose(one);
Airimag=transpose(zero);
```

```
%Get index data
Agreal=Ag(:,2);
Agimag=Ag(:,3);
Alreal=Aloptical(:,2);
Alimag=Aloptical(:,3);
Alqreal=Alqoptical(:,1);
Alqimag=Alqoptical(:,2);
BCPreal=BCPoptical(:,2);
BCPimag=BCPoptical(:,3);
NPDreal=NPDoptical(:,2);
NPDimag=NPDoptical(:,3);
TPPreal=TPPoptical(:,2);
TPPimag=TPPoptical(:,3);

%Define complex index matrix
ni=[Airreal complex(Agreal,Agimag) complex(TPPreal,TPPimag)
complex(NPDreal,NPDimag) complex(Alqreal,Alqimag) complex(BCPreal,BCPimag)
complex(Alreal,Alimag) Airreal];
%Initialize incident E-field
Eo=1;

for a=1:1:size(wavelength)

   Energy(a)=((6.626E-34*3.0E8)/(lambda(a)*1.0E-9*1.6E-19));

   %Define source terms, dipole horizontal, polarization dependent
   kz1(a)=(2*pi*real(ni(a,emitting))*cos(phi))./(1.0E-9*lambda(a));
   k1(a)=real(ni(a,emitting))*((2*pi)./(1.0E-9*lambda(a)));
   kp(a)=(2*pi*real(ni(a,emitting))*sin(phi))./(1.0E-9*lambda(a));
   Aups(a)=-1*0.5*(3/(16*pi))^(1/2));
   Adowns(a)=0.5*(3/(16*pi))^(1/2));
   Aupp(a)=-(0.5*((3/(16*pi))^(1/2)*(kz1(a)./k1(a))+0.5*(3/(8*pi))^(1/2)*(kp(a)./k1(a)));
   Adownp(a)=(0.5*(3/(16*pi))^(1/2)*(kz1(a)./k1(a))+
                  0.5*(3/(8*pi))^(1/2)*(kp(a)./k1(a)));

   %Initialize Ss
   Ss(:,:,a)=[1 0;0 1];

   %Initialize Sp
   Sp(:,:,a)=[1 0;0 1];

   %Calculate q
   for j=1:1:layers
```

```
    qj(a,j)=(ni(a,j).^2-ni(a,1).^2*(sin(phi))^2)^(1/2);
end

%Calculate Fresnel coefficients for s-polarized
for j=1:1:layers-1
    rjks(a,j)=(qj(a,j)-qj(a,(j+1)))/(qj(a,j)+qj(a,(j+1)));
    tjks(a,j)=(2*qj(a,j))/(qj(a,j)+qj(a,j+1));
end

%Calculate Fresnel coefficients for p-polarized
for j=1:1:layers-1
    rjkp(a,j)=(((ni(a,j)).^2).*qj(a,j+1))-((ni(a,j+1)).^2).*qj(a,(j)))/(((ni(a,j+1)).^2).*
                qj(a,j)+((ni(a,j)).^2).*qj(a,(j+1)));
    tjkp(a,j)=(2*((ni(a,j)).*(ni(a,j+1)).*qj(a,j)))/(((ni(a,j+1)).^2).*qj(a,j)+((ni(a,j)).^2).*
                qj(a,(j+1)));
end

%Calculate interface matrix for s-polarized
for j=1:1:layers-1
    Is(:,:,j,a)=(1/tjks(a,j)).*[1 rjks(a,j);rjks(a,j) 1];
end

%Calculate interface matrix for p-polarized
for j=1:1:layers-1
    Ip(:,:,j,a)=(1/tjkp(a,j)).*[1 rjkp(a,j);rjkp(a,j) 1];
end

%Calculate layer matrix for s or p-polarized
for t=1:1:layers
    Lsp(:,:,t,a)=[exp((-i.*2.*pi./wavelength(a)).*qj(a,t).*d(t)) 0;0
    exp((i.*2.*pi./wavelength(a)).*qj(a,t).*d(t))];
end

%Total system transfer matrix for s-polarized
for n=1:1:layers-2
    Ss(:,:,a)=Ss(:,:,a)*Is(:,:,n,a)*Lsp(:,:,n+1,a);
end
Ss(:,:,a)=Ss(:,:,a)*Is(:,:,layers-1,a);

%Total system transfer matrix for p-polarized
for n=1:1:layers-2
    Sp(:,:,a)=Sp(:,:,a)*Ip(:,:,n,a)*Lsp(:,:,n+1,a);
end
Sp(:,:,a)=Sp(:,:,a)*Ip(:,:,layers-1,a);
```

```
%Total reflection and transmission coefficients for s-polarized
rs(a)=Ss(2,1,a)./Ss(1,1,a);
ts(a)=1./Ss(1,1,a);

phases(a)=atan(imag(rs(a))./real(rs(a)));
RIntensitys(a)=rs(a).*conj(rs(a));
TIntensitys(a)=1-RIntensitys(a);

%Total reflection and transmission coefficients for p-polarized
rp(a)=Sp(2,1,a)./Sp(1,1,a);
tp(a)=1./Sp(1,1,a);

phasep(a)=atan(imag(rp(a))./real(rp(a)));
RIntensityp(a)=rp(a).*conj(rp(a));
TIntensityp(a)=1-RIntensityp(a);

%Calculating subset transfer matrices for left side of emitting layer
 for q=1:1:layers-1

    %Initialize Ssprime
    Ssprime(:,:,a,q)=[1 0;0 1];

    %Initialize Ss2prime
    Ss2prime(:,:,a,q)=[1 0;0 1];

    if q==1
       Ssprime(:,:,a,q)=Is(:,:,q,a);
    else
       for n=1:1:q-1
          Ssprime(:,:,a,q)=Ssprime(:,:,a,q)*Is(:,:,n,a)*Lsp(:,:,n,a);
       end
       Ssprime(:,:,a,q)=Ssprime(:,:,a,q)*Is(:,:,n+1,a);
    end

    if q==layers-1
       Ss2prime(:,:,a,q)=Is(:,:,q,a);
    else
       for m=q:1:layers-1
          t=q+1;
          Ss2prime(:,:,a,q)=Ss2prime(:,:,a,q)*Is(:,:,t,a)*Lsp(:,:,t,a);
       end
       Ss2prime(:,:,a,q)=Ss2prime(:,:,a,q)*Is(:,:,m,a);
    end
```

```
end

%Calculate emitted field from cavity for s-polarized
Ssprimeemits(:,:,a)=[1 0;0 1];
Ss2primeemits(:,:,a)=[1 0;0 1];

for b=1:1:emitting-1
   Ssprimeemits(:,:,a)=Ssprimeemits(:,:,a)*Is(:,:,b,a)*Lsp(:,:,b+1,a);
end

for b=emitting:1:layers-2
   Ss2primeemits(:,:,a)=Ss2primeemits(:,:,a)*Lsp(:,:,b+1,a)*Is(:,:,b+1,a);
end

Eoemits(a)=((Ssprimeemits(1,1,a).*Ssprimeemits(2,2,a)-
            (1,2,a).*Ssprimeemits(2,1,a)).*
            (Ss2primeemits(2,1,a).*Aups(a)-s2primeemits(1,1,a).*Adowns(a))./
            (Ssprimeemits(1,1,a).*Ss2primeemits(1,1,a)+Ss2primeemits(,1,a).*
            Ssprimeemits(1,2,a));
E2emits(a)=(Ssprimeemits(1,1,a).*Aups(a)+Ssprimeemits(1,2,a).*Adowns(a))./
           (Ssprimeemits(1,1,a).*Ss2primeemits(1,1,a)+Ss2primeemits(2,1,a).*
            Ssprimeemits(1,2,a));

EoemitIntensitys(a)=Eoemits(a).*conj(Eoemits(a));
E2emitIntensitys(a)=E2emits(a).*conj(E2emits(a));

%Calculate emitted field from cavity for p-polarized
Ssprimeemitp(:,:,a)=[1 0;0 1];
Ss2primeemitp(:,:,a)=[1 0;0 1];

for b=1:1:emitting-1
   Ssprimeemitp(:,:,a)=Ssprimeemitp(:,:,a)*Ip(:,:,b,a)*Lsp(:,:,b+1,a);
end

for b=emitting:1:layers-2
   Ss2primeemitp(:,:,a)=Ss2primeemitp(:,:,a)*Lsp(:,:,b+1,a)*Ip(:,:,b+1,a);
end

Eoemitp(a)=((Ssprimeemitp(1,1,a).*Ssprimeemitp(2,2,a)-Ssprimeemitp(1,2,a).*
            Ssprimeemitp(2,1,a)).*(Ss2primeemitp(2,1,a).*Aupp(a)-
            Ss2primeemitp(1,1,a).*
            Adownp(a))./(Ssprimeemitp(1,1,a).*Ss2primeemitp(1,1,a)+
            Ss2primeemitp(2,1,a).*Ssprimeemitp(1,2,a));
```

```
    E2emitp(a)=(Ssprimeemitp(1,1,a).*Aupp(a)+Ssprimeemitp(1,2,a).*Adownp(a))./
                    (Ssprimeemitp(1,1,a).*Ss2primeemitp(1,1,a)+
                     Ss2primeemitp(2,1,a).*Ssprimeemitp(1,2,a));

    EoemitIntensityp(a)=Eoemitp(a).*conj(Eoemitp(a));
    E2emitIntensityp(a)=E2emitp(a).*conj(E2emitp(a));

end

figure
plot(Energy,RIntensitys,'k'), xlabel('Energy (eV)'), ylabel('Reflectivity');
hold on
plot(Energy,RIntensityp,'r'), legend('S-Polarized','P-Polarized');

figure
plot(Energy,EoemitIntensitys,'r'), xlabel('Energy (eV)'), ylabel('Emission');
hold on
plot(Energy,E2emitIntensitys,'b'), legend('S-Polarized','P-Polarized')hold on
hold on
plot(Energy,EoemitIntensityp,'g');
hold on
plot(Energy,EoemitIntensityp,'k');
```